HIGH-SPEED FUEL AND FLOW IMAGING TO INVESTIGATE MISFIRES IN A SPRAY-GUIDED DIRECT-INJECTION ENGINE

by

Brian R. Peterson

A dissertation submitted in partial fulfillment
of the requirements for the degree of
Doctor of Philosophy
(Mechanical Engineering)
in The University of Michigan
2010

Doctoral Committee:

Professor Volker Sick Chair
Professor Dionissios N. Assanis
Professor James F. Driscoll
Associate Professor Claus Borgnakke
Xiaofeng Yang, General Motors Corporation

DEDICATION

To My Family and Friends

ACKNOWLEDGMENTS

I would first like to thank my advisor Volker Sick for the great opportunity to work with optical diagnostics not only in my graduate career, but in my post graduate career. Also I would like to thank him for the wonderful opportunities he has provided for me: working at Sandia National Laboratories for my Master's research, experience teaching ME 395, interning at General Motors Corporation, opportunity to research abroad in Aachen, Germany, and introducing me to Andreas Dreizler at Technische Universität Darmstadt which has lead to a post-doc position in the Center of Smart Interfaces group. I would also like to thank Dr. David L. Reuss for helping me understand the bounds of my experimental data and walking me through tough times of how to analyze engine data such as presented in this work.

I would also like to thank my committee for participating in my research. I would also like to thank Mike Drake, Todd Fansler, Tang-Wei Quo, Arun Solomon, and Xiaofeng Yang at General Motors Corporation for wonderful insight to interpreting my data and asking grueling questions that help me prepare for the real world.

I would also like to thank my family and friends for their support in my graduate studies. I would like to thank Emily Junck for sticking by my side on the late nights of writing and giving me motivation for waking up the next day and doing it all over again. I big thank you to my lab mates, particularly Ali Alharbi, Louise Lu, and Mike Mosburger for helping me with experimental setups and obtaining the combined PLIF PIV data. I big

thank you to God who has given me a reason to live and has obviously seen me day in day out for all my life helping me live to the fullest in all my ways.

Table of Contents

LIST OF FIGURES

LIST OF TABLES

LIST OF APPENDICES

LIST OF ABBREVIATIONS

AG: Air-Guided

ATDC: After Top-Dead Center

BTDC: Before Top-Dead Center

CAD: Crank-Angle Degree

CI: Compression Ignition

COV: Coefficient of Variance

EGR: Exhaust Gas Recirculation

EOI: End-of-Injection

EPA: Environmental Protection Agency

ESC: Engine Setpoint Controller

EVC: Exhaust Valve Closing

EVO: Exhaust Valve Opening

HR: High-Reflectivity

HT: High-Transmissivity

IC: Internal Combustion

IMEP: Indicated Mean Effective Pressure

IVC: Intake Valve Closing

IVO: Intake Valve Opening

LES: Large Eddy Simulation

LIF: Laser Induced Fluorescence

MAP: Manifold Absolute Pressure (Intake)

MFB: Mass Fraction Burned

PFI: Port-Fueled Injection

PIV: Particle Image Velocimetry

PLIF: Planar Laser Induced Fluorescence

RMS: Root Mean Squared

SI: Spark Ignition

SIDI: Spark-Ignition Direct-Injection

SG: Spray-Guided

SG-SIDI: Spray-Guided Spark-Ignition Direct-Injection

TDC: Top-Dead-Center

UV: Ultra Violet

WG: Wall-Guided

WOT: Wide Open Throttle

ABSTRACT

Simultaneous high-speed fuel fluorescence and particle image velocimetry measurements are combined with spark discharge measurements for the first time to identify the cause of misfire and partial burn cycles in a spray-guided spark-ignited direct-injection engine. Spark ignition is studied for stratified charge operation under a range of external dilution levels (0% - 26% nitrogen). Available spark energy is characterized for a wide range of well-controlled homogeneous gas-phase fuel-air mixtures (Φ = 0.0 - 2.9) and flow conditions (|V| = 1 - 10 m/s) that are characteristic for the spark energy under stratified charge conditions. Under stratified charge conditions, the engine operates with an optimized end-of-injection and spark timing that provides stable engine operation with the occurrence of rare misfire and partial burn cycles. Fuel concentration and flow field measurements are analyzed closest to the spark plug and in the entire field of view (38 mm x 30 mm) within the combustion chamber to diagnose the role of fuel distribution, flow field, and spark energy on misfire, partial burn, and well-burning cycles. Results show that abnormal spark behavior is not the cause of the misfire and partial burn cycles and a model is used to show that all cycles have sufficient electrical spark energy to ignite the flammable mixture nearby the spark plug. The high-speed fuel and flow images reveal that a flame kernel is developed for all cycles. For all errant cycles, flame propagation is too slow due to either lean and/or diluted mixtures and

the flame kernel is not able to catch up to the fuel cloud that travels away from the spark plug. As a result, the flame kernel is surrounded by lean fuel-air mixtures that are insufficient to further support adequate flame kernel growth, leading to a misfire or partial burn. This work demonstrates the increased need for precise fuel injection and atomization control as well as consistent in-cylinder flow patterns that provide favorable mixtures for flame kernel development throughout the entire spark event.

CHAPTER 1

INTRODUCTION

1.1 Spark Ignition Engines

Automobiles are one of the single-most common modes of personal transportation in the world today. The core of the automobile, as we know it today, is the internal combustion (IC) engine, which is a major contributor to the consumption of fossil fuels and production of air pollution. Automotive engineers are continually striving to develop IC engines that improve automotive fuel economy while meeting the progressing strict emission requirements set by agencies like the Environmental Protection Agency (EPA).

The majority of the automobiles in production today, especially in the United States, operate with the gasoline spark-ignited (SI) engine. With the use of a three-way catalyst, the SI engine outputs the least amount of emissions compared to other IC engines, such as the compression ignition (CI) diesel engine, but is far less efficient and has a higher fuel consumption.

The port-fueled injection (PFI) SI engine has been the conventional gasoline engine for the past 30 years [1]. The PFI strategy uses a reliable, yet inefficient method to control the engine load. Load is equivalent to the output power of the engine and is controlled by the amount of fuel and air introduced into the engine cylinder. Under the PFI strategy, the air flow is controlled by means of a throttle plate. Fuel is injected downstream the throttle plate and fully mixes with the air before entering the cylinder.

The amount of fuel injected is proportion to the amount of throttled air to achieve a near stoichiometric fuel-air mixture as required by the 3-way catalyst. At low loads, the throttle plate is primarily closed, limiting the amount of mixture inducted into the cylinder during the intake stroke. The closed throttle position creates substantial pumping losses during the engine cycle, thus decreasing the efficiency of the engine and increasing fuel consumption. It is desired to operate the SI engine unthrottled and restrict the fuel for load control during the low to mid load regime to increase the efficiency of the engine. For this, the engine would operate overall lean and cannot achieve flame propagation for a homogeneous mixture at the lightest loads and idle conditions when the amount of fuel is the least. Stratifying the fuel charge is a method to localize a flammable mixture within the cylinder to allow flame propagation in an overall lean fuel-air mixture, and thereby allow unthrottled engine operation.

Direct injection of the fuel into the cylinder can provide suitable charge stratification allowing flame propagation in overall lean mixtures. Here, fuel and air are introduced separately into the combustion chamber; unthrottled air is inducted during the intake stroke while fuel is injected directly into the cylinder. Load control is achieved by controlling the amount of fuel injected for each cycle, while the amount of air under a given engine speed remains the same. Under higher loads, more fuel is needed and is injected earlier, often during the intake stroke, creating a homogeneous mixture similar to that seen in conventional SI engine operation. Under low to mid loads, less fuel is needed and is injected during the compression stroke. Late injection of the fuel creates a highly stratified mixture, concentrating ignitable mixtures near the spark plug while leaving peripheral regions of the combustion chamber fuel-lean. Fuel savings are the greatest

under low- to moderate-loads, compared to the PFI strategy, where the limited need of the throttle plate in combination with lower amount of fuel injected increases fuel economy.

Automotive engineers have been trying to implement the direct-injection concept in spark-ignited engines since the early 1920's [1]. Until recently, the technology has not been available for this realization. Advancement in electronic control and nano-manufacturing has lead to the development of high-pressure injectors with smaller nozzle diameters, precise needle valve seating and lift, and accurate fuel metering. Higher injection pressures and smaller nozzle diameters allow better atomization of the fuel and enhance the mixing of the fuel and air. In all, these advancements have led to a more reliable and repeatable injection event.

The spark-ignition direct-injection (SIDI) engine has been upcoming within the automotive industry since the mid-1990's. There are three classifications of SIDI engines used in automobiles: air-guided (AG), wall-guided (WG), and spray-guided (SG) [2]. These classifications are defined by the strategy used to deliver a stratified charge to the spark plug during part-load. Air-guided systems rely on the bulk motion of the flow to deliver an ignitable mixture to the spark plug. The intake system and combustion chamber geometry are specially designed to create a repeatable motion of the bulk flow during the compression stroke. Wall-guided systems use a physical boundary to deflect fuel to the spark plug. Typically, fuel is sprayed from a side-mounted injector and is reflected upward off a contoured piston top towards the spark plug [3]. Spray-guided systems typically operate with a centrally mounted fuel injector that sprays along the cylinder axis. Fuel spray is targeted at the spark plug, with the edge of the spray plume

typically seen at the spark electrodes. Spark timing is highly coupled with the spray event under the SG strategy.

The spray-guided approach offers significant advantages over the air-guided and wall-guided approaches. For the air-guided approach, bulk air motion can dramatically change with manifold pressure and engine speed making it difficult to reliably deliver an ignitable mixture to the spark plug over the entire engine operating range. Spray-guided systems offer a wider stratified operating range than wall-guided systems due to the close interaction between the spray and spark event. The spray-guided approach provides reduced soot and hydrocarbon emissions than the wall-guided approach due to reduced piston wetting and a more compact fuel cloud [3]. These advantages arguably suggest that the spray-guided approach is the next generation for of SIDI engines [3].

The SG-SIDI engine is capable of operating under homogeneous or stratified charges which are created by the timing of the fuel injection during the engine cycle. For homogeneous operation, fuel is injected early, typically within the intake stroke to allow sufficient mixing of fuel and air before spark. Homogeneous operation is utilized at high engine loads where more fuel is needed and is similar in operation to the PFI strategy at wide open throttle (WOT). For stratified operation, fuel is injected late within the compression stroke, typically just before spark. Stratified operation is utilized for low-to-moderate loads when less fuel is needed and a stratified charge is required to maintain a flammable mixture near the spark plug. Here, a flammable mixture is concentrated near the spark plug, while the peripheral regions of the combustion are fuel-lean.

At low-to-moderate loads, fuel savings are greatest with the SG strategy compared to the PFI strategy; however, reliable engine operation may be more difficult to

obtain. Under low-loads, the SG-SIDI engine is more prone to misfires during which combustion does not occur and the work output is lost for that particular engine cycle. The strong coupling between the spray event and spark event is crucial to achieve successful combustion. Optimum timing of the spark is limited to a narrow crank-angle regime and typically occurs during or directly after the spray event. The spark plasma is exposed to a wide range of fuel-air mixtures, high velocity magnitudes, and velocity gradients – all of which have a significant role in defining the ignition event. Large cycle-to-cycle variation of mixtures and flow fields exists, particularly near the spark plug. If the onset of spark is not at its optimum timing or if cycle-to-cycle variations are too extreme, conditions near the spark plug can hinder spark ignition and lead to a misfire.

Before the SG strategy can replace the PFI strategy the occurrence of misfires must be limited if not eliminated. Therefore, it is necessary to identify the conditions that lead to a misfire so that automotive engineers can suitably design the engine and operating parameters that avoid these conditions.

1.2 Spark Ignition

Spark ignition is used in many industrial applications, but is most commonly known for its application in the gasoline spark ignition engine. Here, the spark creates a point source ignition site inside of the combustion chamber. Successful implementation of spark ignition in an engine requires a strong fundamental understanding of spark behavior over a wide range of operating conditions. To date, most spark ignition studies have been focused on applications for PFI engines; operating conditions consist of lean-to-homogeneous stoichiometric mixtures and low-to-moderate turbulence levels defined

by the piston movement and intake air motion. With the introduction of the SG-SIDI engine, the spark event must also be well characterized for conditions seen under late-injection stratified operation; namely a wide range of fuel-air mixtures, high velocity magnitudes, and velocity gradients – all of which are created from the injection event.

1.2.1 Spark Discharge Process

The spark discharge consists of three distinct and consecutive phases: breakdown, arc, and glow. Although automotive ignition systems can be operated to complete the plasma discharge at the end of any of these three phases [4], the most common ignition system utilizes all three phases with most of the spark energy being released during the glow discharge phase.

The breakdown phase occurs at the onset of spark when the increasing electric field creates a plasma channel (~ 40 μm diameter) that extends along the shortest path between the electrodes [5]. The breakdown plasma contains an extremely high degree of ionization and electronic excitation. A high radical density is present within the plasma with heavy particles existing as highly excited atoms and ions carrying more than 20eV of internal or potential energy [4]. Temperatures within the plasma channel reach up to 60,000K, with a very steep temperature gradient at its surface. The breakdown event occurs on a very short time-scale (~ 10 ns) and is characterized by a high voltage drop (~ 5 – 20 kV) and a high-peak current of roughly 200 A. Electrical power is greatest during the breakdown event, but the electrical energy is minimal due to its short time-scale. Heat transfer losses to the electrodes and surrounding gas are also minimal due to the short time-scale.

The arc phase occurs directly after the breakdown phase and exists for a longer duration on the order of μs to ms. The arc phase is characterized by a lower voltage at the electrodes (~ 100 V) and currents in excess of 100 mA [4]. The current is often determined by the external circuitry of the ignition system. During the arc phase, the plasma channel expands largely due to heat conduction and mass diffusion. The electric field between the electrodes decreases and the larger plasma channel carries less current flux. Within the plasma channel, there is an overall lower degree of ionization, even though the degree of dissociation may still be high in the center of the plasma. The temperature of the plasma cools significantly (~ 6000 K) due to the rapid expansion and heat loss to the electrodes.

The third phase is the glow discharge phase and occurs throughout the remainder of the spark event (order of ms). During this phase the remaining energy stored in the coil is dumped into the discharge circuit and throughout the spark plasma. At the transition from arc to glow, the voltage at the electrodes typically increases (200-500 V), while the current through the plasma decreases (< 100 mA) and continues to decrease through the remainder of the spark event. Energy losses are greatest during the glow discharge and the temperature of the plasma is reduced to a value of 1000 K - 3000 K [6]. A high-pressure glow discharge phase is similar to the arc phase, but with a cold cathode and lower ionization levels. The majority of the spark energy is released during the arc and glow phases due to their relatively long durations.

1.2.2 Spark Ignition in IC Engine Environments

The fundamental physics of spark ignition and its use in internal combustion engines has been reviewed by Maly [4]. Most spark ignition studies have been conducted

in enclosed chambers [7, 8, 9, and 10], constant volume combustion chambers [6, 11, 12, and 13], and spark ignition engines [5, 14, and 15]. Studies conducted in enclosed chambers were performed under moderate pressures (< 4 bar) and moderate temperatures (< 400 K) and do not represent the environment seen in an operating engine. Most experiments performed in spark-ignited engines focused on the ability of the spark plasma to ignite a given mixture and did not concentrate on the spark behavior. These studies concentrated on obtaining minimum ignition energy [12 and 13], extending the lean misfire limit [16, 17, and 18], and reducing cycle-to-cycle variation in spark-ignited engines [19 and 20].

1.2.2.1 Spark Behavior in Flow Fields

When the spark plasma is subject to a flow field, the discharge path will change its length and shape in the direction of the local flow field. As the plasma channel stretches outward from the spark gap, the voltage between the electrodes increases. The voltage rise due to flow field occurs only within the arc and glow phases because these events exist on a time-scale long enough to be affected by a flow. Maly [11] has developed a theoretical linear relationship between the voltage rise of the arc and glow discharge and the nearby velocity:

$$U(t) = \dot{V}(t) / 2E(t) \tag{1-1}$$

Here, U is the time dependent velocity, $\dot{V}$ is the rise in voltage, and E is the electric field between the electrodes.

At low to moderate velocities (< 15 m/s), the discharge is able to generate enough new electrons and ions to follow the increase in channel length smoothly and the voltage

between the electrodes increases proportionally [11]. At greater velocities, the plasma channel may reach a length at which the voltage is higher than the required voltage needed to sustain a new discharge directly across the electrodes. When this happens, a new plasma discharge will be created in the path with lowest impedance (most-commonly between the spark electrodes) and the old plasma discharge will cease to exist. This phenomenon is known as "restrike". The restriking voltage is lower than the original breakdown voltage (~ 2-4 kV) due to a sufficient number of electrons and ions that already exist at the cathode [4]. As the number of restrikes per spark event increases, the spark duration is essentially shortened [21].

A few investigations have studied spark ignition under strong flow fields. Maly studied spark discharges in air for velocities up to 45 m/s to describe the effects of turbulence on minimum ignition energy [22]. Ballal and Lefebvre obtained minimum ignition energy for fuel-air mixtures under several velocity magnitudes (0-15 m/s) in a closed-circuit wind tunnel [8]. However, this study was conducted at sub-atmospheric pressures and ambient temperatures that do not match operating conditions seen in engines. Kim and Anderson [5] used a spark anemometry method in ambient air flows (0-15 m/s) to further develop an empirical model developed by Maly et al. [6, 11, 22, and 23] to calculate the velocity across the spark electrodes. This work provided a valuable mathematical description of the plasma channel behavior for flowing mixtures, but primarily focused on a rapid method of obtaining convection velocity across the spark plug electrodes. Various spark plug orientations [16] and different intake port configurations [18] have also been used to study spark ignition for appreciable velocities (5 - 10 m/s). However, these studies did not focus on spark behavior, but rather lean

ignition and engine performance. Fansler et al. studied spark plasma centroid location in a SG-SIDI engine under late injection, but do not mention related spark characteristics [15].

1.2.2.2 Spark Behavior in Levels of Fuel-Air Concentrations

There have been a few studies that investigate spark behavior under various levels of fuel concentrations [6, 8, 9, 12, and 24,]. However, most of these studies were conducted under lean-to-stoichiometric mixtures and did not study spark behavior in overly rich mixtures as needed for SG-SIDI engines. Merer and Wallace demonstrated that spark properties, such as breakdown voltage, were affected by fuel concentration [9]. While their study only focused on lean and slightly rich fuel concentrations (Φ = 0.7 - 1.2), their findings suggest the need to continue to study spark behavior under a wide range of rich mixtures.

There have been a limited number of investigations that studied spark behavior for a wide range of well-defined fuel concentrations. Ballal and Lefebvre [8] as well as Danis et al. [25] obtained minimum ignition energies for a wide range of fuel-air equivalence ratios (Φ = 0.5 - 3). However, these studies were respectively conducted under sub-atmospheric and atmospheric pressures with ambient temperatures, neither which mimic conditions within an engine. Fansler et al. used a wide range of fuel-air equivalence ratios (Φ = 0 - 3) to develop a diagnostic tool for equivalence ratio measurements based on the emission intensity of the CN radical at 388 nm [14].

1.2.2.3 Spark Behavior for SG-SIDI Conditions

Despite previous spark ignition investigations, spark behavior under extreme high-velocity and multi-phase fuel concentrations that are seen in SG-SIDI engines under stratified operation are not well understood. Before parameters such as spark energy are used to investigate conditions of misfire, spark energy should first be well characterized under a wide range of fuel-air concentrations and flow fields created from the injection event.

1.3 Misfires in Spark-Ignition Engines

Misfires in spark-ignition engines are an important topic for automotive engineers who strive to improve fuel economy and reduce emissions in internal combustion engines. Misfire phenomena must be well characterized in order to understand how to mitigate them.

Mastorakos has reviewed the spark-ignition of turbulent premixed and non-premixed flames with their applications to misfires in IC engines [26]. For most practical purposes, the overall spark energy is the most important parameter for ignitability. For this reason, many researchers have studied the minimum ignition energy needed to ignite a given mixture in atmospheric conditions [7, 8, 25, 27, 28, 29, among others] and in engine environments [12, 13]. In turbulent flows, there is an additional heat loss mechanism from the flame kernel due to higher strain rates. This alone forces the minimum ignition energy to be higher as well as introduces a probabilistic nature of the ignition event inside the engine; essentially ignition may not be achieved even though a spark exists. Mastorakos argues that this constitutes an additional "randomness" in the

success of ignition presumably due to the effect of turbulent fluctuations of the strain rate at the moment of the spark at the spark location [26].

Misfires have been known to occur in homogenous mixtures seen under PFI engine operation [Hamai et al. 1986]. This can often be attributed to cycle-to-cycle variability of the fresh charge with trapped gases from previous cycles, which require higher spark energy to ignite. With additional turbulence, the ignition probability is reduced and the minimum ignition energy required to ignite the mixture increases.

Conditions seen to promote misfire events are exacerbated for late injection stratified operation in SG-SIDI engines. The very method of delivering the fuel to the spark plug can create unfavorable conditions for spark ignition. The injection event imposes high velocities and large velocity gradients near the spark plug at the time of spark. These high velocities near the spark plug can create multiple spark re-strikes, which rapidly changes the location of the spark plasma and shortens the spark duration [4, 21, and 31]. Local velocity fluctuations can cause undesirable spark motion and location, which can lead to rare ignition failures (misfires) and partial burns in which only a portion of the fuel is consumed. [15]. In addition large values of strain rate can indicate high scalar dissipation rates which ultimately increase heat loss from the flame and can cause flame extinction [32]. The short time duration between the injection and spark event creates highly stratified mixtures including liquid fuel near the spark plug. If the timing between the spray and spark event is not optimal, an overly rich or overly lean mixture may exist at the spark gap and can lead to a misfire or partial burn.

Researchers have employed diagnostic techniques to investigate the conditions under which misfires occur. Planar laser-induced fluorescence (PLIF) techniques have

been used in two-stroke SG-SIDI optical engines to image fuel distribution near the spark plug and have shown that cyclic variations in fuel concentration near the spark plug are large enough to cause misfires [33] LIF imaging in a wall-guided direct-injection engine showed that non-optimal spray and spark timing can cause over-mixing and overly lean mixtures that lead to misfires. Smith and Sick employed high-speed LIF fuel imaging in a SG-SIDI to gain additional insight into the temporal evolution of the fuel cloud leading to misfires [34, 35]. In these studies, lean mixtures near the spark plug was a trend among misfires. However, Smith and Sick also reported a number of misfires cycles that occurred with an ample fuel distribution near the spark plug, but no flame kernel development. For some cycles, abnormally short spark duration was argued as the leading cause of misfire. In other cycles the spark was abnormally stationary, which indicated an abnormal flow field near the spark gap. As a result, Smith and Sick suggested that there is an additional need for quantitative flow field information near the spark plug.

Mie scattering studies have demonstrated that local flow fluctuations can cause unfavorable motion and location of the spark and early flame kernel development, which can be a dominant source of random misfire events [15]. Additional Mie scattering studies have revealed that high velocities near the spark gap lead to dramatic spark stretching and frequent re-strikes which shorten the spark duration but did not show any significant correlation to misfires or partial burns [21]. Overall there appears to be a lack of quantitative flow field analysis for cases of misfire in a SG-SIDI engine. Fajardo and Sick utilized high-speed particle-image-velocimetry (PIV) in an optical SG-SIDI engine to reveal the increase of velocity magnitudes and shear strain rates before and after spray event in a region between the injector and spark plug [36]. The increase in shear strain

rate in the periphery of the spark plug, combined with fuel stratification and location of the plasma channel is argued as a potential cause to prevent flame kernel development.

1.4 Research Objective

The purpose of this research is to provide simultaneous quantitative spark discharge, flow field, and fuel concentration measurements in an operating engine in anticipation to identify the cause of errant cycles (misfire and partial burns) in a SG-SIDI engine operating under late-injection.

Despite previous spark-ignition studies, spark behavior under extreme high-velocity and multi-phase fuel concentrations that are seen in SG-SIDI engines under stratified operation is not well understood. This investigation first utilizes high-speed particle image velocimetry (PIV) to address the spark energy released under well-defined homogeneous, gas-phase, fuel-air equivalence ratios and velocity values typically seen in SG-SIDI engines. Spark energy is obtained for a wide range of homogeneous equivalence ratios (Φ = 0 - 2.9) in a SG-SIDI engine under identical flow conditions. Furthermore, spark energy is also characterized for a wide range of velocities at the spark gap ranging from 0-10 m/s in air to eliminate any influence of equivalence ratio. This data is used to interpret spark events under stratified operation.

After characterization of the spark energy, the primary focus of this research is to identify the conditions that cause misfires and partial burns under a range of external dilution levels (0% - 26% external N_2 dilution). Whereas the previous studies addressed fuel concentration and flow velocity in separate experiments, this study employs the next logical step that provides simultaneous fuel concentration and flow field measurements. A diagnostic technique is developed to simultaneously employ high-speed planar laser

induced fluorescence (PLIF) of biacetyl tracer and particle image velocimetry (PIV) to measure the fuel distribution and flow field within a SG-SIDI engine for misfire, partial burn, and well-burning cycles. Spark voltage and current measurements are additionally acquired to analyze the spark discharge characteristics of the misfire, partial burn, and well-burning cycles. Measurements are analyzed closest to the spark plug and within the entire field of view to diagnose the potential role of fuel distribution, flow field, and spark energy on misfire events.

CHAPTER 2

EXPERIMENTAL APPROACH

2.1 Optical Engine and Hardware

The engine used in this study was a single-cylinder spray-guided spark-ignited direct-injection optical engine and is shown in Figure 2-1. Full details of the engine can be found in [37]. The main components of the engine consist of a General Motors prototype, twin-cam, four overhead-valve, pentroof aluminum cylinder head, a full quartz-glass cylinder, and a quartz-glass Bowditch piston (Figure 2-1). Quartz-glass windows in the cylinder head allow optical access from the top of the pentroof to the fire-deck. The piston includes a bowl for aiding fuel stratification and can be seen in Figure 2-1. Additionally, the piston is equipped with side windows to allow optical access within the piston bowl as the piston moves up toward top-dead center (TDC). Table 2-1 provides the optical engine specifications.

Geometric Compression Ratio	9:1
Bore	86 mm
Stroke	86 mm
Displacement	500 cm^3
Connecting Rod	159 mm
Intake Valve Open (IVO)	362° BTDC
Intake Valve Close (IVC)	126° BTDC
Exhaust Valve Open (EVO)	139° ATDC
Exhaust Valve Close (EVC)	373° ATDC

Table 2-1: Engine specification of the SG-SIDI optical engine. TDC refers to top-dead-center in the compression stroke.

A multi-hole (8-hole) injector is mounted slightly off the cylinder axis, while a double-pinned spark plug is mounted on the opposite side of the cylinder axis. One of the holes of the injector was aimed at the spark plug to provide a spray plume that impacted the spark plug gap and is shown in Figure 2-1. A piezo pressure transducer (Kistler 6125A) is secured to the side of the cylinder head to provide in-cylinder pressure measurements at crank-angle resolution. Figure 2-1 shows the cylinder head with all its features, including spray plume direction and the location of the laser sheet.

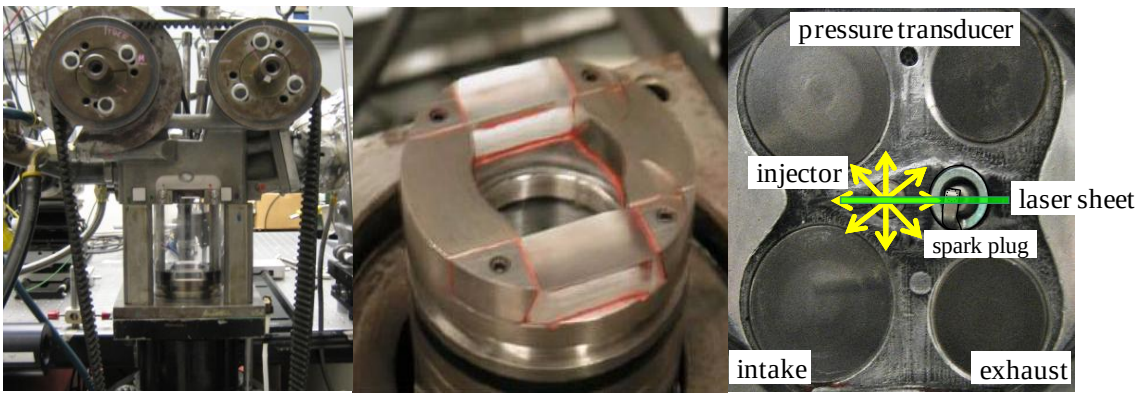

Figure 2-1: Single-cylinder optical engine (left), view of dished shaped piston bowl showing quartz-glass bottom and side windows (middle), view of cylinder head (from view of piston) (right) highlighting its components, general spray plume direction of the injector, and location of the laser sheet.

The cylinder head is thermally controlled by liquid coolant and oil that circulate through the cylinder head. The coolant and oil temperatures were set to 90°C for all

experiments. Air jets are used to cool the quartz-glass cylinder. This cooling method is not sufficient to thermally maintain the quartz-glass temperature below a specific limit (100^{o}C). Ultimately the lack of cooling for the cylinder limits the run time of the engine during a given experiment. The piston is sealed to the cylinder by two sets of graphite piston rings. The top rings are spring loaded to provide a seal to the cylinder, while the bottom rings are used to guide the piston movement. As graphite provides self-lubrication, additional lubrication between the piston and cylinder is not used. Blow-by past the piston rings is significant and found to be on the order of 10% of the trapped mass [38].

Intake air is metered through a critical orifice system upstream of the intake plenum. The pressure upstream the critical orifice is regulated to control the air flow rate through the critical orifice to give a specific intake manifold pressure, MAP. Additionally, air seeded with silicon oil droplets (Dow Corning 510R) is introduced into the air upstream the intake plenum, but downstream the critical orifice system. A six jet atomizer (TSI model 9306) is used to produce silicon oil droplets with 1μm diameter. Air flow rate into the atomizer is measured by a mass flow controller (FMA 5500/5400). The use of the critical orifice system and flow meter for seeded air provides an accurate measurement of flow into the engine under steady state operation. The intake plenum and piping downstream the critical orifice system are equipped with a series of heaters to regulate the temperature of the intake air.

The engine is equipped with a set of encoders to indicate the positioning of the piston during each revolution. A Hall-effect sensor is used with the engine flywheel to

indicate each crank-angle degree (CAD) of the piston, while another Hall-effect sensor is used with the cam flywheel to indicate the occurrence of a new engine cycle.

2.2 Optical Setup

The optical setup used for this investigation was used to simultaneously obtain particle image velocimetry (PIV) and planar laser induced fluorescence (PLIF) measurements in a SG-SIDI engine. The optical setup used is shown in Figure 2-2. A frequency-doubled 527 nm Nd:YLF dual cavity laser (Quantronix Darwin Duo) was used as the light source for Mie scattering. Each laser beam was circularly polarized and had a diameter of ~ 15 mm. At 4.8 kHz, each laser beam provided 5.9 mJ of energy per pulse. A frequency-tripled Nd:YAG 355 nm laser (Quantronix Hawk II) was used for the fluorescence measurements. The UV laser beam was linearly polarized and had a diameter of ~ 5 mm. At 4.8 kHz the laser provided 1.4 mJ of energy per pulse.

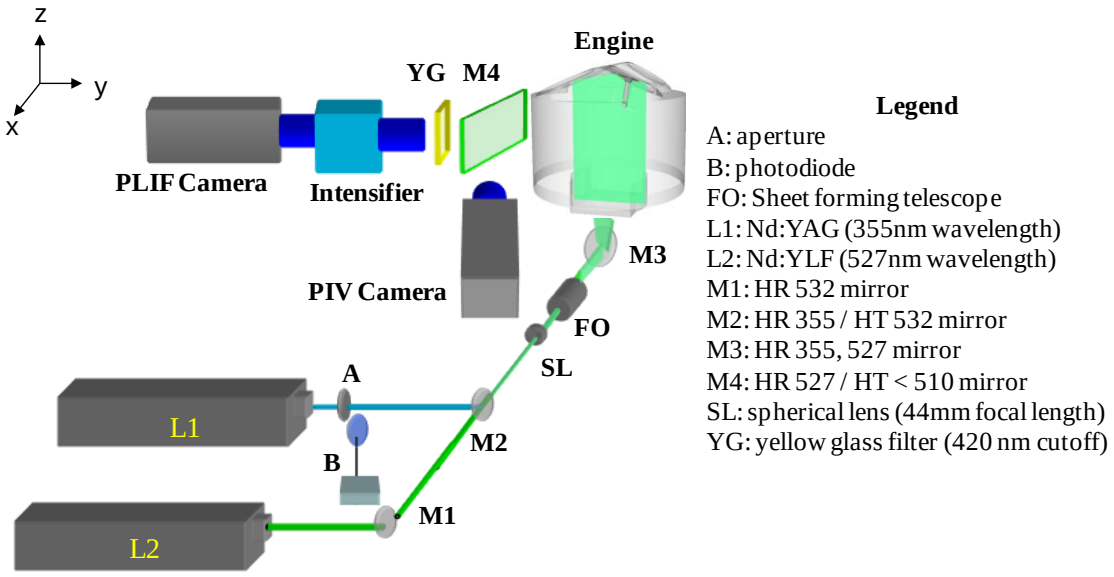

Figure 2-2: Optical setup for combined PIV-PLIF measurements.

The optical setup used to deliver the laser light into the combustion chamber was optimized so that the UV and green laser sheets were of comparable thickness and focused on the same region of interest. A high-reflectivity (HR) 355 nm, high-transmissivity (HT) 532 turning mirror was used to reflect UV laser light towards the engine, while allowing the green laser light to pass through. This combined the UV and green laser beams in the same optical path towards the engine. A spherical lens was used to focus the laser beams into a telescope with a set of cylindrical lenses (LaVision) to form a laser sheet. The laser sheets entered an opening within the extended crankcase and were reflected off a 45^{o} UV dichroic mirror. The vertical laser sheets were aligned with the tumble plane and bisected the fuel injector and spark plug as shown in Figure 2-1. The higher intensity region of each laser sheet was aligned directly downstream (to the right) of the spark plug to provide as much light as possible for Mie scattering and fluorescence at this location. Optical components were positioned to produce similar light sheet thicknesses (1 mm) for both the green and UV laser sheets at the location of the spark plug ground strap. The UV laser sheet had a slightly smaller width (~ 20 mm) than the green laser sheets (~ 35 mm) due to the smaller beam diameter.

A 12-bit CMOS camera (Vision Research Phantom V7.1) was used to capture the Mie scattering of green light off of silicone oil droplets (~ 1μm diameter), while a 14-bit CMOS camera (Vision Research Phantom V7.3) equipped with a lens-coupled image intensifier (LaVision HS-IRO) was used to capture the fluorescence of the biacetyl component of the fuel mixture. The fluorescence signal was focused onto the intensifier with a Nikon 105 mm (f# 1.2) lens. The Mie scatter and LIF light were separated by a dielectric mirror, M4, that reflected light at 527 nm (Mie scattering), but transmitted

below 510 nm (LIF signals). This was placed between the engine and the PLIF camera at a 45^{o} angle, thereby allowing both cameras to image perpendicularly to the laser sheet in the tumble plane. A yellow glass filter was placed in front of the intensifier to mitigate Mie scattering of droplets below 420 nm. The experimental parameters used for the combined PIV / PLIF optical setup are presented in Table 2-2.

The magnification of the PIV camera (0.53) was double the magnification of the PLIF camera (0.25) and was determined by:

$$Magnification = \frac{distance\ from\ lens\ to\ image}{distance\ from\ lens\ to\ object} \quad (2\text{-}1)$$

In order for the PIV camera to operate in frame straddling mode and be able to capture a large number of consecutive cycles (> 300), the original size of the PIV camera chip (800 pixels x 600 pixels) was reduced to 447 pixels x 352 pixels, while the PLIF camera was able to utilize the entire 800 pixel x 600 pixel region. Despite the large difference in the magnifications between the two cameras, the differences in the camera chip size create a distance per pixel that is comparable between the PIV and the PLIF images.

The depth of focus for the PLIF camera (0.3 mm) is smaller than the thickness of the UV laser light sheet (1 mm) which can often question the quality of the fluorescence image. The smaller depth of field is the result of a wide-open aperture of the PLIF camera lens which was set to capture as much fluorescence light as possible. However, the loss of spatial resolution in LIF images is much smaller than the analysis region over which data were spatially averaged for the purpose of this work.

PIV		PLIF	
Parameter	Value	Parameter	Value
Magnification	0.53	Magnification	0.25
Depth of Focus	1.1 mm	Depth of Focus	0.3 mm
Aperture / f#	8	Aperture / f#	2.8
Distance per pixel	0.086 mm	Pixel Size	0.075 mm
Spatial Resolution (based on 32x32 pixel region)	2.85 mm x 2.85 mm	Spatial Resolution (based on 5x5 pixel region)	0.37 mm x 0.37 mm
Vector Spacing	1.4 mm	Camera exposure time	200 μs
Vector Spacing	1.4 mm	Intensifier gain	2000 count / photo electron
		Intensifier exposure time	300 ns

Table 2-2: Experimental parameters for the combined PIV / PLIF optical setup.

A photodiode (LaVison) was used to capture UV light reflected off the spherical lens to provide a measure of the UV laser energy during the course of the experiment and from experiment to experiment.

A high-speed controller (LaVision) was used in conjunction with the imaging system (LaVision - DaVis) to control the timing of the cameras and lasers and their synchronization with the engine. Trigger signals, from the Hall-effect sensors, were sent to the high-speed controller to indicate each crank-angle degree and new engine cycle. Each laser fired once during every crank-angle giving three laser pulses per crank-angle degree, i.e. at a frequency of 4.8 kHz. The PIV camera operated in frame-straddling mode at 9.6 kHz, splitting each CAD into two temporally equal frames of 104 μs. The UV laser fired 24 μs after the second green laser pulse. The intensifier gate was opened for 300 ns and the PLIF camera captured the fluorescence image with an exposure time of 200 μs. The time delay between the two green laser pulses depended on the ability to capture the flow field inside the engine. For images that included the injection event, the time delay between the green laser pulses was 20 μs. For images that did not include the injection

event (e.g. early injection or no injection) the time delay between the green laser pulses was 62.5 μs.

Within this investigation, spark energy released was characterized in the engine for a wide range of homogeneous fuel-air distributions and for a wide range of flow fields without the presence of fuel. For these experiments, PLIF measurements were not necessary and only flow field images were acquired. Therefore, the optical setup shown in Figure 2-2 was simplified; the PLIF equipment was removed and the PIV camera was oriented perpendicular to the light sheet in the tumble plane. As a result, the PIV camera was closer to the engine had had different optical parameters. The optical parameters used for PIV-only experiments are shown in Table 2-3.

PIV-only Experiments	
Parameter	Value
Magnification	0.95
Depth of Focus	1.07 mm
Aperture / f#	11
Pixel size	0.052 mm
Spatial Resolution (based on 32x32 pixel region)	1.7 mm x 1.7 mm
Vector spacing	0.85 mm

Table 2-3: Experimental parameters for PIV-only experiments.

2.3 Spark Measurement Diagnostics

An inductive ignition system was used, which delivered the current to a double-pinned resistive spark plug (NGK) with a 1.3 mm gap spacing. Spark voltage was measured at the top of the spark plug by a high voltage probe (Tektronix model P6015A), while the spark current was measured using a current monitor (Pearson Model 110). Spark voltage and current signals were digitized with a high-speed digitizer (National Instruments PXI/PCI-5105) at a sampling rate of 500 kHz. The spark current was sent

through an amplifier before digitization. The amplifier had an amplification of 151x and a bandwidth of 860 kHz, which was well above the digitization rate.

Spark energy delivered to the spark gap was calculated as:

$$E_{spark} = \int_{\text{spark duration}} \left[V_{probe} - I * R_{plug} * I \right] dt \tag{2-2}$$

where V_{probe} is the voltage recorded form the high-voltage probe at the top of the spark plug, R_{plug} is the internal resistance of the spark plug, and I is the spark current. The internal resistance of the spark plug, 4.6 kΩ, was measured with an ohmmeter. The spark energy was calculated throughout the duration of the spark event. The onset of spark began when the spark voltage and current values both became negative and the duration of the spark event lasted until the spark current value was no longer negative.

2.4 Experimental Procedure

A set of three engine runs were conducted for a given experiment to obtain Mie scattering and fluorescence images. These images were then processed into vector fields and fuel concentration measurements. For each run, the cameras imaged during the same crank-angle regime (e.g. 44^o BTDC – 5^o ATDC) for each a specified number of engine cycles. After each run, the engine was spun down and the images were saved. The first run consisted of 75 cycles of background images for both the PIV and PLIF images. Here, fuel injection and seeding were not used and only the lasers were fired to provide an averaged background image used to subtract background noise. The second run consisted of what will be denoted as the lightsheet images. This run consisted of 100 cycles used for averaged cycle analysis and was used solely for the PLIF processing

routine to normalize the fuel concentration with the late injection run. The lightsheet images corrected for light-sheet intensity variations and provided LIF intensity calibration to fuel concentration. Here a fixed amount of fuel (9.6 mg/cycle) was injected early within the intake stroke (300^o BTDC) to produce a quasi-homogeneous fuel-air mixture within the combustion chamber. Seeding was not used for this run and only the PLIF camera and intensifier were used to acquire images. Finally, the third run consisted of 348 consecutive cycles for the experiment of interest – combined PIV and PLIF measurements under late-injection and stratified charge. Here seeding was introduced into the intake air for PIV measurements and fuel was injected late within the compression stroke (37^o – 32^o BTDC).

For the experiments only requiring flow field images, the lightsheet images were not needed. Therefore, only background images and the experiment-of-interest images (e.g. flow field during the spark event) were obtained.

2.5 Data Processing

2.5.1 PIV Measurements

A commercial imaging software program (LaVision DaVis 7.2) was used for processing the PIV and PLIF images. Unwanted scattered light off surfaces such as the cylinder head and spark plug were removed by subtracting the cycle-averaged background images from the raw Mie scattering images. The two Mie scattering images per crank-angle were then cross-correlated with decreasing size multi-pass iterations. An initial window size of 128 x 128 was reduced to a final window size of 32 x 32 with 50% overlap and two passes for each reduction in window size. The 32 x 32 interrogation

window corresponds to a 1.7 mm x 1.7 mm region for the PIV only experiments, while this region corresponds to a 2.85 mm x 2.85 mm region for the late injection experiments. With 50% overlap, vectors are shown every 1/2 of the interrogation window region.

During post-processing, the peak ratio factor, *Q*, was set to 1.8 to improve the accuracy of the vector computation. Spurious vectors present in the original field were eliminated by using a 4-pass regional median filter (Davis's "strongly remove and iteratively replace" median filter). During the first two passes, this filter removed vectors which had *x* and *y* vector components that differed greater than $U_{median} \pm 3U_{rms}$ of its neighboring vectors. The third pass re-inserted vectors with the average weight of its neighboring vectors if the vector was within $U_{median} \pm 4U_{rms}$ of its neighboring vectors. Since the vectors remaining from the first two passes are assumed to be valid vectors, it was feasible for the re-inserting vectors criteria to have a larger standard deviation from the median value. This procedure removed spurious vectors while preserving vector gradient information. A 3x3 Gaussian smoothing filter was applied to the vector field to remove noise at spatial scales near the resolution limit of PIV measurements [39].

2.5.1.1 Uncertainty in PIV Measurements

PIV relies on detecting particle motion to calculate velocity. There are two main sources of uncertainty in digital PIV: random error and bias error. The ability to obtain reliable velocity field data with minimal uncertainty depends largely on parameters such as tracer particles, optical medium, camera settings, and choice of PIV algorithm (i.e. image interrogation technique, post-processing, etc.). Previous work has addressed identifying and optimizing experimental parameters that minimize uncertainty associated with digital PIV. In this section a brief description of each parameter will be described

with respect to reliable flow field calculations. Optimum parameters found from previous research and used in this investigation will be presented as well as their respective uncertainties.

Tracer particles need to accurately follow the instantaneous flow motion. Atomization of silicone oil droplets with 1 μm diameter provides a particle density that is significantly greater than air and a specific gravity close to unity, which according to Melling [40] is sufficient to have a 95% response to turbulent frequencies well above what can be resolved in the engine [41]. An optimum seeding density of 8-10 particle pairs for a 32 x 32 pixel interrogation regions was suggested by Keane and Adrian [42] and later verified by Megerle et al. [43] to approximately gives a 2% uncertainty of the local average pixel displacement. In addition, it is strongly suggested that the maximum particle displacement is no more than ¼ of the final interrogation window size [42] to prevent loss of in-plane particle pairs. A bias error could also be introduced if the particle displacement is too small (< 1 pixel displacement), but has been shown to be less than 1% in a 32 x 32 pixel interrogation region [44].

Full optical access in a research engine is typically led by a transparent glass cylinder. The curvature effects from the quartz glass cylinder impact the accuracy and precision of the PIV data from an engine. Reuss et al. demonstrated a decrease in accuracy up to 10% near the wall of a curved cylinder, while precision errors, quantified by the RMS displacement, varied between 3.5% and 5% of the local mean velocity [45]. These errors were attributed to out of focus particles and an insufficient amount of light near the cylinder wall. In other experiments, Funk has calculated uncertainty of flow velocities for a field of view in the center of the optical cylinder [46]. Based on a mean 8

pixel particle displacement, Funk quantified the RMS displacement noise as 0.1 and 0.15 pixels for f/11 and f/16, respectively, which corresponds to a 1.25% uncertainty in measured velocity.

Obtaining accurate PIV data can be highly sensitive to the imaging equipment used. Particularly it is important to have as much light as possible with the greatest depth of field for highest quality particle images. Megerle et al. have demonstrated that RMS error increases with a decreasing f-stop (increasing aperture) of the camera.

The fundamentals of digital PIV have been reviewed by Westerweel [44]. The reader is referred to [44] for a complete description of the parameters used to obtain reliable PIV data. Westerweel noted that the use of fast Fourier transform with zero padding is a viable algorithm to provide reliable PIV data. In previous study Westerweel also demonstrated the local-median filter was most efficient for removal of spurious vectors in PIV data [47]. With use of these algorithms, the uncertainty is reduced and usually depends on a bias error termed as peak-locking [44]. Peak-locking is often defined as a bias towards the closest integer value for pixel displacement. This is more predominant for cases of small particles in relation to interrogation window size as well as small particle displacements. A spatial offset between interrogation windows has been shown to avoid pixel-locking effects [44].

For the experiments presented in this study, imaging operating parameters were optimized to obtain reliable, accurate PIV data with minimal uncertainty. Seeding density was set to have 8-10 particle pairs in a 32 pixel x 32 pixel interrogation window. For experiments with late injection the green laser pulses were separated by a time delay of 20 μs, which provides the capability to measure velocities up to 30 m/s based on a

maximum particle displacement of 8 pixels (1/4 final interrogation window). For experiments without injection, the laser pulses were separated by a time delay of 62.5 μs to accurately measure a velocity range from 0.5 – 8 m/s. The PIV camera operated with an f-stop number of 8 to provide an average particle intensity count greater than 200 counts and a depth of field greater than the light sheet thickness (1 mm). Averaged background images were subtracted from the raw Mie scattering images to remove scattered light off of solid surfaces such as the cylinder head and spark plug. These images were then preprocessed with a sliding subtracting background of 10 pixels to further reduce noise. During PIV processing, the cross correlation method employed a multi-pass (2 passes) decreasing window size algorithm that cross correlated particle pairs with an initial interrogation window size of 128 x 128 pixels and reduced to a final window size of 32 x 32 pixels with 50% overlap. The multi-pass decreasing window size provides a window shift that adaptively improves the computation of the vectors as well as the spatial resolution of the vector field, resulting in a more accurate and reliable calculation of the velocity field. In addition, a peak ratio factor, *Q*, was set to 1.8 to improve the accuracy of calculating the particle displacement. For post-processing, a local-median filter was used to efficiently remove spurious vectors within the flow field while preserving velocity gradient information as suggested by Westerweel [48]. With this optimization of the experimental setup and PIV processing routine, the uncertainty in the resulting velocity vectors is calculated from the uncertainties reported in previous literature. Using the sum of squares approach the uncertainty in the velocity calculation for these measurements is 4%. Uncertainty in velocity calculation can be higher with out of plane motion which can typically be seen during the spray event and for combustion.

2.5.2 PLIF Measurements

UV laser energy was measured with a photodiode to quantify shot-to-shot variations and provide an average laser energy measurement for each set of images (e.g. background, lasersheet, and late injection images) within an experiment. Background and lasersheet averaged photodiode measurements were divided by the averaged late injection photodiode measurement and used to normalize averaged background and lasersheet images to correct for any differences in average UV laser energy between the set of images. Scattered light from surfaces such as the cylinder head and spark plug was removed from the late injection and lightsheet images by subtracting the averaged background images. The late injection images were then normalized by the lightsheet images to provide a scaled signal representation of equivalence ratio (Φ). It has been demonstrated that normalization of the late injection images by images of known and homogeneous fuel concentration provides a LIF signal that becomes a representation of the equivalence ratio [34, 49, and 50]. Normalizing of these images also accounts for pressure and temperature dependencies of the LIF signal from the biacetyl and laser light sheet inhomogeneities [34]. A non-linear sliding average filter of size 5 pixels was applied to the late injection fuel distribution image to smooth the fuel concentration within the region of 5 x 5 pixels (0.37 mm x 0.37 mm). A mask was used to remove saturated signals in such regions as the cylinder head. In addition, a dynamic mask was used to exclude the high intensities from the spark plasma when extracting fuel concentration measurements near the spark plug. The vector field was then overlaid onto the processed PLIF images and an overlay was used to clarify the position of the significant features such as the spark plug and injector.

2.5.2.1 Uncertainty in PLIF Measurements

Uncertainty in biacetyl LIF measurements for fuel distributions has been investigated by Smith and Sick [50]. Two main sources of uncertainty in the PLIF measurements are bias error and noise [38]. Bias error accounts for factors that affect the measurements in a certain direction, while noise ultimately includes variances from image to image that may appear random. Sources of each type of error will be presented along with their approximate contribution to the total PLIF measurement uncertainty.

Biased error is mainly introduced through variations of in-cylinder pressure and temperature. Smith and Sick have demonstrated the dependence of LIF signal strength of biacetyl on temperature and pressure [50]. Slight cycle-to-cycle variations of in-cylinder pressure are often due to slight variances of intake manifold pressure. A difference up to 1.5 kPa was found in the intake manifold pressure during the course of these experiments. This can cause a pressure difference of 15 kPa near top-dead-center (TDC). Analyzing the results from Smith and Sick, the LIF signal strength can vary within 1% as a result of these pressure fluctuations. In a similar manner, intake air temperature can vary from 40^{o}C to 50^{o}C during the course of an experiment. This variation can cause a temperature difference within 10 K during the time of imaging. From Smith and Sick this contributes to a ± 2.5 % variation in LIF signal intensity. A more drastic source of local in-cylinder temperature differences is attributed to evaporative cooling of the fuel. Beyrau et al. have shown that local temperature can drop up to 20 K in the region near the spray plume as a result to evaporative cooling [51]. This temperature difference would give a bias error of 4.5% according to Smith and Sick. Using a root-mean-squared (RMS) approach, the total bias error of the LIF measurements obtained in this work is 5%.

Noise can attribute to a much larger portion of the total LIF measurement uncertainty. According to previous work, there are two sources of error due to noise: shot noise and image-to-image variation in LIF signal intensity [38]. Shot noise is considered as the measured variation of LIF signal in a region that should theoretically have uniform intensity. The procedure for calculating this error is the same found in [38] and is briefly summarized. A small region (10 x 40 pixels) within a set of early-injection images (lightsheet images) at the same crank-angle was extracted. The RMS variation within this region was normalized by the spatial average of the same region. This was done for a 100 cycle experiment resulting in a 100 cycle ensemble average. The resulting shot noise was found to contribute to variations up to 20%. This is larger than what was found in previous LIF investigations [38 and 50] and can be attributed to a different region of interest, or perhaps from a slightly-aged intensifier. Image-to-image variation was found by obtaining a 100 cycle ensemble-averaged and RMS image of a selected region within the lightsheet image at a given crank-angle. The region selected depicted the region covered by the UV light sheet. The RMS value was normalized by ensemble-spatial average and was found to be up to 6%.

Using the sum-of-squares approach, the total LIF measurement uncertainty was found to be ± 21%. The biggest contribution of this uncertainty is from shot noise. This is often the case when high gain levels are used with the amplifier when working with low levels of available laser energy. Although this uncertainty may appear large, it is still well within the uncertainty of other diagnostic techniques used in engine research.

2.5.3 Engine Performance Parameters

Engine performance parameters are computed from the in-cylinder pressure, which is recorded with crank-angle resolution using an A & D Technology Phoenix data acquisition system and analyzed using the A & D CAS software. The main parameters of interest are indicated mean effective pressure (IMEP) and coefficient of variance (COV) of IMEP. These parameters accurately describe the combustion performance within the engine. The CAS software utilizes a post-processing program (Post Processing Pro – A & D Technology) that is equipped with a Rassweiler-Withrow heat release code [52] that is capable of calculated mass-fraction burned (MFB) and other important heat release parameters.

CHAPTER 3

SPARK ENERGY RELEASED FOR WELL-DEFINED FUEL-AIR EQUIVALENCE RATIOS AND FLOW FIELDS

3.1 Introduction

Knowledge of spark behavior under conditions relevant to late-injection stratified-operation is crucial when investigating ignition phenomena inside a SG-SIDI engine. As mentioned in chapter 1, spark energy released under the range of fuel-air mixtures and flow fields typically seen in a SG-SIDI engine is not well characterized.

This chapter presents data of spark energy released under well-defined homogeneous, gas-phased, fuel-air equivalence ratios as well as flow fields typically found under stratified charge operation in SG-SIDI engines. For a better understanding of spark behavior, it is necessary to separate the effects of fuel concentration and flow field information on the spark energy released. Two investigations were conducted to address this concern. In the first investigation, spark energy was characterized for a wide range of homogenous equivalence ratios ($\Phi = 0 – 2.9$) in a SG-SIDI engine under identical flow conditions. In the second investigation, a fuel injector was used as an air injector during motored engine operation to produce injection-like flows near the spark plug in an un-fueled (air only) charge. For these experiments, spark energy was characterized for a

wide range of velocity values (V = 1 - 10 m/s), shear strain rate values ($|\sigma|$ = 100 - 1500 1/s), and vorticity values ($|\omega|$ = 100 - 3000 1/s).

This chapter organized as follows. The experimental procedure used for each set of experiments is presented first. The results section is then presented and begins with an explanation of the in-cylinder region where flow field quantities were extracted. Other important factors such as the reliability of the ignition system and the effect of seeding on spark properties are then briefly presented. The results section continues with characterization of spark energy with equivalence ratio, flow velocity, shear strain rate, and vorticity. A short discussion highlighting the significance and application of this analysis is then given. Finally, the summary of these experiments is provided in a conclusion section.

3.2 Experimental Method

3.2.1 Homogeneous Fuel Concentration Experiments

Spark energy was measured under a wide range (Φ = 0 - 2.9) of well-defined fuel-air equivalence ratio in the gas phase. Here, fuel was injected into the cylinder during the intake stroke (end-of-injection (EOI) = 300^{o} BTDC) allowing adequate time for fuel-air mixing to provide a homogeneous fuel-air mixture during the compression stroke and at spark timing. A previous investigation [53] has demonstrated that early injection produces a reasonably homogeneous mixture for this engine with variations on the order of 5% or less. The fuel injector operated at a fuel pressure of 110 bar and was calibrated to provide an accurate amount of fuel at a specified injection duration. The intake air flow was controlled by a critical-orifice system. An atomizer (TSI 9306) was used to seed the

intake air with silicone oil droplets for PIV measurements. The atomizer air was introduced downstream of the critical orifice system and a flow meter was used to measure the additional air flow rate into the engine. Controlling and measuring the fuel and air into the cylinder gave a reliable means to calculate the equivalence ratio with an accuracy of $\Phi = \pm 0.05$.

It was desired to have a well-defined fuel-air mixture without the presence of residual combustion products within the cylinder at the time of spark. Especially for very lean and rich mixtures, high cycle variability my occur leading to variations in residual gas composition. Combustion products such as CO_2 and H_2O can influence spark behavior [Merer and Wallace 1995] and their presence could interfere with the goal of these experiments. Therefore, the engine ran under skip-fired operation (fire 1 in 3 cycles) allowing two motored cycles in between each fired cycle to scavenge residual gases and reduce the presence of combustion products within the cylinder during fired cycles.

Operating parameters for the fuel concentration experiments are shown in Table 3-1. Intake air was throttled to an inlet manifold absolute pressure (MAP) of 50 kPa in order to avoid window damage from high peak cylinder pressures (> 4000 kPa) that result from combustion of stoichiometric and rich mixtures at wide-open throttle (MAP ~ 95 kPa). To match in-cylinder pressures (10 bar) and temperatures (725 K) at spark timing for throttled operation to that unthrottled operation (i.e. stratified operation in an SG-SIDI engine), the onset of spark was triggered at 5^o BTDC. Thus, the spark timing was chosen strictly to create a similar operating environment during spark timing to that of unthrottled operation and not to optimize combustion performance.

The fuel used in this experiment was 90% isooctane, 10% biacetyl by volume. This is the standard fuel mixture used in this engine for fuel fluorescence experiments. Even though laser induced fluorescence techniques were not applied in these experiments, it was important to keep the fuel mixture consistent for comparison with late injection measurements described later within the overall investigation.

Experiments consisted of 100 fired cycles (300 total cycles) and each experiments was repeated three times to give a total of 300 cycles of spark events at a given fuel-air equivalence ratio, ranging from $\Phi = 0 - 2.9$. The PIV camera acquired two Mie scattering images per crank-angle from 10^{o} BTDC – 19^{o} after top-dead-center (ATDC). The time delay between each laser pulse was set to 62.5 μs to adequately capture the flow field when the piston was near TDC and provided a maximum pixel shift that was within ¼ of the final interrogation window size (32 pixels x 32 pixels) [54].

Parameters	Fuel concentration experiments	Velocity Field Experiments
Engine Speed	800 RPM	
Manifold Absolute Pressure (MAP)	50 kPa	95 kPa
Spark Timing	5 BTDC	30 BTDC
Spark Dwell Time	3.5 ms	
Injection Timing (Physical EOI)	300 BTDC	31 BTDC
Injection duration	0, 1.0, 1.25, 1.5, 1.75, 2.0, 2.25, 2.5, 2.75, 3.0, 3.25, 3.5, 3.75, 4.0 ms	1.5 ms
Injection Pressure	110 bar	0, 14, 28, 55, 80, 110, 140 bar
Fuel	90% isooctane 10% Biacetyl	None
Intake temperature	45^{o} C	
Oil and Coolant temperature	90^{o} C	
Image Timing	10^{o} BTDC – 19^{o} ATDC	44^{o} BTDC – 5^{o} ATDC
PIV time delay	62.5 µs	20 µs (air injection) 62.5 µs (no injection)

Table 3-1: Operating parameters for the fuel concentration and air injection experiments performed in the optical SG-SIDI engine.

3.2.2 Defined Air Flow Experiments

Spark energy was measured under a range of velocities (0 – 12 m/s). This range is typically seen near the spark plug during the late state of the injection events in SG-SIDI engines [55]. Experiments were conducted in an un-fueled (air only) charge to isolate the effects of velocity. A high-pressure fuel injector was used to inject dry compressed air and to produce high velocities at the spark plug while maintaining the air-only charge.

The injector used for air injection was an 8-hole fuel injector with a 270^{o} hole pattern, rather than the fuel injector with the 360^{o} hole pattern used in the fueled experiments. The injectors with their respective hole patterns are shown in Figure 3-1.

The new fuel injector was used for air injection to eliminate the risk of overheating and possibly damaging the regular fuel injector used in the liquid fueled experiments. The injector used for air injection is referred to as the air injector throughout this investigation. One of the holes of the air injector was aligned with the center electrode of the spark plug to provide a jet that impacted the spark plug. This exposed the spark plug to the highest velocities from the injection event. A range of air injection pressures from 0 (no injection) to 140 bar was used to vary the velocity at the spark plug.

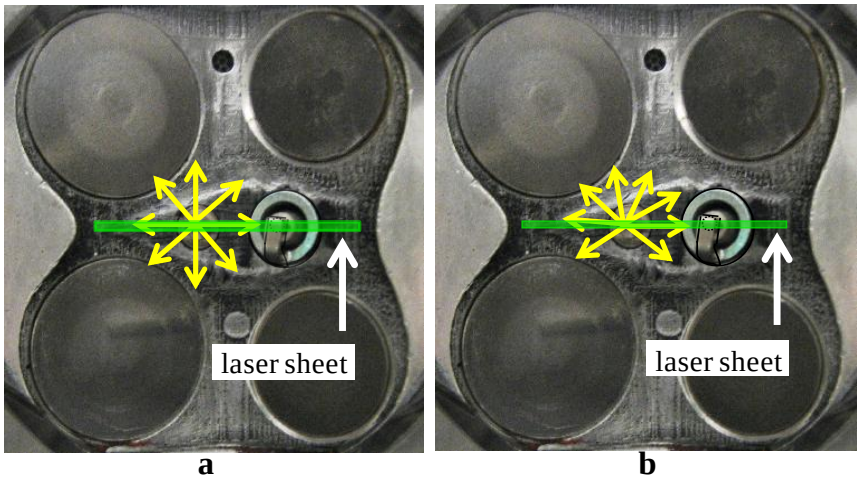

Figure 3-1: a) the fuel injector used for fuel injection experiments was an 8-hole injector with a 360^{o} hole pattern, b) the air injector used for the flow field experiments was an 8-hole injector with a 270^{o} hole pattern. Injector nozzles were aligned with the spark plug center electrode to provide an impacting spray configuration.

Operating parameters for the air injection experiments are shown in Table 3-1. Experiments were performed for multiple injection pressures ranging from 0-140 bars to give a wide range of velocities at the spark plug. The physical EOI was set to 31^{o} BTDC with an injection duration of 1.5 ms. The onset of spark was set to 30^{o} BTDC and was chosen to match that used under stratified-charge operation.

Each experiment consisted of 150 consecutive cycles with injection and spark. Each experiment was repeated once to provide 300 spark events under a specific flow

field from a given injection pressure. Since no fuel was injected, PIV was the only optical diagnostic technique utilized for these experiments. Mie scattering images were acquired from 44^{o} BTDC to 5^{o} ATDC for each cycle. For operation with without air injection, the time delay between the two laser pulses was set to 62.5 μs. For operation with air injection, the time delay between the two laser pulses was shortened to 20 μs in order to resolve the higher velocities from the air injection.

3.3 Results

3.3.1 Selection of In-Cylinder Measurement Location

Throughout this study the impact of fuel concentration, velocity, shear strain rate, and vorticity on available spark energy is investigated. Ideally, these quantities should be measured directly along the three-dimensional extension of the plasma channel. Unfortunately, this is experimentally not feasible. Therefore, the option is explored to spatially average named quantities in an area that typically contained the spark plasma. Due to both the directed tumble flow and the impact of the fuel spray onto the spark plug electrodes, there is a strong preferred direction for the spray-induced flow; the spark plasma either stays between the electrodes or extends along the original direction of the spray plume as indicated in Figure 3-2. Therefore, it is suitable to extract named quantities in a region directly downstream of the spark plug (to the right of the spark plug in Figure 3-2).

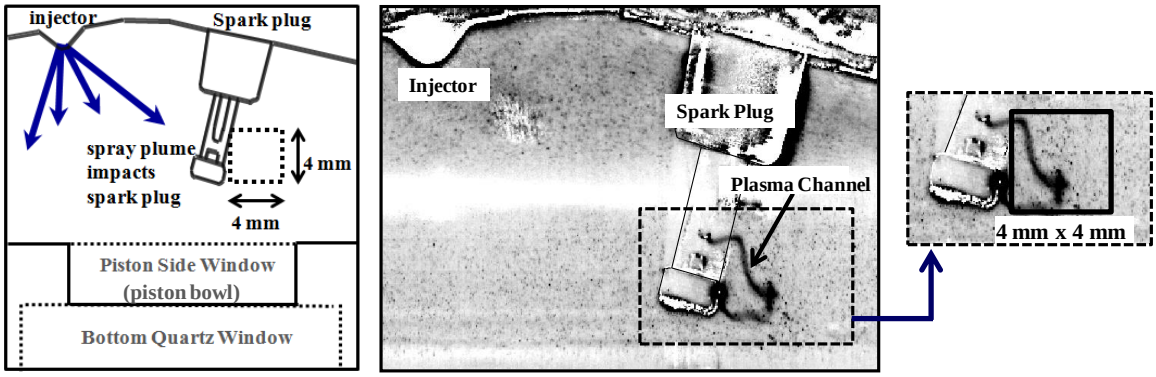

Figure 3-2: Spark plasma is swept out from the spark plug from the spray induced flow. A 4 mm x 4 mm region downstream the spark plug was found to be the optimum location to extract flow field information to relate to spark behavior.

It is found that a 4 mm x 4 mm region downstream the spark plug (Figure 3-2) is best-suiting for extracting quantities near the spark plug. This region was large enough to contain the whole plasma channel as it stretches beyond the spark electrodes. In addition, the size of this region provides an adequate sample of velocity vectors for both the PIV-only experiments and the combined PIV-PLIF experiments. The sensitivity of the extracted spatially averaged magnitudes of velocity, shear strain rate, and vorticity is investigated by varying the size of the extraction window. This analysis is presented in Appendix A. Differences are significantly lower than the cycle-to-cycle variations, confirming the validity of the selected 4 mm x 4 mm region.

3.3.2 Baseline Experiment – Spark in Quiescent-Ambient Air

A baseline experiment was conducted to access the repeatability of the ignition system. The engine was stationary and cylinder head was raised to provide an environment in open air. The engine set-point controller (ESC) was set to automate, which gave a trigger signal command to the spark plug to initiate the spark event. The trigger signal was sent every 208 µs to simulate the time duration between each spark

event when the engine operated at 800 RPM. A total of 400 spark events were obtained to evaluate the repeatability of the ignition system. All spark parameters, such as dwell time remained the same as the engine experiments.

The repeatability of spark energy and spark duration was assessed. The ensemble-averaged spark energy was calculated to be 19.6 mJ with a standard deviation (1 σ) of 0.8 mJ, while the ensemble-averaged spark duration was determined to be 3.1 ms with a standard deviation (1 σ) of 0.1 ms. Under these baseline conditions, the spark energy is repeatable within 4%, while the spark duration is repeatable within 3.2%.

3.3.3Seeding Particles on Spark Behavior

The effect of seeding on specific spark properties was evaluated to ensure that the introduction of PIV seeding particles did not influence spark behavior. Three seeding conditions were studied in the engine: 1) No seeding, 2) PIV seeding, and 3) Over-seeded. PIV seeding was the seeding density used in the PIV experiments and over-seeded was the condition which used a seeding pressure (air pressure into atomizer) x5 times that needed for PIV seeding conditions. Experiments were conducted with the same engine parameters for the velocity field experiments presented in Table 3-1. At each seeding condition, 300 spark events were analyzed.

Silicone oil seeding particles did not influence spark energy and duration. Figure 3-3 clearly shows that spark energy and duration are agreeable within uncertainty for all three conditions. Bars shown in Figure 3-3 represent one standard deviation of the 300 spark events at each given condition. These results provided confirmation that seeding would not influence spark behavior as different seeding densities are needed under different fueling rates.

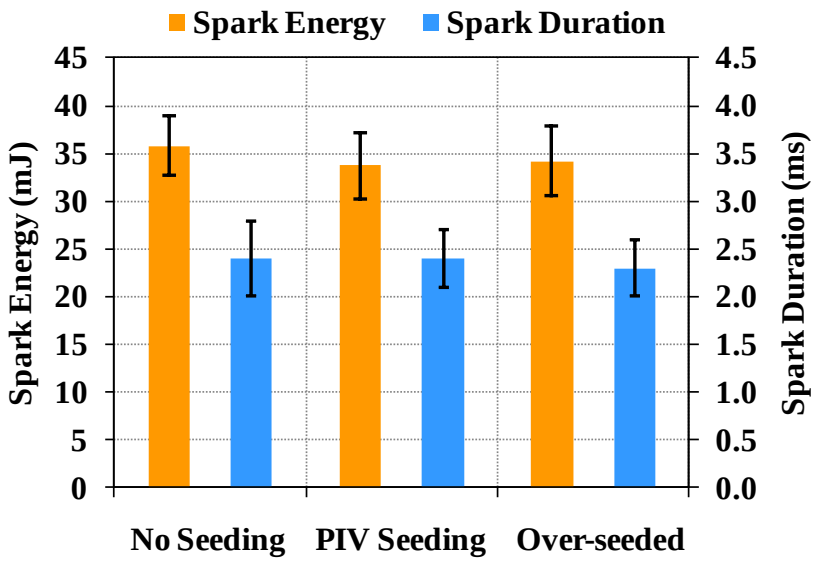

Figure 3-3: The introduction of silicone oil droplets for PIV seeding does not influence spark properties such as spark energy and duration. Bars indicate one standard deviation of the 300 spark events.

3.3.4 Controlled Experiment – Homogeneous Fuel-Air Operation

The goal of this experiment was to measure spark energy for a wide range of well-defined fuel-air equivalence ratios (Φ = 0 – 2.9). Values presented in this section are ensemble averages of 300 spark events. Bars indicated one standard deviation of the 300 measurements.

The behavior of spark energy with respect to fuel concentration is shown in Figure 3-4. A moderate trend exists between spark energy and equivalence ratio, with averaged values of spark energy showing a linear increase with equivalence ratio. Spark energy shows a 21% increase in averaged values as equivalence ratio increases from Φ = 0 – 2.3, but also exhibits an average standard deviation (1 σ) of 11%. Beyond an equivalence ratio of 2.3, spark energy begins to decrease and exhibits a smaller cycle-to-cycle variability. At these richer mixtures (Φ = 2.5 – 2.9), an appreciable amount of soot deposits existed in the cylinder, which may influence the spark behavior shown for these

mixtures. Additional studies are necessary to further examine spark behavior in the presence of soot deposits and are considered to be beyond the scope of this research.

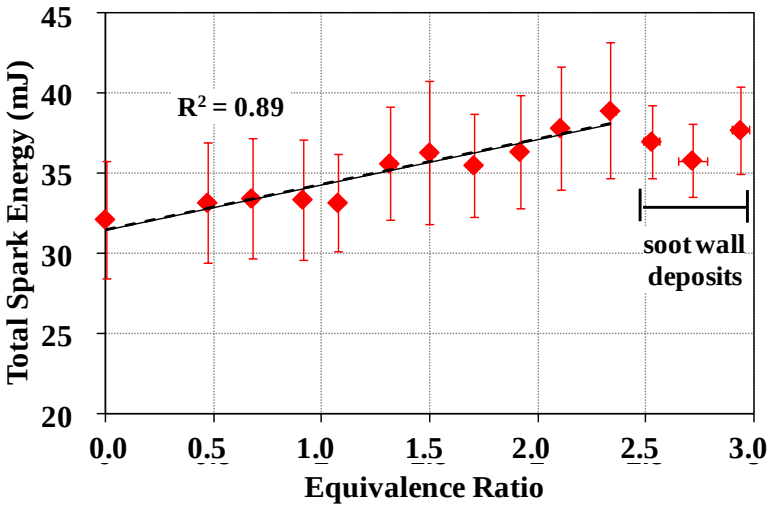

Figure 3-4: A moderate positive trend exists between spark energy and equivalence ratio. This relation ends beyond Φ = 2.3, where substantial soot was presented in the combustion chamber.

It was important to ensure that the flow field near the spark plug remained constant during these measurements. As expected, the PIV measurements showed that the different fuel injection duration during the intake stroke had no influence of the flow field near the spark plug at the time of spark. The average velocity seen during spark timing was measured as 1 – 2 m/s in the 4 mm x 4 mm region. These velocity values were consistent among all experiments. Due to the narrow range of low velocities, no correlation was found between the velocity near the spark plug and the electrical behavior of the spark discharge. This suggests that all trends shown here are strictly due to mixture composition near the spark plug and not velocity. However, the increase in the standard deviation of the spark energy at Φ = 0 compared to the baseline experiments in quiescent-ambient air is attributed to velocity fluctuations in the motored engine.

3.3.5 Controlled Experiments – Flow Field from Air Injection

The goal of these experiments was to measure spark energy released under a variety of velocities seen from an injection event. To isolate the impact of flow on spark energy, experiments were conducted in an un-fueled (air only) charge and injection velocities were produced from an air injector. Several velocity strengths were studied next to the spark plug by conducting experiments under a variety of air injection pressures (0-140 bars) with the same injection duration (1.5 ms).

It is important to note that the data with air injection and without air injection (0 bar injection pressure) were collected under the same fundamental conditions and the only difference was the flow velocity. As shown in Table 3-1, the spark event occurs after the injection event. The spark is not exposed to a direct jet of "fresh" air, but instead exposed to the residual flow field from the injection event. Mie scattering images revealed that the seeding is homogeneous during the spark event for the air injection cases and thus would have no different in mixture between air injection and non-injection cycles. Furthermore, seeding was shown to have no impact on the spark event (i.e. difference in spark energy and duration was with and without seeding was negligible). In-cylinder pressure was higher by 0.06 bar for maximum air injection (140 bar) at a peak pressure of ~ 19 bar. This different is minimal and would not drastically affect spark energy. The temperature of the injected air is estimated to be that of the cylinder head temperature (95^{o}C), while the in-cylinder temperature during injection is estimated to be 400^{o}C. Local in-cylinder temperature differences from injecting air at temperatures lower than the in-cylinder temperature can be assumed negligible as inferred from the minute

pressure difference. The only difference between the air injection and non-injection cycles is the entrained fluid velocity from the injection event. Therefore, it is argued that differences in spark energy between air injection and non-injection experiments are solely due to flow velocity.

In order to understand the different flow conditions with and without air injection, a sequence of flow field images under these conditions is shown in Figure 3-5. The sequence of flow fields for an instantaneous cycle without air injection is shown in the top half of Figure 3-5. Selected images from an air injection cycle, shown in the bottom half of Figure 3-5, highlight flow features at the highest injection pressure (140 bar) during spark timing. It should be noted that although the flow field is 3-dimensional (see Appendix B), the planar flow fields presented in Figure 3-5 accurately describe the flow fields with and without air injection. The velocity field for the non-injection cycle illustrates the flow evolution that is determined by the piston motion and residual tumble from the intake flow. The edge of a vortex borders the spark plug resulting in a moderate velocity magnitude upstream (to the left) of the spark plug (~ 2-3 m/s). The spark plug obstructs the flow beyond the spark plug leaving a wake region with a relatively stagnant flow (~ 0.5 m/s) downstream (to the right) of the spark plug. The difference in the flow field on each side of the spark plug can lead to stretching and deformation of the spark plasma. Figure 3-5 shows that the spark plasma primarily remains between the spark electrodes for cycles without air injection. At 25^{o} BTDC the spark shows a mild stretch beyond the spark electrodes.

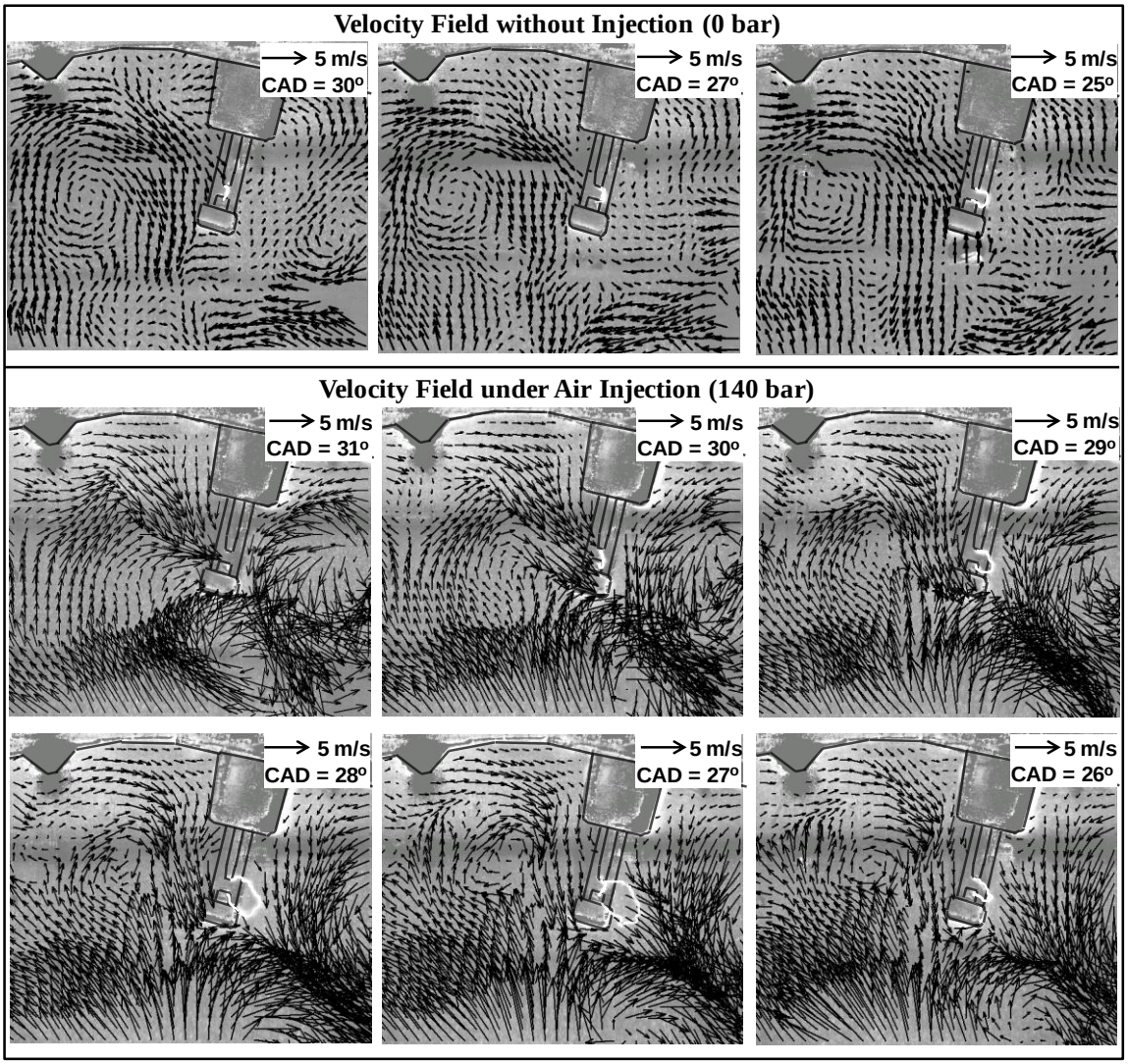

Figure 3-5: Flow fields without air injection are modest providing minimal spark stretch, whereas flow fields with air injection provide higher velocities and significant spark stretch and restrike.

The velocity field for an air injection cycle reveals much higher velocities during spark timing. The first image in this sequence shows the flow field one CAD prior to spark and at the end of the air injection (31^{o} BTDC) to illustrate the flow field during the air injection event. During the air injection, an air jet travels from the injector towards the spark plug and impacts the spark plug. Fluid in this region is dispersed and creates two re-circulating regions downstream of the spark plug. As the air jet impacts the plug, a

portion of the jet is deflected horizontally while the remaining portion of the jet passes through the spark gap and impacts the side of the piston bowl. The piston is not in the field of view for these flow images, but can be seen in Figure 3-2. The flow deflected off the spark plug interacts with nearby boundaries (top of the piston and cylinder wall) to create the circulating flow to the right of the spark plug. The flow impacting the piston bowl is reflected back towards the spark plug [55] creating the circulating region downstream the spark plug and strong flow upward at the bottom of the viewing plane. During the spark event, a strong shear flow exists downstream of the spark plug, while the flow upstream the spark plug resembles that of the expired air jet. A high vertical velocity (~ 6 m/s) at the bottom right of the images exists throughout spark timing and is primarily due to the fluid that impacts the piston bowl and is re-directed towards the cylinder head.

For air injection cycles, the high velocity near the spark plug significantly stretches and deforms the spark plasma. Referring to the images in Figure 3-5, the spark plasma in the air injection cycle shows more deformation one CAD after the onset of spark (29^o BTDC) than during the entire spark duration in the non-injection cycle. At 28^o BTDC the spark channel continues to lengthen and is shown to stretch well beyond the spark gap. The image at 27^o BTDC captures a restrike event and shows two distinct plasma channels – one channel is well beyond the spark gap, while another exists directly between the spark plug electrodes. Here, the spark discharge length reaches a limit where the plasma channel stretches well beyond the spark gap and the spark discharge cannot sustain enough new electrons and ions along the lengthening plasma channel. The elongated plasma channel ceases to exist, but a sufficient number of electrons and ions

remain available at the cathode before the available electrical energy in the secondary coil is completely dissipated [4]. At this time, a new breakdown event occurs with a new plasma channel shown directly between the electrodes. Once the new plasma channel is established, the flow is still strong enough to stretch and deform the new plasma channel before the end of the spark event.

The spark voltage and current for the non-injection and air injection cycle in Figure 3-5 are shown in Figure 3-6. The breakdown phase of the spark discharge occurs on the order of nano-seconds and is not resolved. After the peak voltage value, the voltage drops to a level on the order of 200 V, indicating the discharge has transitioned to either the arc or glow discharge phase [6]. As demonstrated by Lee et al. at the 12 bar pressure attained here, a transition from the arc to glow phase cannot always be resolved. [10].

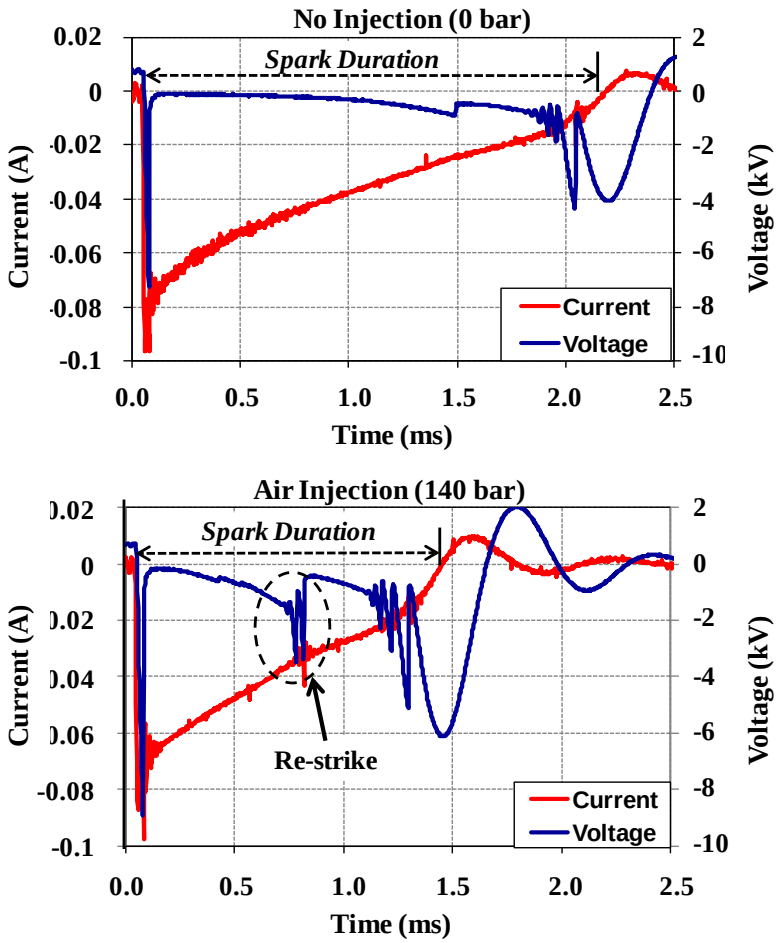

Figure 3-6: Spark voltage and current traces for the non-injection (top) and air injection (bottom) cycles shown in Figure 3-5. The higher voltage during the arc and glow phase for the air injection cycle indicates the lengthening of the plasma channel. The breakdown event associated with the restrike at 27° BTDC in Figure 3-5 is indicated by the sharp increase in voltage magnitude at 0.7 ms.

For the non-injection cycle, the glow voltage primarily remains below 1000 V and exhibits fewer changes in voltage magnitude in comparison to the air injection cycle. This is indicative of the plasma channel undergoing minimal stretch and deformation during the spark event. The spark voltage trace for the air injection cycle shows a continual voltage increase during the arc and glow phase and is associated with the lengthening of the plasma channel. The voltage increases to a value in which the available coil voltage

can no long sustain the plasma channel, resulting in the restrike shown at 27^o BTDC in Figure 3-5. This restrike is associated with a new breakdown event and is indicated by the sharp increase in voltage magnitude shown at 0.7 ms in Figure 3-6.

The flow field was analyzed in the 4 mm x 4 mm region downstream the spark plug as shown in Figure 3-2, and is presumed representative of the conditions surrounding the spark plasma especially in the region where the spark plasma extends. Spatial averages of velocity magnitude $|\overline{V}|$, shear strain rate magnitude

$$\sigma = \left(\left| \overline{\frac{1}{2}\left(\frac{\partial u}{\partial y} + \frac{\partial v}{\partial x} \right)} \right| \right) \tag{3-1}$$

and vorticity magnitude

$$\omega = \left(\left| \overline{\left(\frac{\partial u}{\partial y} - \frac{\partial v}{\partial x} \right)} \right| \right) \tag{3-2}$$

were all extracted from this region. Results presented in this section depict the ensemble-spatial average ($\left\langle \overline{\ldots} \right\rangle$) over 300 cycles. Bars shown for data at 110 bar injection pressure indicate one standard deviation of the 300 measurements to demonstrate cyclic variability.

Crank-angle resolved values of velocity, shear strain rate, and vorticity downstream the spark plug are shown for each air injection pressure in Figure 3-7. Values of velocity are shown in the top graph, while shear strain rate and vorticity values are shown in the middle and bottom graphs respectively.

Maximum velocity during spark timing occurs at the onset of spark (30^o BTDC) right after the end of injection (31^o BTDC). Velocities decay throughout the spark event and throughout the remainder of the compression stroke when velocities approach those seen under no injection. The rate of decay increases as injection pressure increases. Similar velocities are seen for injection pressures of 140, 110, and 80 bar despite differences in injection pressure. A likely explanation can be that the air jet impacts the spark plug and velocities are significantly altered, possibly limiting the air velocity downstream the spark plug.

Maximum shear strain rate occurs during the injection event and the highest values during spark occur at the onset of spark. Peak shear strain rates increase monotonically with injection pressure and are significantly greater than shear strain rates for non-injection operation. Values of shear strain rate from the injection event continue to decay throughout the remainder of the compression stroke and approach values seen for no injection.

In contrast to velocity magnitude and shear strain rate, vorticity does not vary monotonically with injection pressure in the investigated area. Furthermore, at the onset of spark, the vorticity is higher for lower injection pressures and decreases as injection pressure increases. This trends along with those seen for shear strain rate and velocity indicates that the flow after the injection event is stronger with greater fluid deformation at the higher injection pressures, but shows greater fluid rotation at the measurement location for lower injection pressures. The vorticity is largest during air injection and rapidly decreases at the conclusion of the injection event.

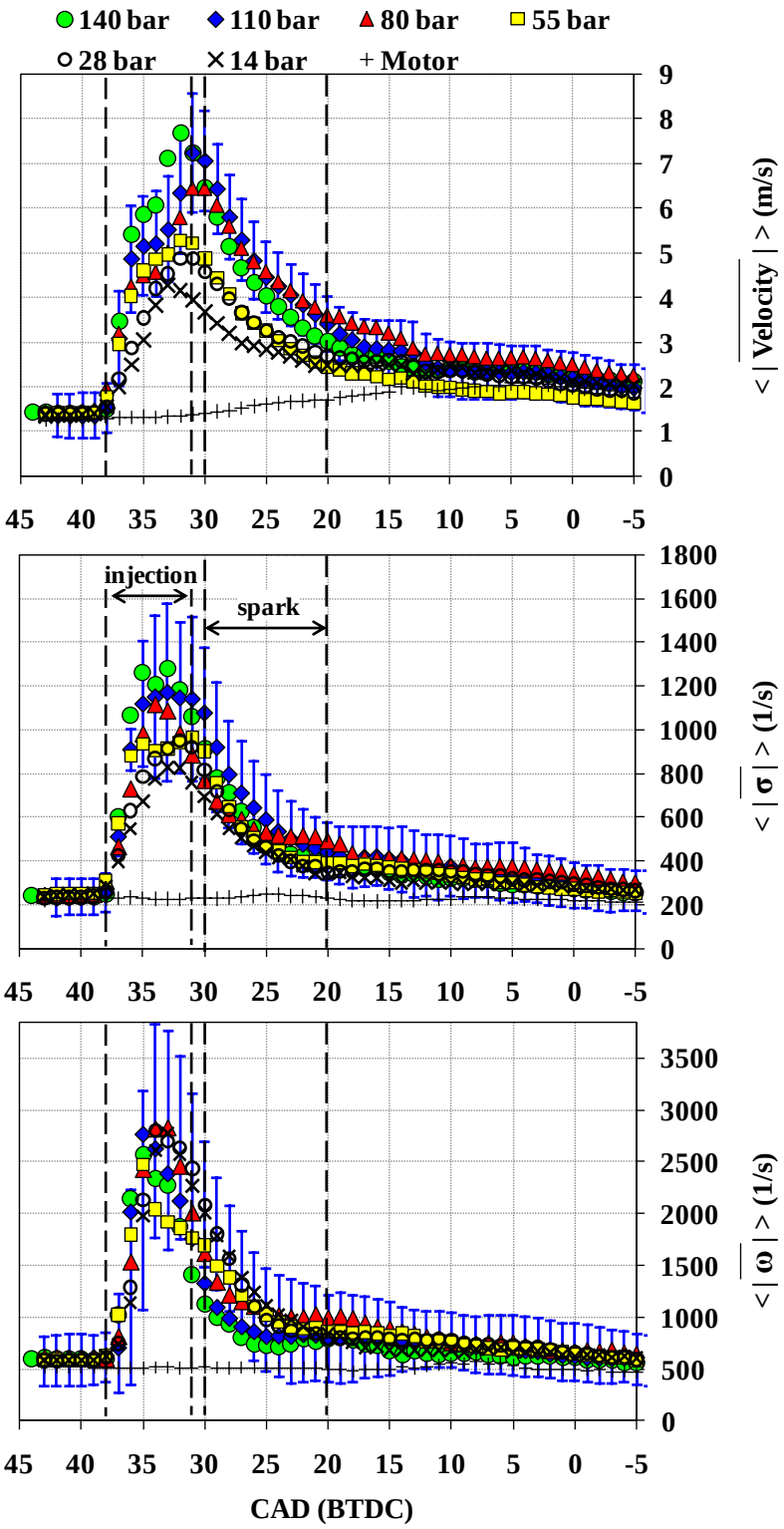

Figure 3-7: Ensemble-spatial average of velocity magnitude (top), shear strain rate (middle), and vorticity (bottom) during the air injection and spark event for all air injection pressures. Bars indicate one standard deviation of the 300 measurements at 110 bar to demonstrate the cycle-to-cycle variability.

At the time of spark, averaged values of velocity magnitude (8 m/s), shear strain rate (1000 1/s), and vorticity (1200 1/s) under the highest air injection pressures (140 and 110 bar) are similar to averaged values seen under stratified operation in a SG-SIDI engine and reported by Peterson and Sick [55]. Thus, similar flow conditions have been achieved with the air injection but any complication due to multi-phase flow or high stratification have been avoided for the analysis of spark behavior as a function of flow field properties.

Relationships between flow properties and spark energy released to the fuel-air mixture are of high interest for ignition studies and for building predictive models for IC engine simulations. Therefore, spark energy was correlated with velocity magnitude, shear strain rate, and vorticity measured in the 4 mm x 4 mm region downstream the spark plug. Integrated quantities for the duration of the spark discharge as well as values at the onset of spark were examined. The onset of spark was chosen to correlate time-specific quantities to compare results to cases of combustion in which flow field quantities beyond the spark are biased due to disappearing PIV seeding and combustion luminosity in the 4 mm x 4 mm region.

This discussion presents both cycle-resolved quantities of the entire data set for all air injection pressures and ensemble averages computed for the 300 cycles recorded for each injection pressure. Averaged flow field quantities throughout the entire spark event are the ensemble-temporal-spatial average represented as $\{\overline{\langle ... \rangle}\}$, while quantities at the onset of spark are ensemble-spatial averages represented as $\overline{\langle ... \rangle}$.

The influence of velocity magnitude on spark energy is displayed in Figure 3-8. The cycle-resolved velocity data exhibits large scatter but a positive correlation exists for

a linear relationship between total spark energy and averaged velocity seen during the spark event. This is more evident when the data are ensemble-averaged for each injection pressure. As velocity near the spark plug increases, the energy delivered to the spark plasma increases. This is primarily due to the stretching of the spark plasma (see Figure 3-5) that increases the voltage between the electrodes [5, 11, and 18]. In addition, with higher velocities near the spark plug, restrikes are more common which further increase the spark energy due to additional breakdown events. A linear relationship is also found for ensemble-averaged quantities at the onset of spark, but shows a weaker correlation. The large scatter in the data and thus weaker correlations are most likely attributed to the inability to measure quantities along the plasma channel. At the time of spark, the plasma channel has not had sufficient time to stretch into the 4 mm x 4 mm region. Instead the plasma channel is primarily located between the spark electrodes and quantities do not depict the values seen along the spark plasma. Time-specific data during the 2^{nd} and 3^{rd} CAD after the onset of spark have higher correlation coefficients (see Appendix C), most likely because the spark plasma is within the 4 mm x 4 mm region at this time. However, as stated above, quantities at the onset of spark are emphasized to be compatible with measurement restriction under fired conditions presented in chapter 5. In inability to measure quantities along the spark channel during each CAD is a weakness of the measurement technique, but is still able to provide relevant information to describe spark behavior.

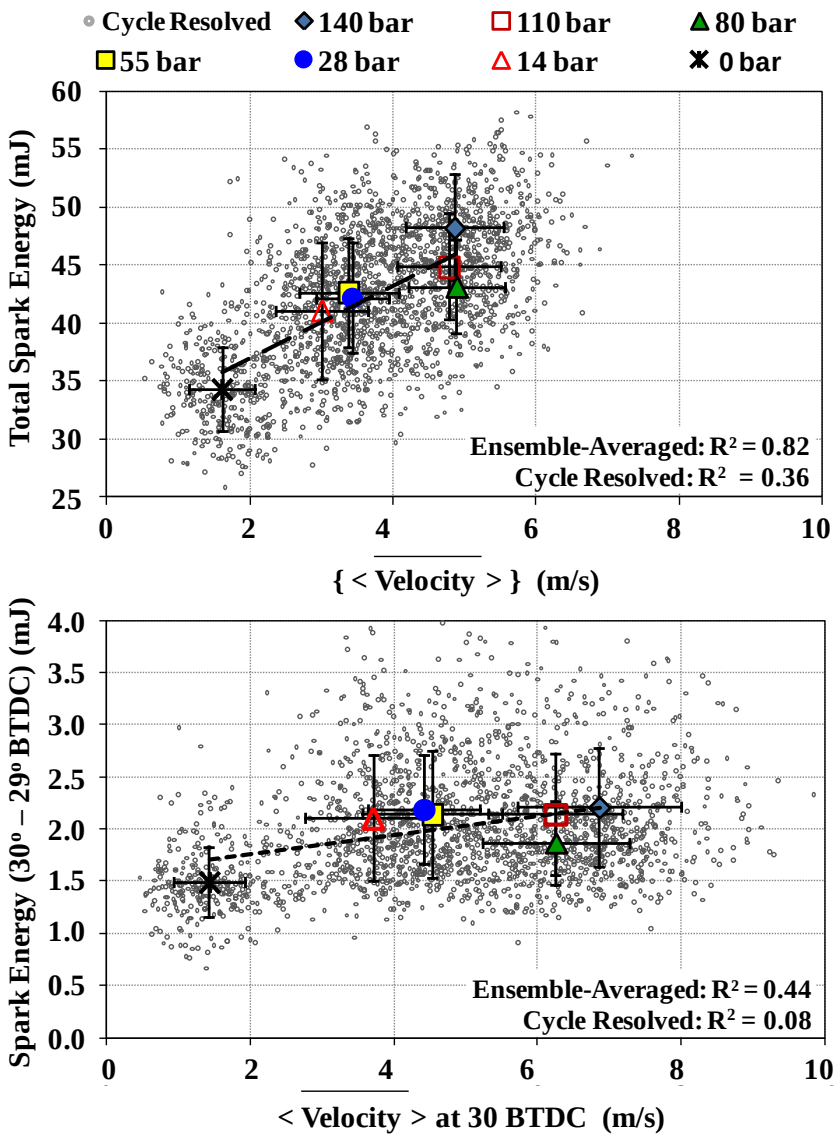

Figure 3-8: A linear relationship exists between spark energy and velocity during the entire spark duration (top) and at the onset of spark (bottom). The spread in the cycle-resolved data yields weaker correlations. Spark energy at the first spark CAD excludes the breakdown. Bars indicated one standard deviation of the 300 measurements. Cycle-resolved data are presented for all injection pressures.

Cycle-resolved velocity data (for all injection pressures) overlaid with specific ensemble-averaged data show the cycle-to-cycle variability in the data and shows lower a correlation. With all observed events being highly stochastic, the large cyclic variability is not too surprising. The lower correlation for the cycle-resolved data can also arguably

reflect that the recorded velocities are not directly measured along the plasma channel. On average the spark plasma lies in the 4 mm x 4 mm region, but velocities vary across this region and the plasma channel can move out of plane since the light sheets are only 1 mm thick. With integral scales found to range from 1 – 10 mm in this engine [46], it is not surprising to see weak correlations if the plasma channel moves slightly in or out of the viewing plane. In addition, the fact that the flow field is 3-dimensional (see Appendix B) can inhibit the ability to correlate planar velocity measurements with the spark energy. Nonetheless, the expected linear relationship between spark energy and velocity [4, 5, 7, 8, and 22] is observed, albeit with low correlation coefficients even close to zero for measurements during the first spark CAD.

Total spark energy is also well-correlated with ensemble-averaged shear strain rate for each injection pressure as shown in Figure 3-9. Spark energy released between the electrodes increases linearly with increasing strain rates. It is likely that the fluid deformation within the region downstream the spark plug is similar to deformation of the actual plasma channel. This is consistent with the view that the spark plasma is transported passively by the local fluid motion described by Maly et al. [11]. Spark energy increases with plasma deformation and is consequently strongly correlated with the nearby fluid deformation. The temporal-spatial averaged shear strain rate and the strain rate at 30^{o} BTDC both correlate well with total spark energy and spark energy seen throughout the first spark CAD. Similar to cycle-resolved velocity measurements, cycle-resolved data between spark energy and shear strain rate exhibit a lower correlation compared to ensemble-averaged quantities. Large cycle-to-cycle variations and the

inability to measure along the plasma channel (i.e. plasma channel not in extraction region) are the primary factors leading to the lower correlations.

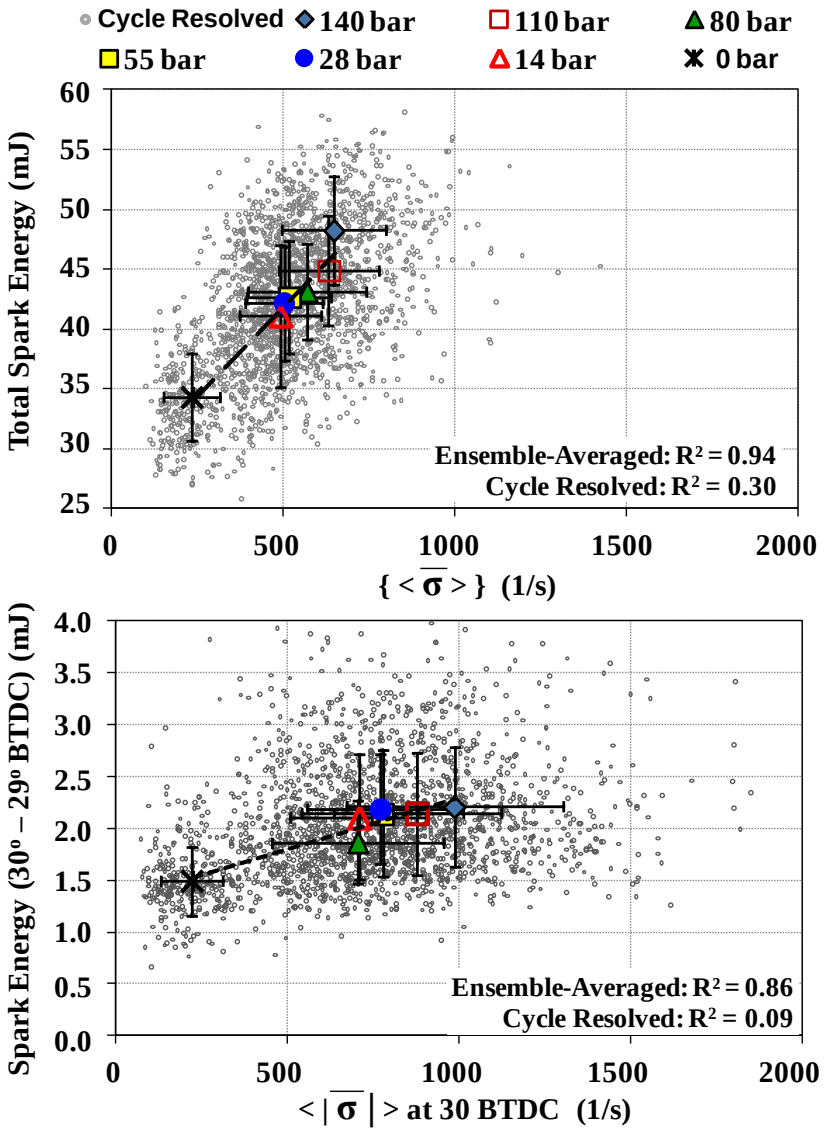

Figure 3-9: A linear relationship exists between spark energy and shear strain rate during the entire spark duration (top) and at the onset of spark (bottom). Cycle-resolved data have a large spread yielding lower correlations. Spark energy at the first CAD excludes the breakdown. Bars indicate one standard deviation of the 300 measurements. Cycle-resolved data are presented for all injection pressures.

The impact of vorticity near the spark plug on spark energy released is shown in Figure 3-10. The total spark energy does not show an apparent, simple relationship with

averaged vorticity in contrast to averaged velocity and shear strain rate. From the cycle-resolved data it is indicated that increasing vorticity does lead to an increase in spark energy but the spread in the data is very large and hence the correlation is weak. The analysis of the impact of vorticity on spark plasma stretching and in turn spark energy will require further assessment and experiments which are beyond the scope of this work.

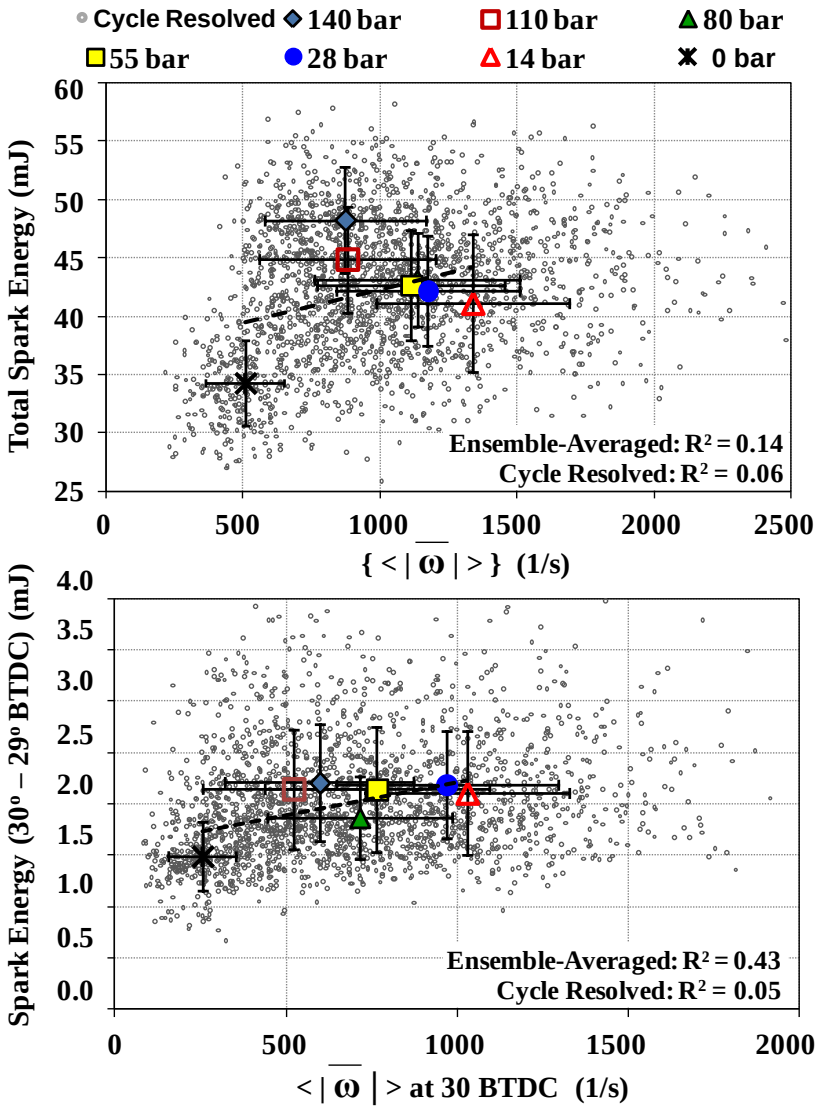

Figure 3-10: A linear relationship does not exist between total spark energy and averaged vorticity during the spark event (top). A weak positive linear relationship is shown between spark energy and vorticity at the onset of spark (bottom). Spark energy at the first spark CAD excludes the breakdown. Bars indicated one standard deviation of the 300 measurements. Cycle-resolved data are presented for all injection pressures.

3.4 Discussion

The data presented in this chapter characterizes spark energy dependence for a wide range of operating conditions. It is suggested that modeling approaches for spark ignition in environments such as stratified operation must include spatial and temporal resolved information of fuel concentration and flow properties since both have an impact on the amount of available spark energy. Relationships obtained between spark energy and flow properties should be interpreted as trends only, given that measurements were obtained in manner such that only in a statistical sense the plasma channel was contained in the measurement volume. Other factors specific to the ignition system (i.e. spark gap spacing, electrode material, etc.) should also be considered when interpreting relationships presented in this chapter.

Weaker correlations are shown for cycle-resolved measurements than ensemble-averaged measurements for each injection pressure. As previously stated, a possible explanation of this is the fact that the flow field properties are not measured directly along the plasma channel. On average, the plasma channel is contained within the 4 mm x 4 mm region, but velocities vary across this region and the plasma channel can move out of plane. From the presented measurement technique it would also appear that the data is better correlated when conditionally sampling on the injection pressure rather than conditionally sampling on the specific flow field data. The injection pressure would more or less indicate the momentum of the air jet rather than the resulting velocity or shear strain rate.

The data presented in this chapter is intended to provide additional information of spark energy release under stratified operation in the SG-SIDI engine. In general, trends shown in this chapter are capable of describing how available spark energy will respond

as engine parameters such as spark timing change to produce different fuel-air mixtures and flow fields near the spark plug at the time of spark. This is capable of providing further insight to what might attribute to ignition stability or instability.

For rare ignition instability events (i.e. misfires) it is necessary to look at spark energy, fuel concentration and flow field information on a cycle-resolved basis. As presented in this chapter, lower correlations exist for cycle-resolved data primarily due to the large scatter in the data and the inability to measure directly along the spark channel. Therefore, it is not unexpected to experience weak trends among cycle-resolved data under fired operation. However, it is anticipated that analysis presented in this chapter can further couple fuel concentration and flow field properties to spark energy to explain rare ignition instability events such as misfire.

3.5 Conclusions

Experiments were conducted to characterize the spark energy dependence on equivalence ratio, flow velocity, shear strain rate, and vorticity near the spark plasma. Spark energy was obtained for a wide range of homogeneous equivalence ratios ($\Phi = 0 – 2.9$) under identical flow conditions ($V = 1 – 2$ m/s). In addition, spark energy was measured for a wide range of flow fields at the spark gap (1 – 10 m/s) in an un-fueled, air injected charge to eliminate the influence of equivalence ratio.

A moderate dependence of spark energy on equivalence ratio was found with average values of spark energy increasing by 21% for the equivalence ratio range from $\Phi = 0 – 2.3$. The impact of velocity, shear strain rate, and vorticity on spark energy released is much stronger under the applicable range of flow fields in a SG-SIDI engine. Values of spark energy were shown to increase up 40% over the investigated range of flow fields.

Measured flow data and spark energy were correlated for ensemble-averaged data at each air injection pressure and for cycle-resolved data for the entire data set from all air injection pressures. These correlations were presented for averaged flow field values throughout the spark event and total spark energy as well as crank-angle specific values at the onset of spark. Data interpreted for flow field properties should be interpreted as trends only since the flow measurements were performed such that only in a statistical sense was the plasma contained in the measurement region. Spark energy was shown to increase linearly with increasing velocity and shear strain rate. This is consistent with previous findings in ambient conditions for velocity [5 and 11]. A linear increase of spark energy with increasing vorticity observed with very low correlation and further studies are suggested for confirmation. Overall weak correlations existed for cycle-resolved data primarily due to the large scatter in the data and the inability to measure directly along the plasma channel. Trends between ensemble-averaged quantities ultimately remove some of the scatter, resulting in higher correlation coefficients.

It is anticipated that analysis presented in this chapter can further couple fuel concentration and flow field properties to spark energy to help explain rare ignition instability events such as misfire.

CHAPTER 4

ENGINE OPERATION WITH RARE IGNITION INSTABILITIES

4.1 Introduction

It is desired to study the occurrence of *rare* misfire events under stratified charge, low-load idle operation in a SG-SIDI engine. To achieve this, engine operating parameters need to be selected to provide stable engine performance, yet have the occurrence of rare ignition instabilities.

This chapter presents the procedure used to identify near optimum engine performance with the occurrence or rare misfires and partial burns at idle conditions. In particular, spark timing was the key variable that was adjusted to obtain near optimum engine operation with rare occurrences of ignition instability. In addition, the introduction of nitrogen (N_2) is used to simulate exhaust-gas-recirculation (EGR) and provides additional ignition instability events for the given operating conditions. PIV, PLIF, and spark measurements are obtained at the near optimum and optimum engine operation to demonstrate the different in-cylinder conditions that exist near the spark plug for these operating conditions at selected spark timings and dilution levels.

4.2 Inducement of Ignition Failures

4.2.1 Selection of Spark Timing

Engine operating parameters, shown in Table 4-2, were chosen to mimic low-load idle conditions in a SG-SIDI engine at 800 RPM. The fueling rate (7.5 mg / cycle) was selected to provide idle-like engine loads. External dilution (N_2 to simulate EGR) was not introduced for the initial mapping of the engine performance. The injection timing was held fixed with end-of-injection at 32^o BTDC to provide a suitable 50% mass fraction burned (MFB) at a location 5^o – 10^o ATDC to optimize engine output. To identify optimum engine operating conditions, spark timing was varied to maximize the indicated mean effective pressure (IMEP) and minimize the coefficient of variance (COV) of IMEP. Figure 4-1 shows averaged IMEP and COV of IMEP values for 375 engine cycles at various spark timings (33^o – 28^o BTDC).

Engine Operating Parameters for Engine Mapping	
Engine Speed	800 RPM
Intake manifold pressure	95 kPa (absolute)
Intake air temp.	45^oC
Coolant temp	90^oC
End-of-injection (physical)	32^o BTDC
Injection pressure	110 bar
Fuel	90% isooctane, 10% biacetyl
Fuel per cycle	7.5 mg
Spark timing	Variable
Spark dwell	3.5 ms
External Dilution level (%)	Variable

Table 4-2: Engine operating parameters used for characterization of engine performance at low-load idle conditions.

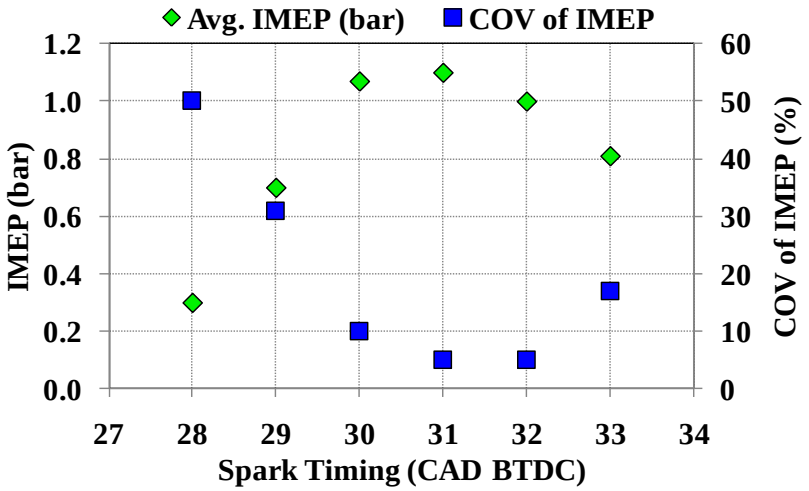

Figure 4-1: With an EOI of 32° BTDC, optimum engine performance occurred with a spark timing of 31° BTDC where IMEP was maximized and COV of IMEP was minimized.

Optimum engine performance occurs for a very narrow spark timing window (32° – 31°). The best engine performance occurs with a spark timing of 31° BTDC where IMEP is maximized (1.13 bar) and COV of IMEP is minimized (4%). At a spark timing of 31° and 32° BTDC no misfires or partial burns were observed. Here misfire is defined as cycles with IMEP < 0 bar, while partial burns are defined as cycles with MFB < 0.6. As spark timing is advanced to 33° BTDC, multiple misfires and partial burns occur (indicated by lower average IMEP and higher COV of IMEP), demonstrating the difficulty of igniting a mixture during the injection event. Operation with a spark timing of 30° BTDC yielded an IMEP = 1.09 bar and COV of IMEP = 10%, which included the occurrence of misfires and partial burns (< 1% occurrence).

Figure 4-2 compares the engine performance between the optimum spark timing (31° BTDC) and the spark timing of 30° BTDC. IMEP values are shown for 375 cycles at the two spark timings. IMEP values for a spark timing of 30° yielded similar IMEP values as those at a spark timing of 31° BTDC; at 30° BTDC the average IMEP was calculated to be 1.13 bar with a COV of IMPE of 5% when excluding the partial burn and

misfire. Figure 4-2 also demonstrates the rare occurrence of ignition instability events; out of the 375 cycles 1 misfire and 1 partial burn occurred. Thus, the spark timing of 30° BTDC with an EOI of 32° BTDC (and no external dilution) provided an opportunity to study the rare occurrence of misfires and partial burns at an otherwise robust operating condition. Increasing the rate of misfires and partial burns (via adjusting spark timing) was not attempted so that all errant cycles were always preceded by a well-burned cycle with an IMEP within one standard deviation of the mean.

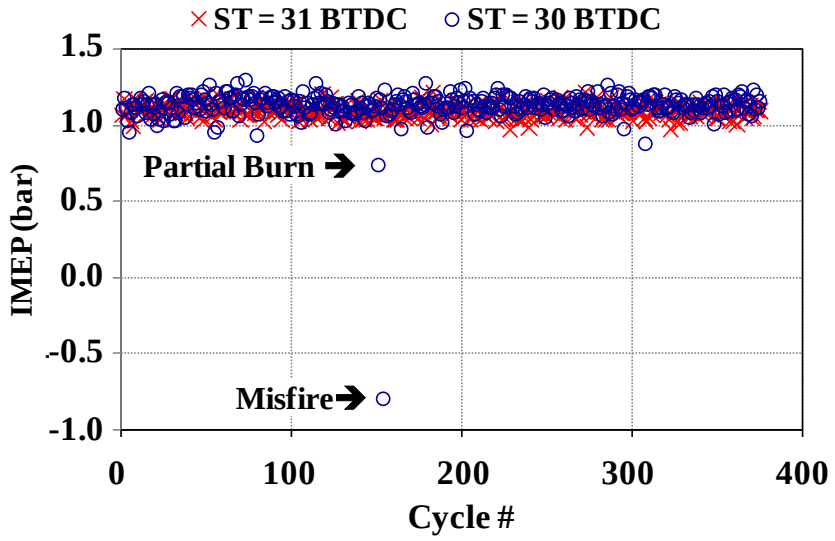

Figure 4-2: Individual cycle IMEP values are similar for spark timing of 31° BTDC and 30° BTDC, with the exception of rare misfire and partial burn cycles at a spark timing of 30° BTDC.

4.2.2 Dilution Level

In typical engine operation, external exhaust gas recirculation (EGR) is often introduced into the intake air as a charge diluent to moderate peak temperatures inside the cylinder to reduce the production of NO_X [1]. Consequently, the presence of EGR in the cylinder also slows flame propagation and can destabilize combustion. In the extreme case, ignition instabilities can occur especially in stratified mixtures. Therefore, it is

desired to characterize engine performance under a range of applicable dilution levels at the selected spark timings of 30^{o} and 31^{o} BTDC. In particular it is desired to obtain near optimum operating conditions for a given range of dilution levels in which rare ignition instabilities occur.

Exhaust gas is a highly complex, multi-component mixture that can be difficult to reproduce repeatedly. Fortunately, in a previous investigation by Quader [56], it was revealed that the main feature of the diluent that affects combustion performance is the heat capacity and not the specific mixture composition. For this reason, bottled nitrogen was used to simulate EGR dilution due to its similarity in heat capacity. The diluent nitrogen was metered through a critical orifice system and introduced into the intake air. Intake manifold pressure was maintained at 95 kPa and therefore the oxygen in the intake air was displaced with the added nitrogen.

IMEP values are shown in Figure 4-3 to characterize engine performance for a range of dilution levels (0%, 10%, 18%, 26% by volume) with the selected spark timings of 30^{o} and 31^{o} BTDC. A total of 375 cycles were recorded at each operating condition. As previously shown, rare misfires and partial burns occur for a non-diluted (0% dilution) mixture with a spark timing of 30^{o} BTDC. As dilution level increases to 10% with the 30^{o} spark timing, the occurrence of misfires and partial burns increase and is indicated by the increasing number of cycles with IMEP values below 0.7 bar. While more ignition instabilities occur at this operating condition, their occurrence is still shown to be rare with roughly a 2% occurrence rate. The dilution level of 18% and spark timing of 30^{o} BTDC produces multiple ignition instabilities that significantly alter the engine performance. A dilution level of 26% with a spark timing of 30^{o} BTDC is not reported

because these conditions did not produce a stable engine operating condition due to common occurrence of misfire, partial burn, and overall high cycle-to-cycle variability (i.e. COV of IMEP ~ 60%). At a spark timing of 31^{o} BTDC no misfires or partial burns occur for the dilution levels of 0% and 10% and the engine performance is stable. When dilution level increases to 18%, rare ignition instability events occur for the spark timing of 31^{o} BTDC. As the dilution level increases to 26%, multiple misfires and partial burns occur and significantly alter the engine performance.

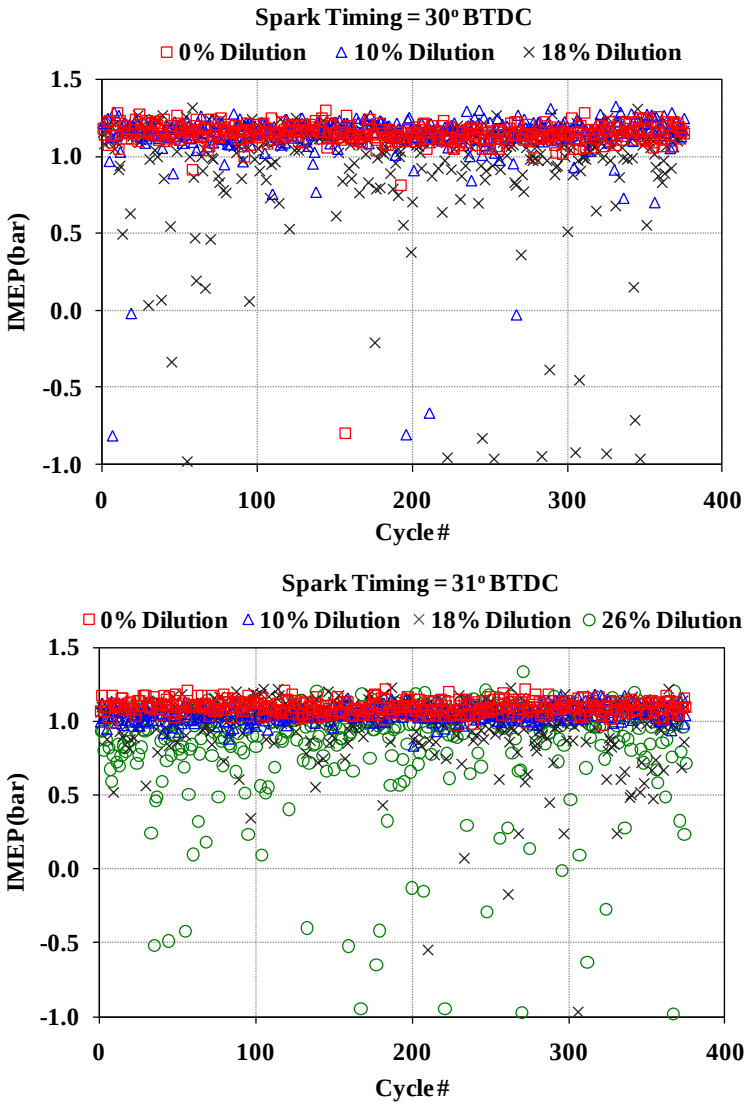

Figure 4-3: Individual cycle IMEP values are used to characterize the engine performance for a range of dilution levels (0%, 10%, 18%, 26%) for the selected spark timings (30° and 31° BTDC). A total of 375 cycles are obtained for each operating condition. Stable engine performance with the exception of rare ignition instabilities is found for dilution levels of 0% and 10% with a spark timing of 30° BTDC and for a dilution level of 18% with a spark timing of 31° BTDC.

Overall, the dilution levels of 0% and 10% provide a stable engine operating condition with the rare occurrence of ignition instabilities for a spark timing of 30° BTDC. Similarly, with the optimum spark timing of 31° BTDC, rare ignition instabilities occur for the dilution level of 18%. At the higher dilution levels of 18%, the spark timing of 30° BTDC is advanced to 31° BTDC to provide stable engine performance, with the

exception of rare ignition instabilities. As dilution level increases to 26%, engine performance even at the optimum spark timing (31^{o} BTDC) is non-optimal and indicates the upper limit of dilution level for stable engine operation.

4.3 Simultaneous Flow Field and Fuel Concentration Images

Simultaneous flow field and fuel concentration measurements were obtained at crank-angle resolution in the SG-SIDI engine under stratified fuel operation. Fuel concentration measurements were confined to an 18 mm x 28 mm region left of the spark plug, while velocity measurements expanded a slightly large region of 35mm x 28 mm as illustrated in Figure 4-4. The different dimensions of the two measurement planes are due to the differences in the laser beam diameters (UV laser beam ~ 5 mm diameter, green laser beams ~ 15 mm diameter). The two green laser pulses were separated by a time delay of 20 μs to resolve the high velocity magnitude after the spray event and provided a pixel shift that was within ¼ of the final interrogation window size (32 pixels x 32 pixels) [54].

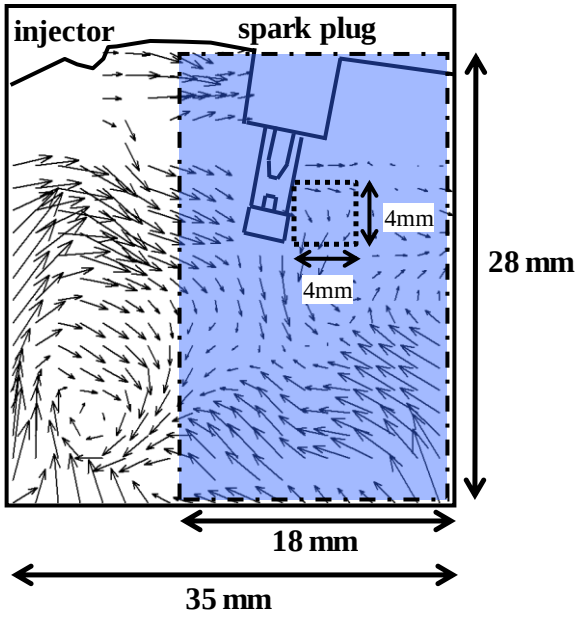

Figure 4-4: Fuel concentration measurements were confined to an 18 mm x 28 mm region (darkened region), while velocity measurements were obtained in a 35 mm x 28 mm viewing plane.

Images of flow field and fuel concentration are shown for an instantaneous motored cycle (no spark) with late fuel injection in Figure 4-5 (a)-(i). Images are acquired for each CAD, but images shown in Figure 4-5 are selected to demonstrate the in-cylinder conditions before, during, and after the injection event. Images during and after the spray event (33^{o} – 26^{o} BTDC) are shown at crank-angle resolution to reveal the in-cylinder conditions that exist when spark timing would occur. The gray color-scale for equivalence ratio is incorporated with a color-scale (blue and green) to highlight the regions of lean mixtures within the flammability limits ($\Phi = 0.6 – 0.9$, shown in blue) and regions of stoichiometric mixtures ($\Phi = 0.9 – 1.1$, shown in green). The analysis in this section is *strictly* presented to provide the reader with a general understanding of the injection event and post-injection event for the given single-cylinder SG-SIDI optical engine.

An image at the onset of injection (37^o BTDC) is shown in Figure 4-5 (a) to reveal the in-cylinder conditions before the injection event. The image during spray (33^o BTDC) is shown in Figure 4-5 (b) and reveals the highly turbulent flow conditions that exist from the spray event. It is shown that the spray plume impacts the spark plug and primarily penetrates through the spark gap, creating high velocities downstream the spark plug. Strong velocities exist after the injection event and decrease in magnitude as time elapses from the end-of-injection. In a similar manner, rich fuel-air mixtures exist near the spark plug after the end-of-injection and quickly lean out with time. Specifically, a rich fuel cloud ($\overline{\Phi} \sim 1.7$) exists downstream the spark plug at 31^o BTDC and leans out near stoichiometric ($\overline{\Phi} = 0.9$) a crank-angle later (30^o BTDC). Beyond this timing, the fuel distribution directly downstream the spark plug is fuel-lean and becomes leaner quickly with time. The fuel distribution shown for this cycle demonstrates the short time interval in which a flammable mixture exists near the spark plug after the spray event. This adequately reveals that the CAD range of $32^o - 30^o$ is clearly the optimum timing for the onset of spark as described earlier in Figure 4-1. Beyond this timing, fuel mixtures are likely to be too lean to sufficiently form a flame kernel that is capable of remaining in contact with the flammable mixture that quickly moves away from the spark plug.

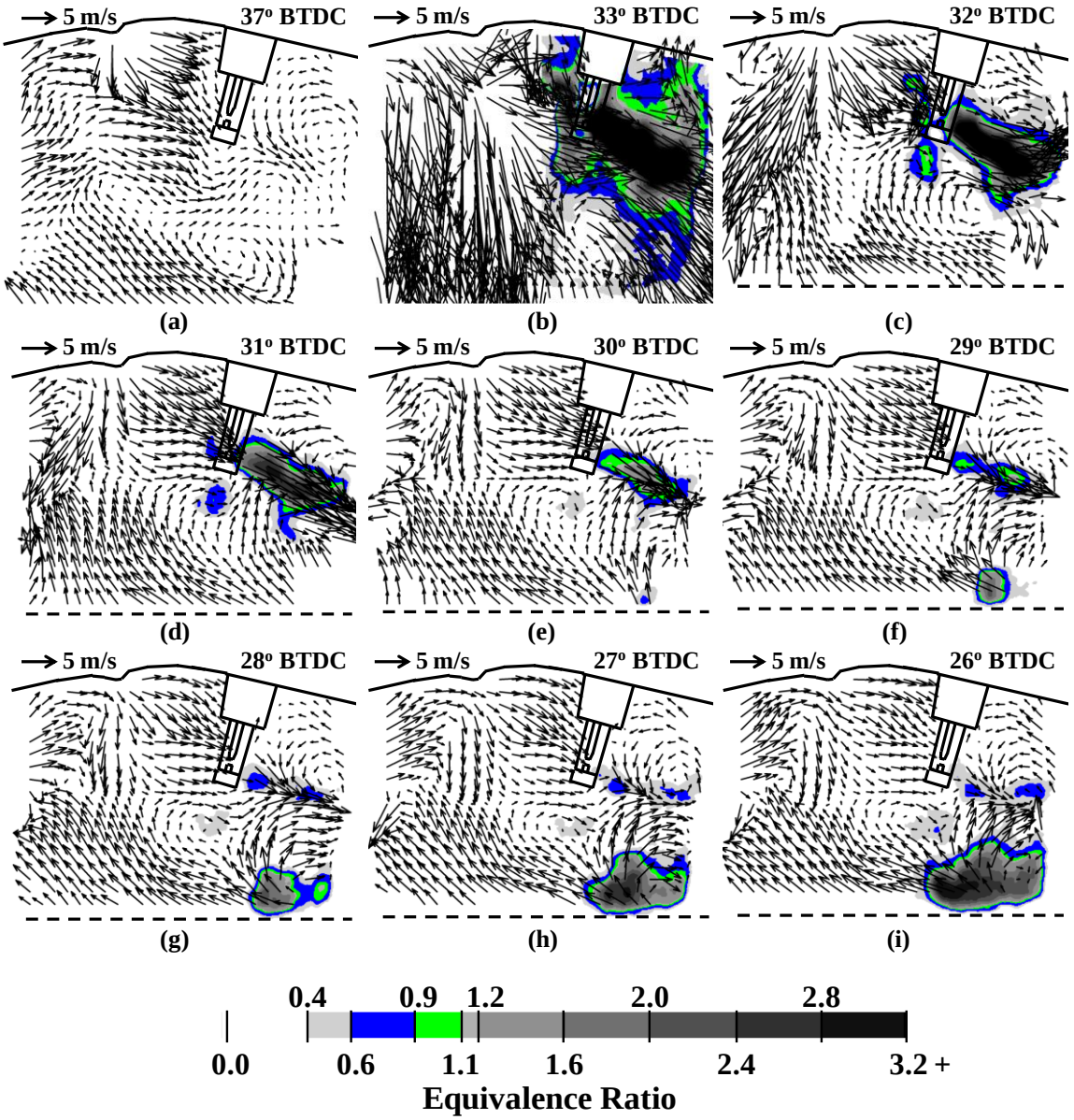

Figure 4-5: Simultaneous fuel concentration and flow field measurements for a single motored-spray cycle illustrate the conditions that exist near the spark plug during the typical spark timing. Images reveal the highly turbulent conditions that exist during the injection even and shortly afterwards as well as the short time interval after the injection event in which an ignitable mixture is located near the spark plug (32^{o} – 30^{o} BTDC).

The images of the post-injection event adequately describe the flow motion and fuel distribution in the rest of the combustion chamber. After the injection event, the momentum of the fuel-air mixture continues diagonally downward into the piston bowl and impacts the bottom corner of the piston bowl (Figure 4-5 (f)). The fluid then

rebounds off the piston bowl surface and a rich fuel-air mixture is collected in the piston bowl and moves upward with the bottom of the piston bowl (Figure 4-5 (f) – (i)), which is shown by the dotted line. Velocities surrounding the fuel-air mixture adequately describe the motion of the fuel-air mixture downstream the spark plug and within the piston bowl. Well after the injection event it is also shown that the flow field portrays a similar less turbulent 2-D flow pattern as shown prior to the injection event.

4.4 Flow Field and Equivalence Ratio Measurements for Fired Operation at Selected Spark Timings

High-speed PIV and PLIF are used to measure flow velocity and fuel distribution for fire operation for cycles with selected spark timings of 31^o and 30^o BTDC. Spatial averages of equivalence ratio ($\overline{\Phi}$), velocity magnitude $|\overline{V}|$, shear strain rate magnitude $|\overline{\sigma}|$, and vorticity magnitude $|\overline{\omega}|$ were extracted from the 4 mm x 4 mm region downstream the spark plug shown in Figure 4-4. These values were used to compare the in-cylinder conditions near the spark plug for the different spark timings during fired operation.

Figure 4-6 shows plots of equivalence ratio vs. velocity magnitude (top) and vorticity vs. shear strain rate (bottom) at the onset of spark for the different spark timings. A total of 1044 cycles are shown for each spark timing. No external dilution was used for the 2088 cycles in this analysis. The ensemble-spatial averaged values of equivalence ratio, velocity, shear strain rate, and vorticity are displayed in Table 4-3 for the different spark timings. The variation associated with these values is one standard deviation over the 1044 measurements associated with each spark timing.

At a spark timing of 31^{o} BTDC, stronger velocities and richer mixtures exist near the spark plug due to the shorter time separation between EOI and spark timing. The velocity range shown in Figure 4-6 is larger for a spark timing of 31^{o} BTDC than for a spark timing 30^{o} BTDC. This is likely due to the stochastic nature of the flow caused by the injection event. The injection event creates a highly turbulent 3-dimensional flow field (see Appendix B) and produces large cycle-to-cycle variations in the in-cylinder flow. This cycle-to-cycle variation is still large one CAD after the end-of-injection (31^{o} BTDC) and begins to decrease as time progress after the injection event. Also illustrated in Figure 4-5, richer mixtures are present near the spark plug at 31^{o} BTDC than at 30^{o} BTDC because the momentum from the fuel plume past the spark plug quickly disperses the fuel-air mixtures further downstream the spark plug and into the piston bowl.

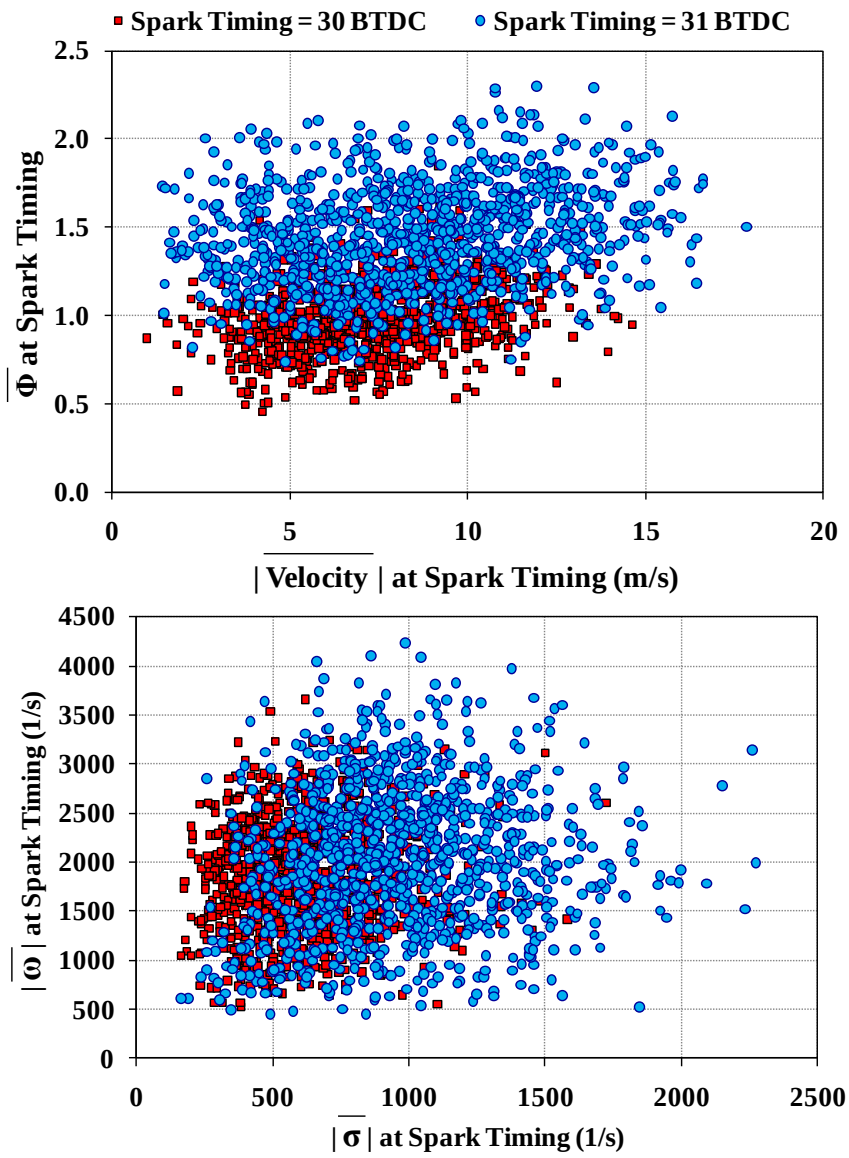

Figure 4-6: Equivalence ratio, velocity, and shear strain are greater near the spark plug at the spark timing of 31° than the spark timing of 30° due to the shorter time interval between the end-of-injection and the onset of spark.

Parameter	Spark Timing = 31° BTDC	Spark Timing = 30° BTDC
Velocity Magnitude (m/s)	8.6 ± 3.4	7.4 ± 2.3
Equivalence Ratio	1.5 ± 0.3	1.0 ± 0.20
| Shear Strain Rate | (1/s)	980 ± 350	610 ± 230
| Vorticity | (1/s)	2000 ± 730	1800 ± 550
Spark Energy for 1st Spark CAD (exclude breakdown) (mJ)	5.0 ± 1.1	3.2 ± 0.6

Table 4-3: Ensemble-spatial average values for velocity magnitude, equivalence ratio, and spark energy during the first spark CAD for the spark timings of 31° BTDC and 30° BTDC.

The stochastic nature of the flow field from the injection event can also be displayed in the large cycle-to-cycle variation shown in the vorticity vs. shear strain rate plot for a spark timing of 31^{o} BTDC shown in the bottom graph of Figure 4-6. Shear strain rate is shown to be higher for the earlier spark timing with a slightly larger spread in the values. Vorticity, on the other hand, is shown have similar values and cycle-to-cycle variability for the different spark timings.

The differences with the flow field and fuel distribution near the spark plug affect the amount of spark energy released for engine operation at the different spark timings. Table 4-3 also includes the ensemble-averaged values of spark energy released for the first spark CAD for each spark timing (i.e. first spark CAD for ST = 31: 31^{o}-30^{o} BTDC, first spark CAD for ST = 30: 30^{o}-29^{o} BTDC). For further analysis, spark energy released during the first CAD is plotted against velocity magnitude and equivalence ratio and is shown in Figure 4-7. The spark energies reported for the first spark CAD exclude the breakdown event since the breakdown event cannot be resolved. Comparison of the data points for the different spark timings shows an evident impact on spark energy released due to the different velocity magnitudes and equivalence ratios nearby the spark plug at the onset of spark. Spark energy during the first spark CAD is on-average greater for the earlier spark timing of 31^{o} BTDC, where higher velocities and richer mixtures exist near the spark plug. The top graph in Figure 4-7 reveals greater spark energies at a spark timing of 31^{o} BTDC, despite the large spread in velocity data. The cycle-resolved data do not reveal a strong trend between spark energy and velocity for the measured values, which is consistent with cycle-resolved data for air injection velocities presented in section 3.3.5. The maximum values of velocity magnitude presented here for fuel

injection ($|\overline{V}|$ ~ 18 m/s) is larger than the values obtained for the air injection experiments in section 3.3.5 ($|\overline{V}|$ ~ 10 m/s). Furthermore, the range of velocity values for fuel injection at 110 bar ($|\overline{V}|$ = 1 – 18 m/s) is greater than the range of values obtained for the air injection pressure of 110 bar ($|\overline{V}|$ = 3 – 9 m/s). The higher values and ranges are expected for fuel injection given that the jet penetration is a function of the density ratio between the injected fluid and the in-cylinder air. This density ratio is lower for the air injection thus the penetration towards the spark plug is reduced and lower velocities result downstream the spark plug. The lower velocity values downstream the spark plug for fuel injection can result from the stronger impact of the liquid spray onto the spark plug electrodes which can greatly reduce the momentum of the flow in the wake region of the spark plug.

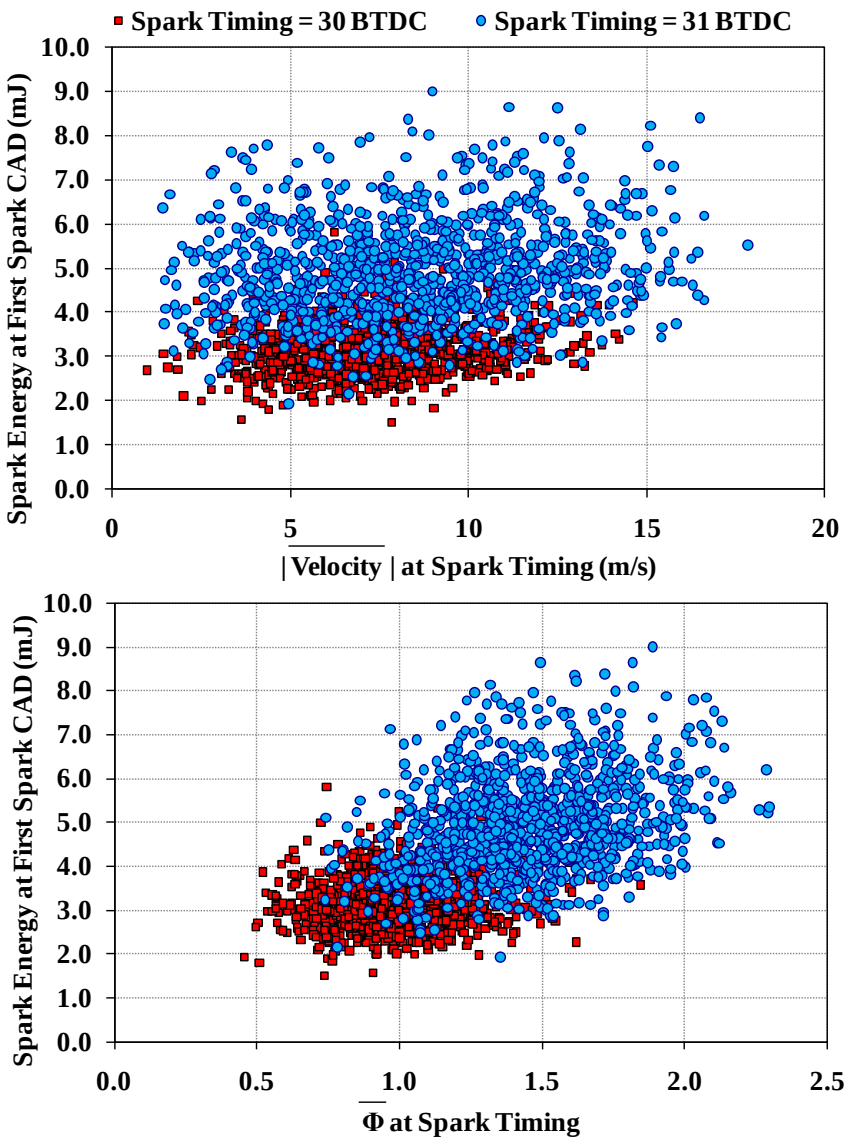

Figure 4-7: Spark energy released during the first spark CAD is affected by the velocity and fuel-air distribution near the spark plug at the time of spark. Higher spark energies exist for cycles with a spark timing of 31° BTDC than for cycles at 30° BTDC because of the stronger velocities and richer mixtures.

The trend between spark energy and equivalence ratio is much more defined shown in the bottom graph of Figure 4-7. Spark energy is shown to increase with increasing values of the spatial-averaged equivalence ratio near the spark plug. This is in agreement with the trends revealed in section 3.3.4 (see Figure 3-4). The increase in spark energy with respect to equivalence ratio shown in Figure 4-7 is not restricted to a

linear fit curve as was used for the results in section 3.3.4 (Figure 3-4). It should be noted that the experiments result presented in section 3.3.4 involved homogeneous fuel-air mixtures, while results with late-injection operation have highly stratified mixtures and the equivalence ratio values reported are spatially-averaged from the 4 mm x 4 mm region downstream the spark plug from the PLIF measurements. Furthermore, spark energies reported in section 3.3.4 were total spark energies not just the spark energy at the onset of spark. Nonetheless, the positive trend shown in Figure 4-7 is consistent with the results presented in section 3.3.4 and is within the same equivalence ratio range (Φ = 0.5 – 2.3).

Spark energy during the first spark CAD as a function of shear strain rate and vorticity values measured at the onset of spark is shown in Figure 4-8. The increase in spark energy can be shown to be associated with the stronger shear strain rate measured for the spark timing of 31^{o} BTDC. The increase in spark energy with respect to the increase in shear strain rate is consistent with the results presented in section 3.3.5 for air injection over the same shear strain rate range ($|\sigma|$ = 100 – 2000 1/s). Vorticity values (shown in the bottom graph of Figure 4-8) are similar for the different spark timings and thus do not show a trend with respect to spark energy. This does not provide further insight about the unexplained relationship between spark energy released and vorticity as presented in section 3.3.5.

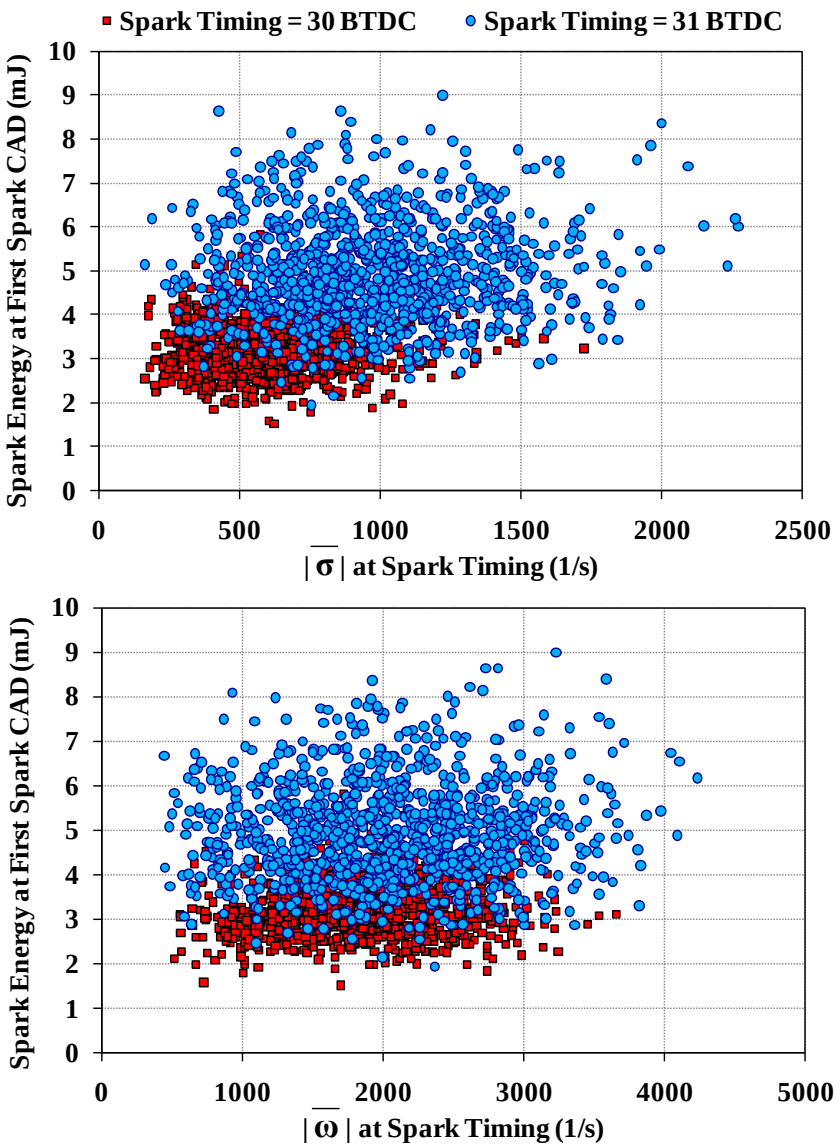

Figure 4-8: Top: Higher shear strain rates at the earlier spark timing also lead to greater spark energy during the first spark CAD. Bottom: Vorticity values are similar for the two spark timings and thus do not show a defined relationship with spark energy.

These trends for fuel injection are consistent with the trends presented for well-defined conditions in chapter 3, namely – available spark energy increases with increasing equivalence ratio, velocity magnitude, and shear strain rate. Also weak correlations can exist for cycle-resolved velocity data given the large spread in the data for highly turbulent conditions.

The richer mixtures, higher velocities, and greater spark energies present at a spark timing of 31^{o} BTDC all well-suited to provide sufficient ignition stability. For fuels whose molecular weight is greater than the oxidizer (as for isooctane air mixtures), richer mixtures require lower minimum ignition energies for reliable ignition [57]. This is primarily due to the preferred diffusion of the lighter deficient oxygen molecules compared to the abundant heavier fuel molecules which mitigate flame quenching for curved flame kernels and promote stable flame kernel development [28and 58]. Higher velocities will stretch the plasma channel exposing the channel to a larger volume of mixtures, increasing the likelihood that the plasma channel will interact with ignitable mixture. Lastly, greater spark energies transferred into the mixture can generate larger initial flame kernels faster [4] increasing the likelihood of further consuming the stratified mixture. However, conditions near the spark plug for a spark timing 1 CAD off its optimum (ST = 30^{o}) are still adequate to provide ignition. Therefore, the investigation of ignition instabilities at this operating condition is of high interest.

4.5 In-Cylinder Conditions for Range of External Dilution Levels

To compare in-cylinder conditions that exist near the spark plug for different dilution levels, flow field and fuel distribution images were analyzed in the 4 mm x 4 mm region downstream the spark plug at the onset of spark for each dilution level (0%, 10%, 18%, and 26%). In total, 1044 cycles were analyzed at each dilution level with a spark timing of 31^{o} BTDC. Velocity magnitude and equivalence ratio were the only major quantities significantly affected by the dilution level. Figure 4-9 shows ensemble-spatial average values of velocity magnitude and equivalence ratio at the onset of spark for each

dilution level. Bars shown in the graph indicate one standard deviation of the 1044 measurements at each dilution level.

Velocity magnitude is shown to increase as dilution level increases. This can be explained by the greater momentum of the liquid fuel plume for seen for diluted operation. As previously mentioned, external dilution into the cylinder reduces in-cylinder temperatures. As a result, liquid fuel evaporation is less during the injection event and the liquid fuel plume penetrates greater distances into the combustion chamber. The denser liquid fuel plume impacts the spark plug electrodes with greater momentum and ultimately increases the velocity downstream the spark plug. Despite the greater momentum near the spark plug, values of shear strain rate and vorticity do not show an apparent trend with dilution level and are therefore not included in Figure 4-9.

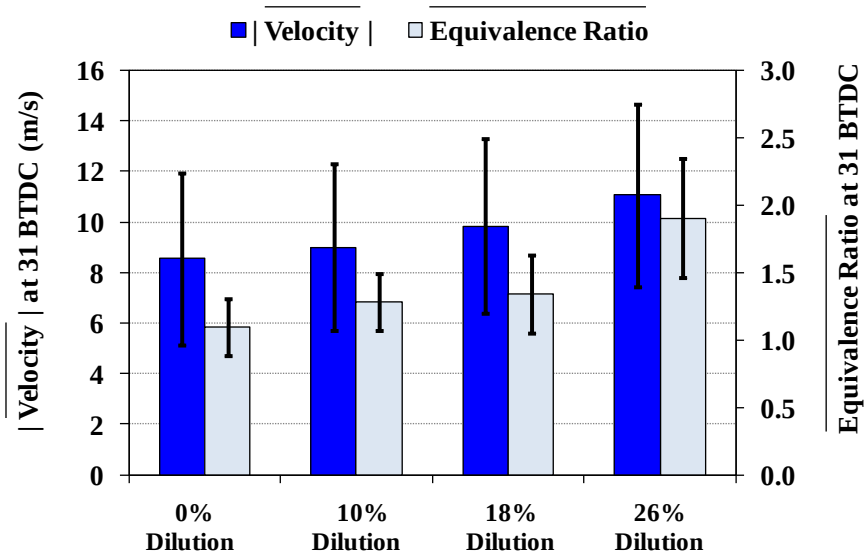

Figure 4-9: Averaged values of velocity increase with dilution due to higher momentum of spray from longer evaporation times of the liquid fuel. Averages values of equivalence ratio slightly increase with dilution level because N_2 displaces oxygen in intake air, producing richer mixtures.

Equivalence ratio is also shown to increase with increasing dilution levels. This is of no surprise since the added nitrogen from the dilution displaces the oxygen in the

intake air and ultimately reduces the oxygen level in the combustion chamber. As a result the equivalence ratio increases as dilution level increases.

The spark energy during the first CAD was not significantly affected by the slightly stronger velocities and richer mixtures near the spark plug for the increased dilution levels.

4.6 Conclusions

Optimum engine performance is found for low-load idle conditions. Spark timing one crank-angle degree off its optimum provides similar engine performance to that of the optimum spark timing, with the exception of rare ignition instabilities. Introduction of nitrogen dilution to simulate exhaust gas recirculation provides additional ignition instabilities at the given spark timings of 30^{o} and 31^{o}. Flow field and fuel concentration measurements adequately describe the conditions that exist near the spark plug at the time of spark for the different spark timings. These in-cylinder conditions ultimately affect the available spark energy, and the findings are consistent for well-defined in-cylinder conditions presented in chapter 3.

CHAPTER 5

FLOW FIELD, FUEL CONCENTRATION, AND SPARK DISCHARGE MEASUREMENTS AT SPARK TIMING

5.1 Introduction

In an attempt to identify the cause of rare errant cycles, measurements of spark discharge, flow field, and fuel distribution are obtained to characterize the in-cylinder conditions that exist for errant cycles in comparison to well-burning cycles. Measurements are presented for engine operating conditions that provided misfire and partial burn cycles; namely a spark timing of 30^{o} BTDC with 0%, 10%, and 18% external dilution levels and a spark timing of 31^{o} with 18% and 26% external dilution levels. Measurements associated for each operating condition are presented in an individual manner to adequately compare errant cycles to well-burning cycles at the same operating condition.

In particular, spark energy and duration are calculated to assess the range of values for errant and well-burning cycles to determine if abnormal spark behavior is associated for cycles with ignition instability. A theoretical minimum ignition energy value is also calculated based on thermodynamic properties to determine if the available

spark energy during the first spark crank-angle degree is theoretically sufficient to provide successful combustion.

In addition, spatial averaged quantities of equivalence ratio, velocity magnitude, shear strain rate magnitude, and vorticity are extracted from the 4 mm x 4 mm region downstream the spark plug at the onset of spark. Results reveal the range of fuel concentrations and flow fields in which misfire and partial burn cycles occur for each operating condition (i.e. spark timing and dilution level).

5.2 Experimental overview

Rare misfires and partial burn events were investigated under a range of external nitrogen dilution levels (0%, 10%, 18%, and 26%). The fixed engine operating conditions for this investigation are presented in chapter 4. With a fixed end-of-injection of 32^{o} BTDC, a spark timing of 31^{o} BTDC was found to provide optimum engine performance. As the spark timing was retarded one crank-angle to 30^{o} BTDC, IMEP values were comparable to those seen under the optimum spark timing with the exception of rare misfire and partial burn cycles. Table 5-1 provides the number of misfire and partial burn cycles that occurred at the two spark timings and range of dilution levels. At the spark timing of 30^{o} BTDC, rare misfire and partial burn cycles occurred at the dilution levels of 0% and 10%. As dilution level increased to 18%, engine performance was compromised due to multiple misfires and partial burns that the dynamometer had difficulty controlling the engine speed. This indicated the upper dilution level limit at the spark timing of 30^{o} BTDC. At the spark timing of 31^{o} BTDC, rare misfire and partial burn cycles did not occur until the dilution level was increased to 18%. As the dilution level increased to

26%, the number misfire and partial burn cycles increased dramatically that these events were no longer considered rare (< 1% occurrence).

Flow field and fuel concentration images were acquired during the compression stroke (i.e. 44 BTDC – 5 ATDC) for 348 consecutive fired cycles. Experiments were repeated multiple times to obtain a sufficient number of misfires (> 10 cycles) at each spark timing and dilution level. Results are presented for operating conditions that provided misfire and partial burn cycles, namely: spark timing of 30^{o} BTDC with 0%, 10%, and 18% dilution levels and spark timing of 31^{o} BTDC with dilution levels of 18% and 26%. In-cylinder conditions at each given spark timing and dilution level are presented in individual graphs to adequately compare errant cycles to well-burning cycles at the same operating condition.

Nitrogen Dilution Level	Spark Timing 30^{o} BTDC		Spark Timing 31^{o} BTDC	
0%	Total Cycles:	4523	Total Cycles:	1044
	Misfire Cycles:	18	Misfire Cycles:	0
	Partial Burn Cycles:	27	Partial Burn Cycles:	0
10%	Total Cycles:	2087	Total Cycles:	1392
	Misfire Cycles:	26	Misfire Cycles:	0
	Partial Burn Cycles:	25	Partial Burn Cycles:	1
18%	Total Cycles:	350	Total Cycles:	2430
	Misfire Cycles:	11	Misfire Cycles:	17
	Partial Burn Cycles:	14	Partial Burn Cycles:	30
26%	Total Cycles:	-	Total Cycles:	1044
	Misfire Cycles:	-	Misfire Cycles:	37
	Partial Burn Cycles:	-	Partial Burn Cycles:	36

Table 5-1: Number of misfire and partial burn cycles obtained at each external dilution level. With a fixed EOI at 32^{o} BTDC, two spark timings 30^{o} and 31^{o} BTDC were used to obtain rare ignition instability events for a range of nitrogen dilution levels from 0-26%.

5.3 Results

5.3.1 Spark Characterization for Ignition Failures

5.3.1.1 Spark Energy and Duration

Spark energy and spark duration were calculated to characterize spark behavior for errant cycles and well-burning cycles. Measurements for the spark timing of 30^{o} BTDC are shown for the dilution levels of 0%, 10% and 18% in Figure 5-1 (a), (b), and (c) respectively, while measurements for the spark timing of 31^{o} BTDC at the dilution levels of 18% and 26% are displayed in Figure 5-1 (d) and (e). For each operating condition, the misfire and partial burn cycles are highlighted among the predominately well-burning cycles. It is shown that the spark discharge characteristics for the errant cycles occur within the same general population of well-burning cycles. More specifically, the errant cycles are not restricted to abnormally short spark durations (< 1ms) or abnormally low spark energies (< 10 mJ), which have been identified as the cause of misfire cycles in previous investigations [29 and 38]. For certain operating conditions (i.e. specific spark timing and dilution level), spark behavior for the errant cycles are predominately within a range of values. For example, with a spark timing of 30^{o} BTDC and 0% dilution (Figure 5-1 (a)), errant cycles predominately occur within the lower spark energy (< 45 mJ), longer spark durations (> 1.7 ms) spectrum of the data set. Lower energy, longer spark durations are often common for stationary plasma channels as opposed to plasma channels that stretch beyond the spark plug electrodes. Unfortunately, the plasma channel length was not obtained from the 2-D images acquired for the flow field and fuel concentration measurements and thus cannot be quantified. Therefore, this trend should only be recognized as an observation at this point in the

analysis. Similarly, for a spark timing of 31^{o} BTDC with 18% dilution (Figure 5-1 (d)), errant cycles show a slight bias towards the lower end of the spark energies for a given spark duration. Previous studies have shown that the probability of successful ignition increases as more energy is deposited into the mixture [29]. However, since the errant cycles occur well within the range well-burning cycles, this cannot be suggested as the cause of the errant cycles. For the other operating conditions presented, the spark discharge characteristics for errant cycles are equally distributed over the range of values shown for the well-burning cycles. The data presented for each operating condition arguably suggests that abnormal spark behavior was not the cause of the errant cycles presented in this investigation.

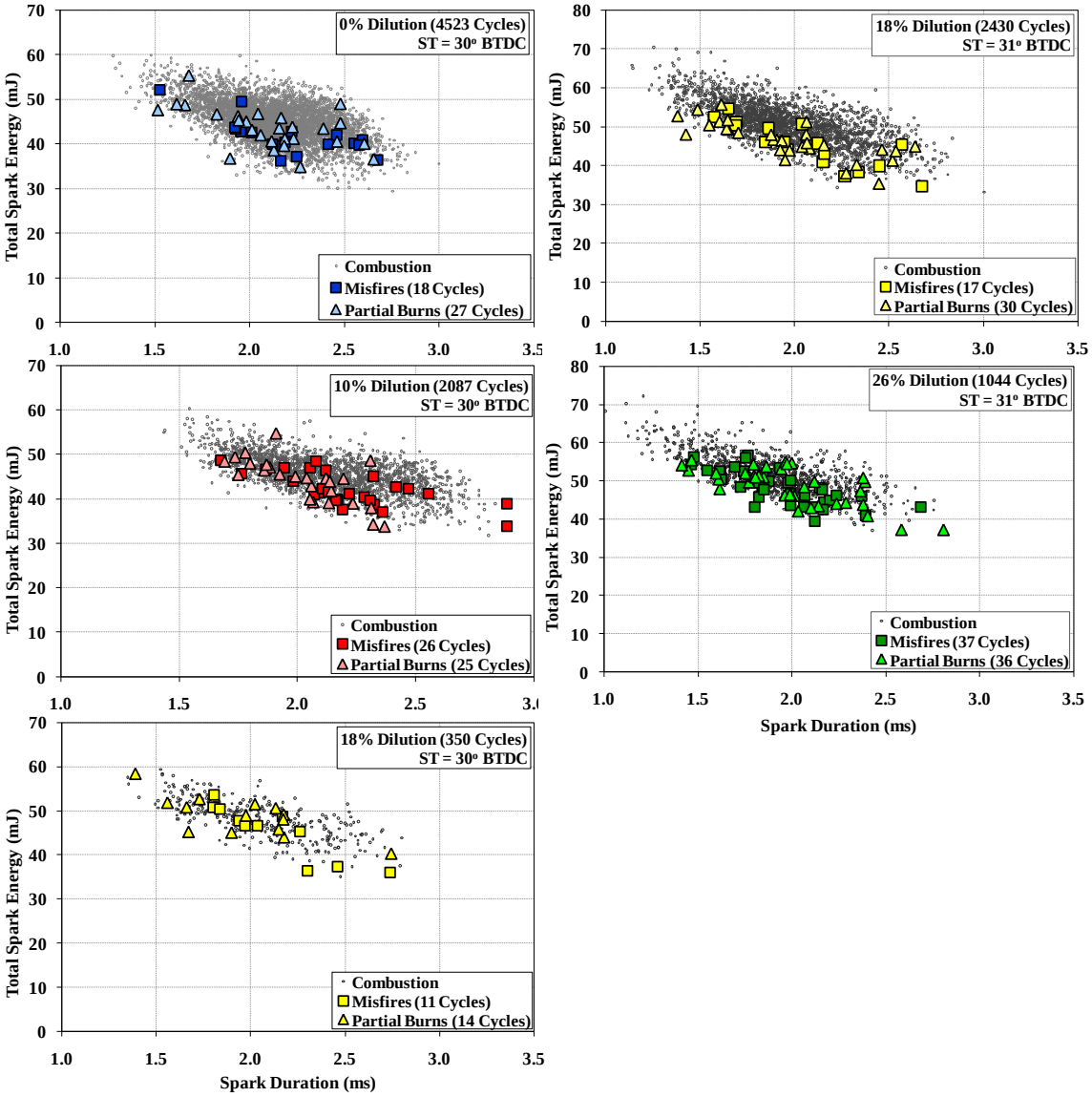

Figure 5-1: Spark energies and durations for misfires and partial burn cycles are within the general population of well-burning cycles. It can therefore easily be concluded that abnormal spark behavior was not the cause of the rare misfire or partial burn cycles.

5.3.1.2 Minimum Ignition Energy

In this section, a theoretical expression is used to calculate the minimum ignition energy required to ignite fuel-air mixtures presented in this study. These values are calculated to analyze whether the available spark energy recorded for the first spark crank-angle degree is sufficient to ignite the given mixture for the misfire cycles.

In most practical situations, the spark energy deposited into the mixture is the most important parameter for successful ignition [26]. In this regard, the minimum ignition energy is a quantity of interest and is defined as the minimum spark energy needed to reliably ignite a flammable mixture. Minimum ignition energy has been obtained and presented in the literature for various flammable mixtures at ambient conditions [27, 57, and 59 among others]. Unfortunately, values of minimum ignition energy specific to the engine operating conditions for this study are not available within the literature. Therefore an expression developed by Glassman and Yetter [59] is used to calculate the minimum ignition energy for the thermodynamic in-cylinder environment relevant to this study. This expression is given as:

$$\text{Minimum Ignition Energy} = 4/3\pi r_C^{\,3}\ \rho c_P\ T_b - T_0 \tag{5-1}$$

where r_C is the critical flame kernel radius, ρ is the gas density, c_P is the specific heat at constant pressure, T_b is the adiabatic flame temperature, and T_0 is the ambient temperature. The critical flame kernel radius is defined as:

$$r_C = 3k/\ \rho_b c_P S_L \tag{5-2}$$

where k refers to the heat conductivity of the surrounding gas, ρ_b is the burned gas density, and S_L is the laminar flame speed for the given mixture. These expressions, however do not account for effects such as flow velocity or turbulence. Flowing mixtures at the spark plug elongate the plasma channel and the energy within the plasma channel is distributed over a larger volume. This in turn reduces the temperature along the plasma

channel and requires an overall larger energy within the plasma channel for successful ignition [59]. If the flow is turbulent, there is additional heat loss from the flame kernel due to higher strain, which ultimately requires an increase in ignition energy to develop a larger initial flame kernel [7, 29, 60, and 61]. Maly [4] has demonstrated that larger initial flame kernels are better suited to withstand higher turbulence levels. A flame kernel twice its original size was able to endure turbulence levels that extinguished a flame kernel of its original size. Therefore, to account for flow and turbulence in the calculation for minimum ignition energy, the critical flame kernel radius expressed in (5-2) was increased by a factor of two to provide a reasonable estimate of the minimum ignition energy needed for flow conditions relevant to this study. The values of each parameter in the expressions for critical flame kernel radius and minimum ignition energy are presented in Appendix D.

Table 5-2 reports the calculated theoretical values of critical flame kernel radius and minimum ignition energy for lean-to-stoichiometric isooctane air mixtures. Mixtures richer than stoichiometric, yet still within the flammability limits ($1.0 \leq \Phi \leq 3.0$), require less spark energy for ignition. This effect is caused by the preferred mass diffusivity of the deficient species (oxygen) for rich mixtures (i.e. Lewis number > 1), which produces favorable flame expansion. Theoretically, the largest ignition energy needed to ignite a flammable mixture is 4.61 mJ for a lean mixture of $\Phi = 0.5$. This value can now be used to evaluate whether the available spark energy during the first few crank-angles is sufficient to theoretically ignite the given mixture for the misfire cycles.

Equivalence Ratio	Critical Flame Radius [mm]	Minimum Ignition Energy [mJ]	Critical Flame Radius for Turbulent Flows (x2) [mm]	Minimum Ignition Energy for Turbulent Flows [mJ]
0.5	0.25	0.58	0.5	4.61
0.6	0.17	0.19	0.33	1.55
0.7	0.13	0.10	0.25	0.77
0.8	0.11	0.060	0.21	0.48
0.9	0.091	0.042	0.18	0.34
1.0	0.086	0.038	0.17	0.30

Table 5-2: Theoretical values of critical flame kernel radius and minimum ignition energy from equations 5-1 and 5-2 for lean-to-stoichiometric isooctane air mixtures. An estimate of minimum ignition energy for a spark event in a turbulent flow field is obtained by calculating the minimum ignition energy with a critical flame kernel radius twice as large as the value for stagnant flow.

5.3.1.3 Initial Spark Energy

For the spray-guided approach, there is a limited amount of time in which the spark plasma is exposed to an ignitable mixture and the spark energy within the first few crank-angles after the onset of spark must be sufficient to initiate a flame kernel. Therefore, this section presents the available spark energy for the first spark crank-angle degree and compares these values to the theoretical values of minimum ignition energy. The initial spark energy is correlated with the spatial averages of equivalence ratio and velocity magnitude within the 4 mm x 4 mm region downstream the spark plug to reveal the in-cylinder conditions that exist near the ignition site.

As previously mentioned in chapter 3, the 4 mm x 4 mm region was selected to extract named quantities because it was the region that contained the plasma channel as it was convected from the spray induced flow field. The sensitivity of the size and location of this extraction region is provided in Appendix A. For the combined PIV / PLIF measurements, the 4 mm x 4 mm region provided the optimum extraction region because it was the smallest region that had an adequate number of velocity vectors (9 velocity vectors) that was suitable to obtain velocity gradient information for the highly turbulent

flow field imposed by the spray event. The measurements were extracted at the onset of spark. Quantities in the 4 mm x 4 mm region after the onset of spark were not available because a flame kernel often existed within this region, which interfered with the quantitative velocity and fuel fluorescence measurements.

The breakdown event associated with the spark discharge is not resolved in the spark measurements and therefore the spark energy released during the first spark CAD begins at the onset of the arc phase once the voltage stabilizes after the initial voltage peak. The amount of energy released during the breakdown is often on the order of 20% of the total spark energy [4].

To provide a succinct yet thorough evaluation of available spark energy, measurements are focused on the operating condition with spark timing of 30^{o} BTDC and 0% dilution. This operating condition consists of misfire cycles that primarily exhibit the lower spark energies than misfire cycles at the other dilution levels and at the spark timing of 31^{o} BTDC. A discussion of the correlations between spark energy and spatially averaged quantities of equivalence ratio and velocity magnitude for all operating conditions is presented in Appendix E.

Figure 5-2 presents the available spark energy during the first spark crank-angle degree and spatially averaged quantities of equivalence ratio and velocity magnitude. The misfire and partial burn cycles are highlighted among the predominately well-burning cycles. It is revealed that the misfire cycles occur for lower spark energies (1.5 mJ – 3.5 mJ), but contain flammable mixtures nearby the spark plug ($0.5 \leq \overline{\Phi} \leq 1.1$) and low to moderate velocities ($0.5 \text{ m/s} \leq \overline{V} \leq 8.0 \text{m/s}$) near the spark plug. The range of equivalence ratios and the incorporation of the flow and turbulence on minimum ignition energy

presented in Table 5-2 sufficiently capture the range of in-cylinder conditions for the misfire cycles presented in Figure 5-2.

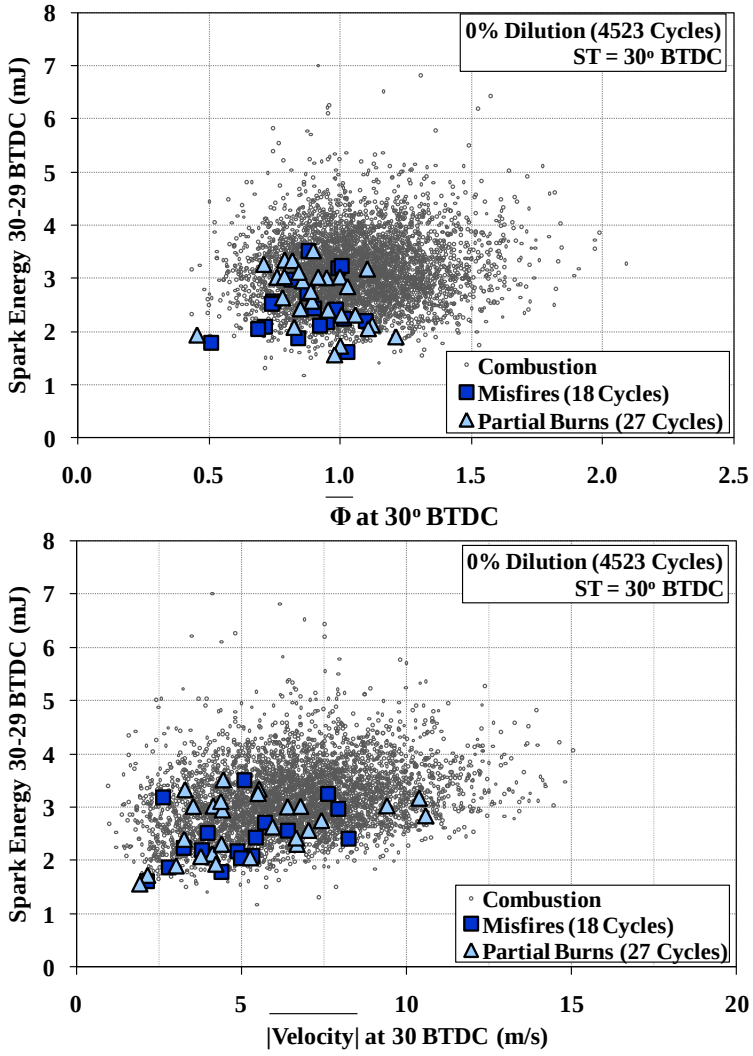

Figure 5-2: Available spark energy for misfire cycles (excluding losses) is above the theoretical minimum ignition energy value for the flammable mixtures and moderate velocities that exist in the 4 mm x 4 mm region at the onset of spark.

With the exception of cycles with mixtures leaner $\Phi < 0.6$, the available spark energy during the first spark crank-angle degree for all cycles is greater than the theoretical minimum ignition energy calculated for turbulent flows at a given equivalence ratio. However, factors such as energy transfer efficiency are not accounted for in Figure

5-2. Lewis and von Elbe [28] have revealed that spark energy loss due to heat transfer to the spark electrodes can be on the order of 50% of the available spark energy. When accounting for this energy loss, the spark energy released during the first spark CAD can be lower than the theoretical spark energy needed to ignite the mixture. However, Figure 5-2 reveals that even well-burn cycles have spark energies lower than what is theoretically needed for ignition yet do not encounter ignition instability. It should again be mentioned that the spark energies presented in Figure 5-2 do not include the breakdown energy which provides additional spark energy that can result in ignition. As previously mentioned the breakdown energy often contributes to 20% of the total spark energy. However, since the breakdown energy cannot be accurately quantified in these spark measurements it is then relevant to evaluate the additional spark energy released directly after the first spark crank-angle degree. Figure 5-3 shows the ensemble-averaged spark energy values during each crank-angle degree for the first four crank-angles of the spark discharge. These values are presented for the 4523 cycles shown in Figure 5-2. Bars indicate one standard deviation of the 4523 spark measurements. Even when accounting for the 50% energy transfer efficiency, the spark energy released within the first two crank-angle degrees is greater than the theoretical energy required for successful ignition. Despite the fact that mixtures downstream of the spark plug become leaner with time after the end-of-injection, the available spark energy within the first four crank-angle degrees should theoretically be sufficient to develop a flame kernel for each cycle. Therefore, insufficient spark energy is not considered to be the cause of the misfire cycles presented here.

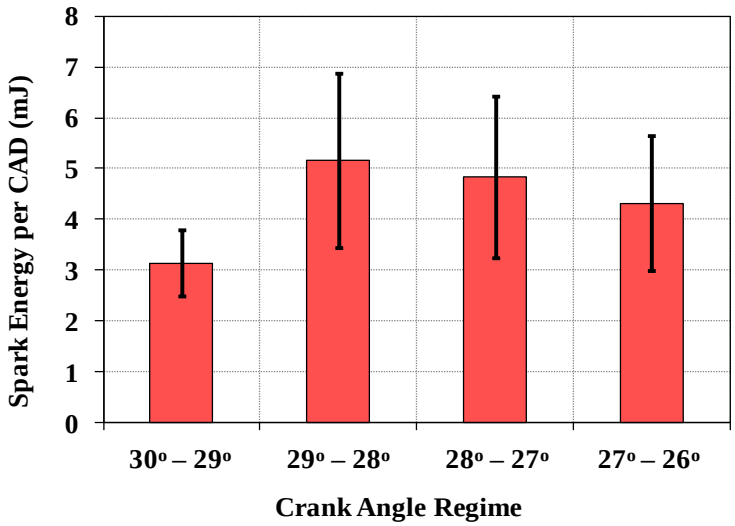

Figure 5-3: Ensemble-averaged spark energy for each crank-angle during the first four crank-angles after the onset of spark. Accounting for spark energy losses up to 50%, the spark energy within the first two crank-angle degrees of the spark is greater than the theoretical minimum ignition energy values. Bars indicate one standard deviation of the 4523 measurements.

5.3.1.4 Correlation of Spark Energy and Measurements of Flow Field and Fuel Concentration

The spark energy for the first spark crank-angle degree is correlated with spatially averaged quantities of equivalence ratio, velocity magnitude, shear strain rate magnitude, and vorticity magnitude measured in the 4 mm x 4 mm region at the onset of spark. This data is analyzed for each spark timing (30^o and 31^o BTDC) and dilution level. This analysis was conducted to compare the results for late injection, stratified operation to the findings for the well-defined conditions presented in chapter 3. This analysis is greatly detailed but the findings do not provide additional insight to identify the cause of the errant cycles which is context of this chapter. Therefore, this analysis is presented in Appendix E and a brief summary of the findings is presented here.

Overall, the data exhibits large cycle-to-cycle variation in the measurements (as can be seen in Figure 5-2) and thus the correlations between the spark energy and quantities extracted from the 4 mm x 4 mm region are weak. This is of no surprise since

the cycle-resolved spark energy and flow field data for the air injection experiments presented in chapter 3 also exhibited large cycle-to-cycle variation and weak correlations. Results for most operating conditions (i.e. specific spark timing and dilution level) reveal a positive weak relationship between the spark energy and the quantities extracted from the 4 mm x 4 mm region, while other operating conditions exhibit such a large spread in the data that no significant correlation was found. The inability to extract named quantities along the spark plasma channel is a likely explanation for the weak correlations for known relations.

5.3.2 Equivalence Ratio and Flow Field Measurements

It has thus far been determined that abnormal spark behavior and insufficient spark energy are not attributed as the cause of the misfire or partial burn cycles. To continue this investigation it is now necessary to quantify measurements of fuel concentration and flow field quantities near the spark plug for the errant and well-burning cycles. Therefore, measurements of equivalence ratio, velocity magnitude, shear strain rate magnitude, and vorticity were extracted from the 4 mm x 4 mm region at the time of spark to characterize the in-cylinder conditions for spark ignition. In this analysis the misfire and partial burn cycles are highlighted among the predominately well-burning cycles to articulate the similarities and differences between errant cycles and well-burning cycles at each operating condition.

Figure 5-4 shows spatial averaged measurements of equivalence ratio and velocity magnitude for the spark timings and dilution levels investigated. Overall, it is shown that all misfire and partial burn cycles occur with the same general population of well-burning cycles at each operation condition. It can also be shown that for some dilution levels

errant cycles are more commonly within a limited range of values. For example, at a spark timing of 30^o BTDC and 0% dilution (Figure 5-4 (a)), misfire and partial burn cycles are more common for velocities below 8m/s and mixtures leaner than $\overline{\Phi} = 1.1$. There are however three partial burns that occur for higher velocities (9 m/s < $\overline{V}$ < 11 m/s). As dilution level increases to 10% at this spark timing (Figure 5-4 (b)), the misfire and partial burn cycles are less restricted to stoichiometric-to-lean and lower than average velocity mixtures. As dilution level increases further to 18% (Figure 5-4 (c)), misfires and partial burns are no longer considered rare and engine performance deteriorates significantly. In fact with the spark timing of 30^o BTDC and the dilution level of 18% only 350 total cycles were captured due to difficulty in stabilizing the engine speed for greater than 200 consecutive cycles. The misfires and partial burns that occur at this spark timing and dilution level appear to be insensitive to the initial fuel concentration and velocity near the spark plug as these errant cycles occur for the whole range of equivalence ratio and velocity values measured ($0.6 \leq \overline{\Phi} \leq 1.6$, 3 m/s $\leq \overline{V} \leq$ 13 m/s).

At dilution levels of 18% and 26%, spark timing was advanced to 31^o BTDC to stabilize engine performance. With a dilution level of 18%, misfire and partial burn cycles are again more common for the leaner ($0.8 \leq \overline{\Phi} \leq 1.8$), lower velocity (3 m/s $\leq \overline{V}$ $\leq$ 11 m/s) regime of the distribution of the well-burning cycles; however, the errant cycles are still within the general population of well-burning cycles. At the higher dilution level of 26% (Figure 5-4 (e)), misfire and partial burn cycles are again insensitive to the initial fuel concentration and velocity magnitude near the spark plug as the errant cycles occur for the whole distribution of well-burning cycles ($1.5 \leq \overline{\Phi} \leq 3.5$, 3 m/s $\leq \overline{V} \leq$ 18 m/s).

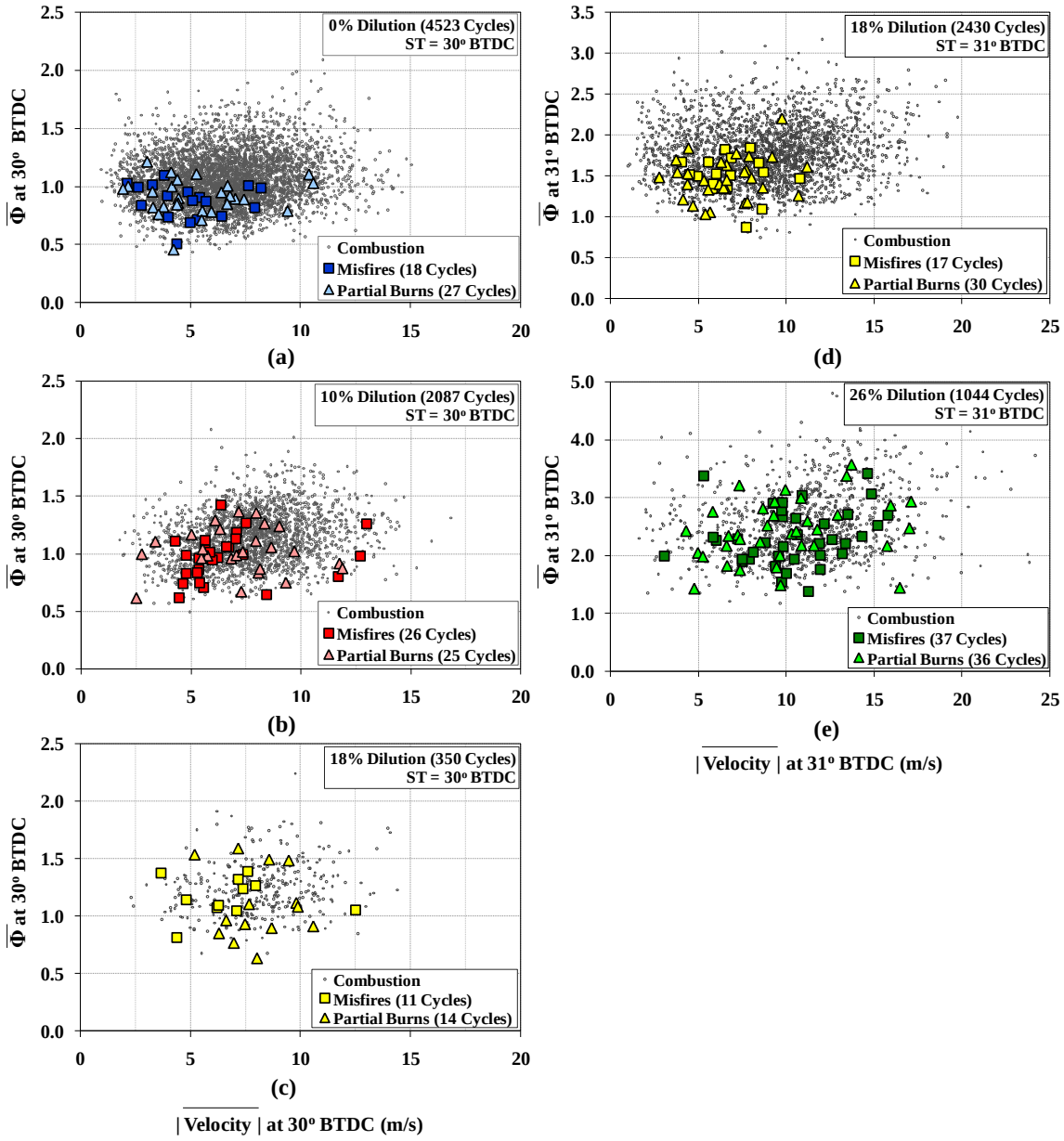

Figure 5-4: Spatial averaged values of equivalence ratio and velocity magnitude in the 4 mm x 4mm region at the onset of spark are shown for the spark timings of 30° and 31° BTDC and dilution levels of 0%, 10%, 18% and 26%. Overall, the misfire and partial burn cycles at each operating condition are within the general population of well-burning cycles.

The lack of errant cycles at the higher than average equivalence ratio and velocity values for the operating conditions with a spark timing of 30° BTDC and 0% dilution (figure 5-4(a)) and for the spark timing of 31° BTDC and 18% dilution level (figure 5-4(d)) is an interesting observation. Despite a large spread in cycle-resolved data in

chapter 3 (and in Appendix E), it has been revealed that spark energy increases with equivalence ratio and velocity magnitude. Although it has been theoretically shown that the available spark energy should be adequate to provide successful ignition, additional spark energy increases the initial flame kernel size [4]. In addition, higher velocities stretch the spark plasma and expose it to a larger volume of flammable mixtures which increases the likelihood of ignition. At this point in the analysis, the cause of the errant cycles is not known and these trends are only presented as observations. This topic is discussed further in chapter 6 where images within the entire viewing plane and throughout the engine cycle are presented.

Spatial averages of shear strain rate magnitude ($|\bar{\sigma}|$) and vorticity magnitude ($|\bar{\omega}|$) are correlated with one another and are shown in Figure 5-5 for the different operating conditions. The measurements distinctly shows that misfire and partial burn cycles occur for the same general population of well-burning cycles for all operating conditions presented. In addition, the misfire and partial burn cycles do not show a bias toward higher or lower values of shear strain rate or vorticity for any operating condition. It can then concluded that the misfire and partial burn cycles insensitive to the initial shear strain rate and vorticity values near the spark plug. This information thus does not provide additional information that can be used to diagnose the cause of the errant cycles.

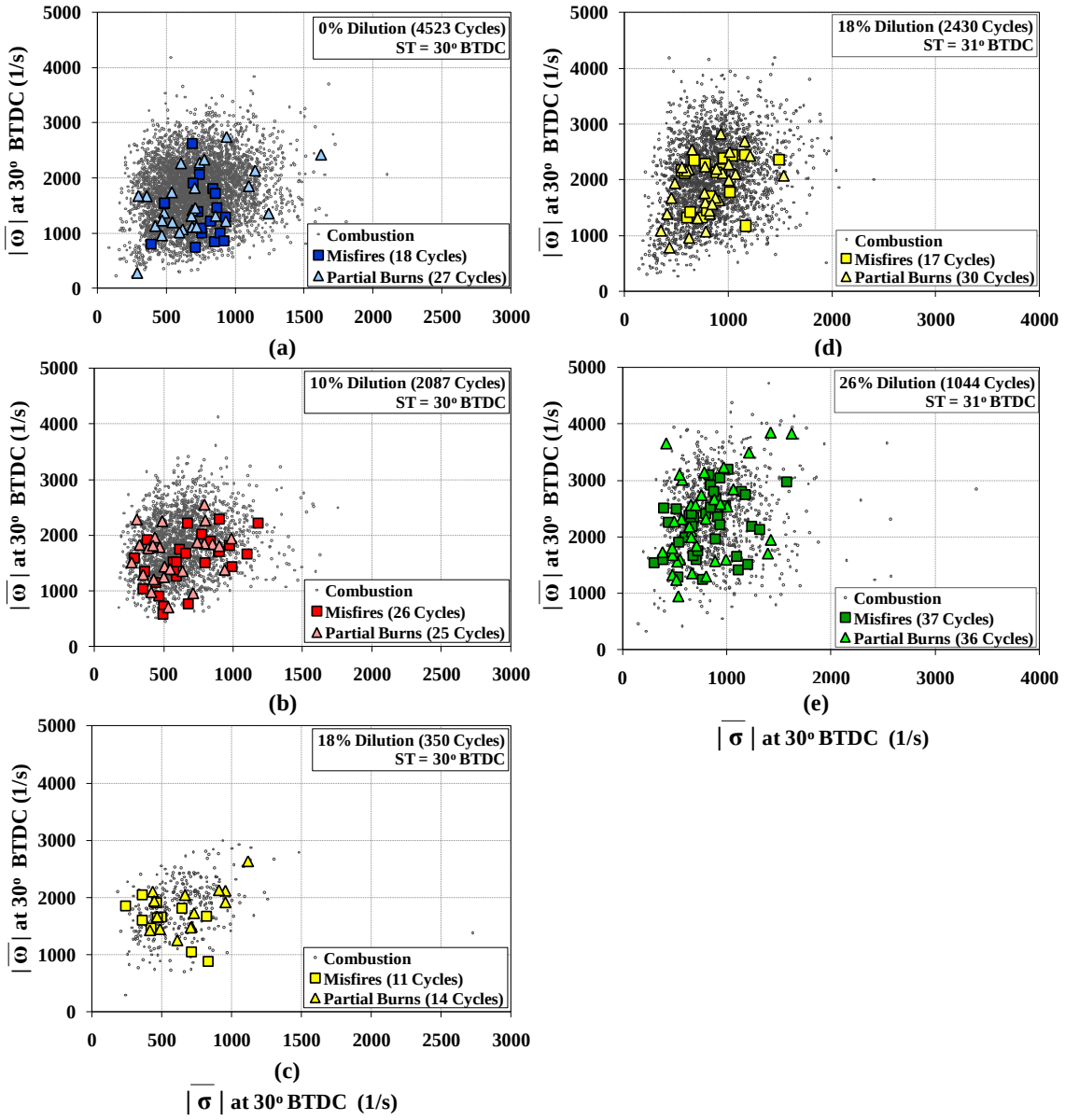

Figure 5-5: Misfire and partial burn cycles occur within the same general population of shear strain rate and vorticity values as well-burning cycles. The errant cycles span the entire range of shear strain rate and vorticity values and thus appear to be insensitive to the initial shear strain rate and vorticity values near the spark plug.

It is observed that equivalence ratio, velocity magnitude, shear strain rate magnitude, and vorticity magnitude show a slight increase in value with increasing dilution levels. As explained in chapter 4, mixtures become richer as dilution level increases because the additional nitrogen dilution reduces the amount of oxygen present

within the cylinder. Higher dilution levels also produce lower peak flame temperatures and thus reduce in-cylinder temperatures. This ultimately prolongs fuel evaporation and the greater momentum from the liquid spray produces a stronger flow with increased turbulence near the spark plug.

In addition, equivalence ratio, velocity magnitude, shear strain rate magnitude, and vorticity magnitude values increase as spark timing is advanced from 30^{o} BTDC to 31^{o} BTDC. As mentioned in chapter 4, the larger values at the spark timing of 31^{o} BTDC are present because the spray plume is still passing through the spark gap at 31^{o} BTDC.

Regardless of these fine details, the main conclusion of this analysis is that the errant cycles occur within the general population of well-burning cycles under each dilution level and spark timing. This analysis, while relevant, does not discriminate between errant and well-burning cycles and thus is insufficient to identify the cause of the misfire and partial burn cycles.

5.4 Conclusion

Measurements of spark discharge, fuel concentration, and flow field are extracted at the onset of spark for operating conditions with spark timings of 30^{o} and 31^{o} BTDC and nitrogen dilution levels of 0%, 10%, 18%, and 26%. Spark discharge properties reveal that misfire and partial burn cycles do not occur for abnormal spark events. Furthermore, the spark energy within the first two crank-angle degrees after the spark onset is greater than the estimated theoretical value of minimum ignition energy at a given equivalence ratio for all cycles. Thus, the misfire cycles should theoretically have sufficient spark energy for successful ignition. Spatial averaged values of equivalence ratio, velocity magnitude, shear strain rate magnitude, and vorticity magnitude within the

4 mm x 4 mm region for misfire and partial burn cycles are within the general population of the values for well-burning cycles. Thus this analysis does not provide significant findings that noticeably identify the cause of the errant cycles. Further analysis of the fuel concentration and flow field information for the entire viewing plane should be analyzed in attempt to identify the cause of the errant cycles.

CHAPTER 6

EVOLUTION OF FUEL DISTRIBUTION AND FLOW FIELD FOR FLAME KERNEL DEVELOPMENT

6.1 Introduction

Spark discharge, fuel concentration, and flow field measurements have thus far been analyzed in an attempt to identify the cause of misfire and partial burn cycles. Specifically spark discharge properties have shown that abnormal spark behavior and insufficient spark energy are not attributed to the errant cycles. Additionally, measurements of equivalence ratio, velocity, shear strain rate, and vorticity in the 4 mm x 4 mm region at the time of spark reveal that misfire and partial burn cycles occur within the same general population of in-cylinder measurements for well-burning cycles. Thus far, this analysis has not been sufficient to identify the cause of the misfire or partial burn cycles. Therefore, this chapter presents the temporal and spatial evolution of fuel concentration and flow field on flame kernel development for the errant and well-burned cycles. Here, the fuel concentration and flow field is analyzed within the entire viewing plane.

6.2 Misfire and Partial Burn Analysis for Cycles Without External Dilution

Misfire and partial burn cycles were obtained for a range of dilution levels at the spark timing of 30^{o} and 31^{o} BTDC. To provide a succinct yet thorough analysis of the misfire and partial burned cycles, simultaneous PLIF and PIV images are first presented for non-diluted cycles with the spark timing of 30^{o} BTDC. This operating condition is considered to be the baseline operating condition that provided rare misfire and partial burn cycles without the addition of external dilution. These images are presented to adequately reveal the common trends shown for misfire and partial burn cycles. Once these trends for the errant cycles have been quantified and identified, the effect of dilution level on the burning rate and its inherent cause of misfire and partial burn cycles for stratified operation are then presented.

6.2.1 Simultaneous PLIF, PIV, and Mie Scattering Images

PLIF and PIV images over the entire field of view (38 mm x 30 mm) were used to analyze the temporal and spatial evolution of the fuel concentration and flow field on flame kernel development for misfire, partial burn, and well-burning cycles. The size and location of the flame kernel within the 2-dimensional viewing plane was portrayed in the Mie scattering images. The flame kernel was identified as the darkened region in the Mie scattering images where seeding droplets evaporated due to the hot flame gas. The 2-D size and location of the flame kernel was extracted from the Mie scattering images and manually overlaid onto the PLIF-PIV images. A mask was used to exclude spurious velocity vectors and luminosity signals the may appear in the flame kernel region. An overlay was added to the final image to show the location of the spark plug, fuel injector, and bottom of the piston bowl. The resulting image revealed the spatial distribution of

fuel concentration, flow velocity, and flame kernel development within the 2-D viewing plane. The incorporation of the PLIF, PIV, and Mie scattering images is shown in Figure 6-1. Images at crank-angle resolution provided adequate temporal information that captured the evolution of the fuel distribution and flow field on the flame kernel development for each cycle. While the flow field within the engine is 3-dimensional (see Appendix B) and out of plane motion can exist, the results presented from the planar measurements provide adequate detail that describes the development of the flame kernel.

The seeding density optimized for PIV measurements was not suitable to develop an automated routine that could manually extract the size and location of the flame kernel for each image and cycle. Even with dilation and erosion image manipulation procedures, the darkened spacing between individual seeding particles was, at times, falsely identified as the darkened region associated with the flame kernel. In addition, the presence of combustion luminosity created difficulty in identifying the flame kernel as the darkened region within the Mie scattering images. Therefore, the spatial information of the flame kernel was extracted manually. This information was not feasible to extract for all cycles. Instead, the 2-D spatial information of the flame kernel was extracted manually for each misfire and partial burn cycle in addition to a corresponding well-burn cycle with similar initial conditions in the 4 mm x 4 mm region at the onset of spark.

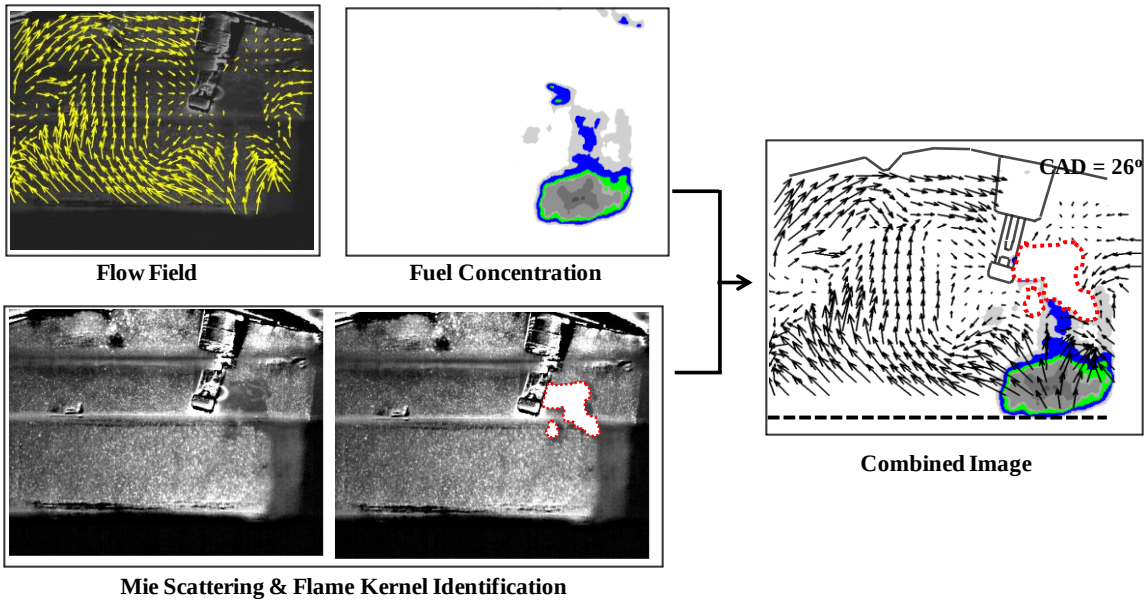

Figure 6-1: The flame kernel was identified in the Mie scattering images and manually overlaid onto the combined flow field and fuel concentration images to reveal the spatial distribution of fuel concentration, flow velocity, and flame kernel development within the 2-D viewing plane. The flame kernel is highlighted by the dotted red outline.

In an attempt to identify the cause of the errant cycles, images during each misfire and partial burn were compared to an individual well-burning cycle that had similar equivalence ratio and velocity magnitude in the 4 mm x 4 mm region at the time of spark (values within ± 5%). This allowed adequate comparison of errant cycles to well-burning cycles that had similar initial conditions for early flame kernel development. In this comparison, the temporal and spatial evolution of the fuel concentration and flow field on the early flame kernel development clearly identified the differences between the errant and well-burning cycles which was sufficient to identify the cause of the misfire and partial burn cycles within this study.

A sequence of PLIF-PIV images for a misfire and partial burn cycle are presented to illustrate the differences between the errant cycles and their respective well-burning cycle. Figure 6-2 features selected images taken for a misfire cycle and its corresponding

well-burning cycle which have mixtures just lean of stoichiometric and moderate velocity magnitudes ($\overline{\Phi}$ = 0.87 – 0.89, $\overline{V}$ = 5.7 m/s) within the 4 mm x 4 mm region at the time of spark. Similarly, Figure 6-3 compares selected images taken for a partial burn cycle and its respective well-burning cycle that have a comparable spatially averaged equivalence ratio to the cycles shown in Figure 6-2, but have a slightly higher velocity magnitude ($\overline{\Phi}$ = 0.89, $\overline{V}$ = 7.0 m/s) within the 4 mm x 4 mm region at the time of spark. The misfire and partial burn cycles shown in the figures were specifically chosen because they contained mixtures and flow velocities in the 4 mm x 4 mm region at the onset of spark that are predominately found for well-burning cycles. Even though images were recorded at each crank-angle degree, the figures only display certain images to highlight the trends seen in these cycles. The images show the flow field and fuel concentration at the end-of-injection (32^o BTDC), the onset of spark (30^o BTDC), during the spark event when a flame kernel is established (26^o BTDC), and after the spark event (21^o, 18^o, and 14^o BTDC) to show the evolution of the flame kernels. The fuel concentration is shown by the gray-scale with super-imposed blue and green colors to highlight the lean ignitable mixtures and stoichiometric mixtures respectively.

At the end-of-injection (32^o BTDC), the cycles in Figure 6-2 and Figure 6-3 show a dense fuel cloud with rich mixtures and high velocities downstream of the spark plug. At the onset of spark, the mixtures near the spark plug become leaner and exhibit lower flow velocities. While the fuel cloud downstream the spark plug for the misfire and its corresponding well-burned cycle (Figure 6-2) have distinctly different shapes, the spatially averaged equivalence ratio in the 4 mm x 4 mm region is similar ($\overline{\Phi}$ = 0.87 for the misfire cycle and $\overline{\Phi}$ = 0.89 for the well-burned cycle). The spark plasma channel for

the misfire cycle is distinctly shown between the electrodes by the high intensity. This high intensity is excluded when calculating the equivalence ratio within the 4 mm x 4 mm region. At 26^{o} BTDC, a flame kernel is established for both cycles but is significantly larger for the well-burned cycle. The flame kernel for the well-burned cycle is formed at 29^{o} BTDC (not shown), while the flame kernel for the misfire cycle is not formed until 26^{o} BTDC. The difference in the CAD in which a flame kernel is present suitably describes the discrepancies of the flame kernel size for the misfire and well-burned cycle. It is also shown that the flame kernel for the well-burned cycle is located to the side of the spark plug, while the flame kernel for the misfire cycle is primarily located below the spark plug. More importantly, the flame kernel for the well-burned cycle remains in contact with a flammable mixture during the early stages of its growth, whereas the misfire cycle shows spatial separation between the flame kernel and flammable mixture at 26^{o} BTDC. The flame kernel for the well-burning cycle grows rapidly and promptly reaches the rich mixture within the piston bowl where the flame kernel fully consumes the flammable mixture. For the misfired cycle, mixtures are significantly leaner outside of the 4 mm x 4 mm region and within the piston bowl by the time a kernel is present at 26^{o} BTDC. It appears that the leaner mixtures are insufficient to further develop the flame kernel into the piston bowl and the flame kernel disappears shortly after the spark event. It should be mentioned that while these planar measurements reveal distinct differences between errant and well-burning cycles, they cannot detect the out of plane motion nor fuel distribution within the third-dimension.

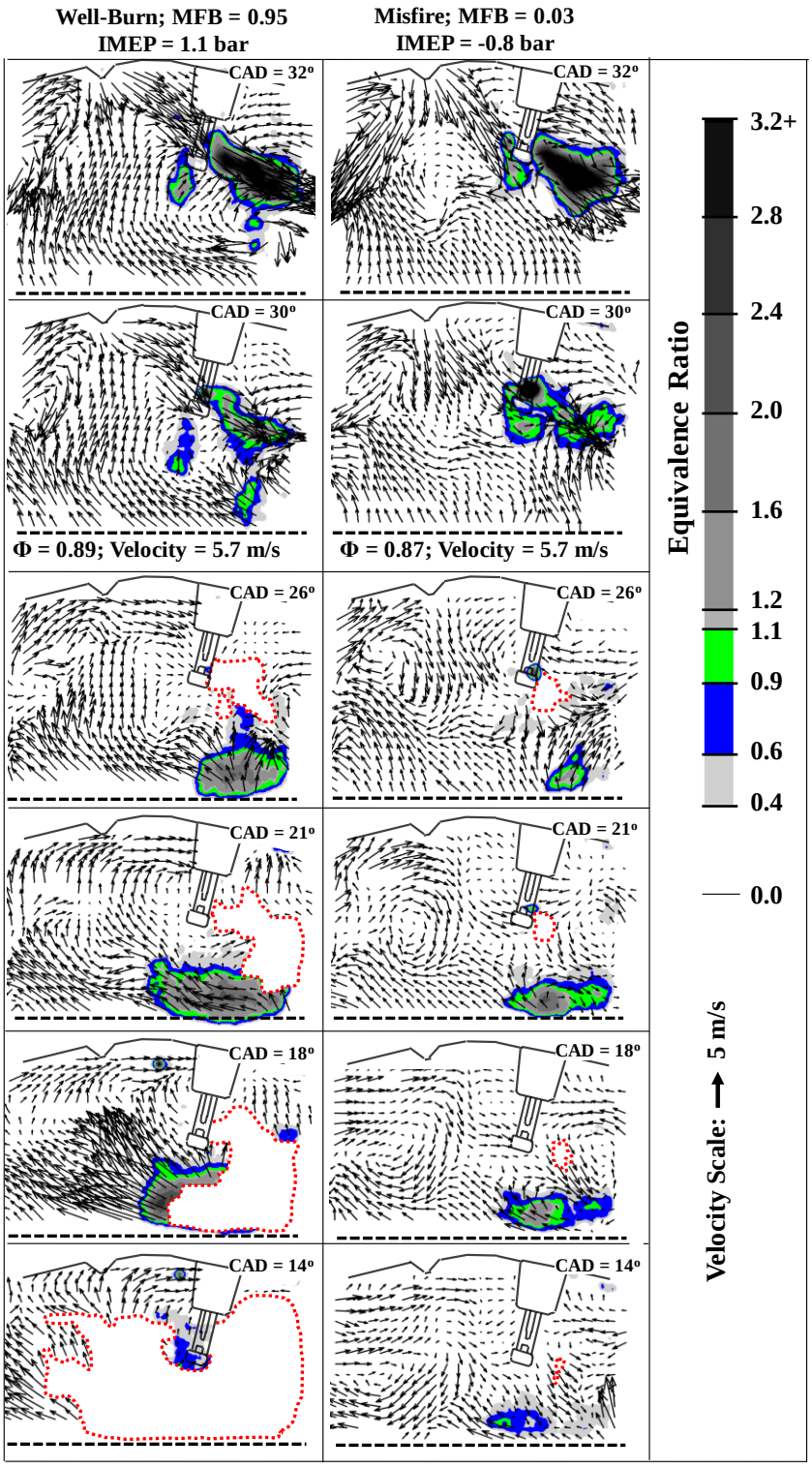

Figure 6-2: Image sequence showing the fuel distribution, velocity, and flame kernel development for a misfire and its corresponding well-burning cycle. A flame kernel is present at a later time than the well-burning cycle and is smaller and surrounded by significantly leaner mixtures which appear to be insufficient to develop the flame kernel which disappears after the spark event.

The partial burn cycle and its corresponding well-burning cycle shown in Figure 6-3 also reveal distinct differences in the flame kernel growth despite similar mixtures and flow velocities near the spark plug at the time of spark ($\overline{\Phi}$ = 0.89, $\overline{V}$ = 7.0 m/s). At 26^{o} BTDC, the flame kernel for the well-burning cycle is significantly larger than the flame kernel for the partial burn cycle. The flame kernel for the well-burning cycle is present at 29^{o} BTDC, while the flame kernel for the partial burn cycle is present a crank-angle degree later at 28^{o} BTDC. The flame kernel for the well-burning cycle is in contact with a flammable mixture at all times and by 26^{o} BTDC is already interacting with the rich flammable mixture within the piston bowl. The subsequent images show that the flame kernel then quickly consumes the mixture within the viewing plane. Similar to the misfire cycle shown in Figure 6-2, the partial burn cycle shows a spatial separation between the flame kernel and the flammable mixture to the right of the spark plug and within the piston bowl. As a result, the flame kernel for the partial burn cycle does not grow as rapidly as the flame kernel for the well-burned cycle. More importantly, the flame kernel for the partial burn cycle primarily grows horizontally and does not promptly enter into the piston bowl where the bulk of the flammable mixture is located. The flame kernel does not begin to interact with the flammable mixture until 18^{o} BTDC, when the mixture within the bowl becomes leaner with time. Ultimately the late arrival of the flame kernel into the piston bowl leads to a flame kernel interaction with a leaner mixture, presumed to be the result of longer mixing times in the bowl, and only a portion of the fuel is consumed.

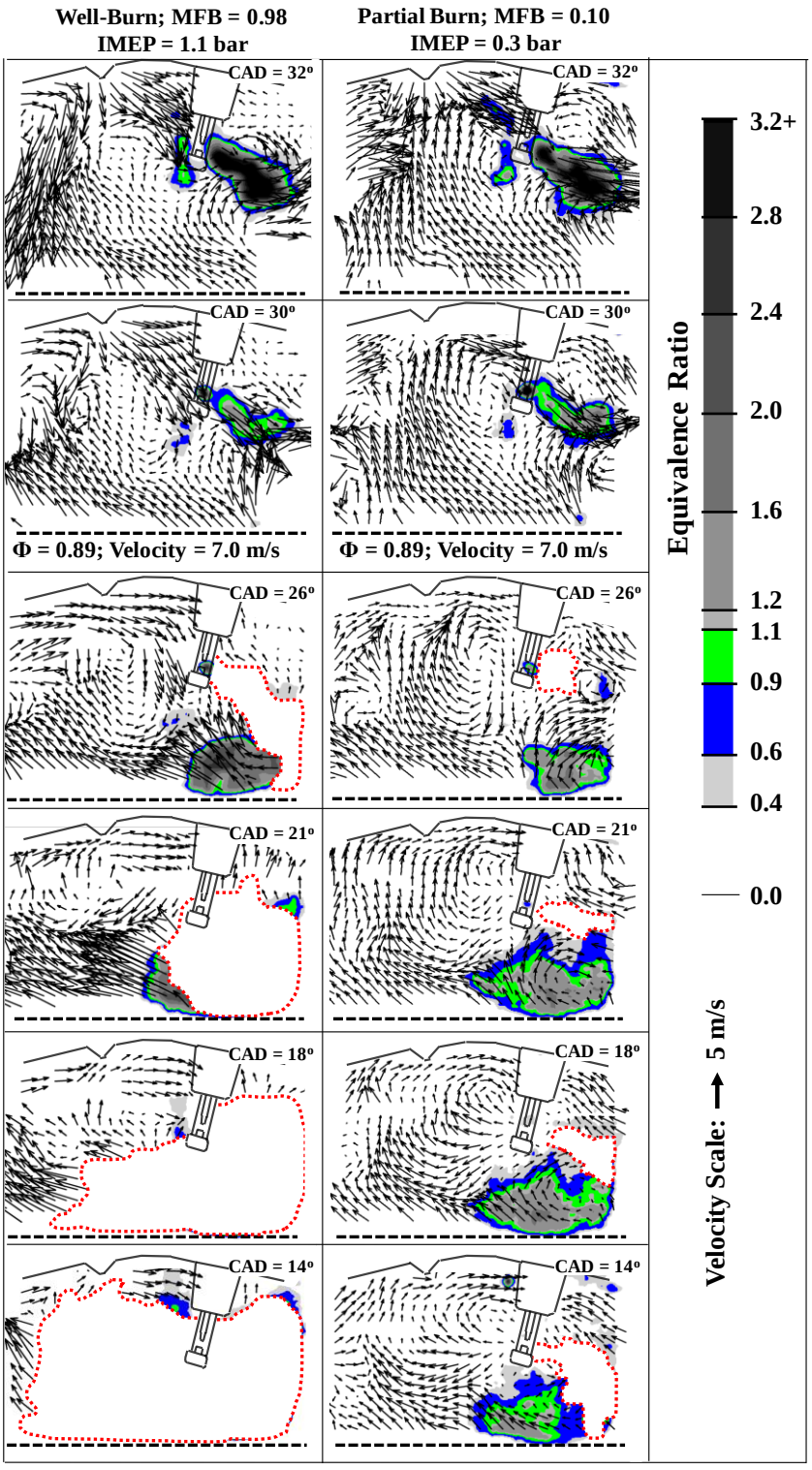

Figure 6-3: The PLIF-PIV image sequence for a partial burn and its corresponding well-burning cycle. The flame kernel for the partial burn cycle does not promptly grow into the region of the flammable mixture. The flame kernel begins to interact with the flammable at 18° BTDC when the mixture in the bowl becomes significantly leaner and only a portion of the mixture is consumed.

The PLIF-PIV images presented in Figure 6-2 and Figure 6-3 provided the information needed to identify the cause of the misfire and partial burn cycle. As shown in chapter 5, for non-diluted cycles with a spark timing of 30^{o} BTDC, misfires and partial burns occurred for a broad range of initial fuel concentration and flow velocities within the 4 mm x 4 mm region ($\overline{\Phi}$ = 0.5 – 1.1; $\overline{V}$ = 2 – 11 m/s). Therefore, it is necessary to reveal the evolution of the fuel distribution and flow field for errant cycles that span this range of mixtures and flow velocities. It is not feasible to show images for every errant and well-burning cycle for this analysis. Instead, images taken for selected misfire and partial burn cycles that span the range of mixtures and flow velocities in the 4 mm x 4 mm region at the onset of spark are presented to reveal the trends common to misfire and partial burn cycles. Figure 6-4 highlights the misfire and partial burn cycles (shown by red circles) for which PLIF-PIV images are presented within this chapter. These highlighted errant cycles span the entire range of equivalence ratio and velocity magnitude values found for the errant cycles.

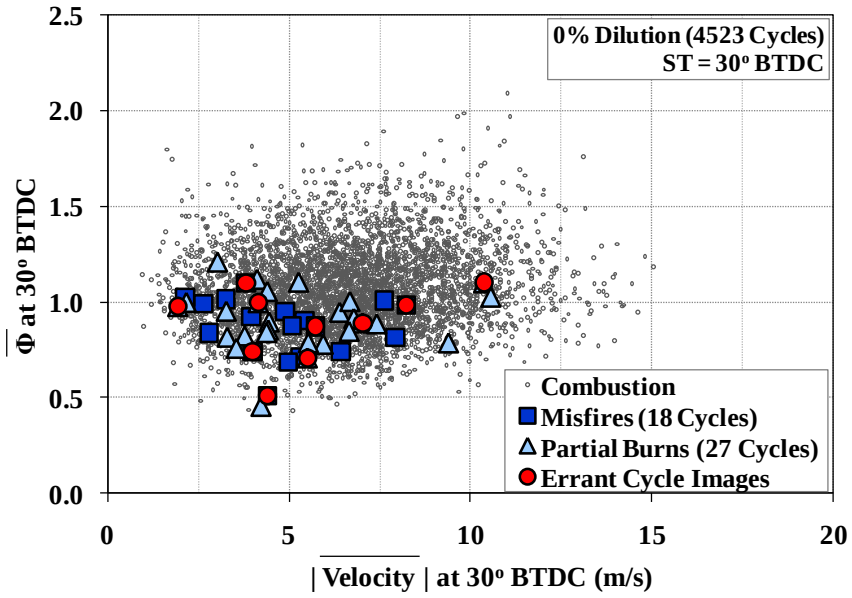

Figure 6-4: The graph of spatially averaged equivalence ratio and velocity magnitude within the 4 mm x 4 mm region at the onset of spark is represented from chapter 5 (figure 5-4 (a)) to highlight the errant cycles (shown by red circles) for which PLIF-PIV images are presented.

Four misfire cycles are presented in Figure 6-5 and are organized by increasing velocity values measured within the 4 mm x 4 mm region at the onset of spark. At the onset of spark (30^o BTDC) each cycle shows distinctly different mixtures and flow velocities near the spark plug ($\overline{\Phi}$ = 0.51 – 1.1; $\overline{V}$ = 3.8 – 8.2 m/s). Despite the different mixtures and velocities near the spark plug at the time of spark, the flame kernel development for each cycle is similar to that shown for the misfire cycle presented in Figure 6-2. A flame kernel is present in each cycle by 26^o BTDC. These flame kernels are small and do not appear until 28^o – 26^o BTDC. More importantly, the flame kernel for each cycle is spatially separated from the flammable mixtures within the viewing plane. The lean mixtures that surround the flame kernel appear to be insufficient to develop the flame kernel into the flammable mixture and the flame kernel size decreases and eventually disappears.

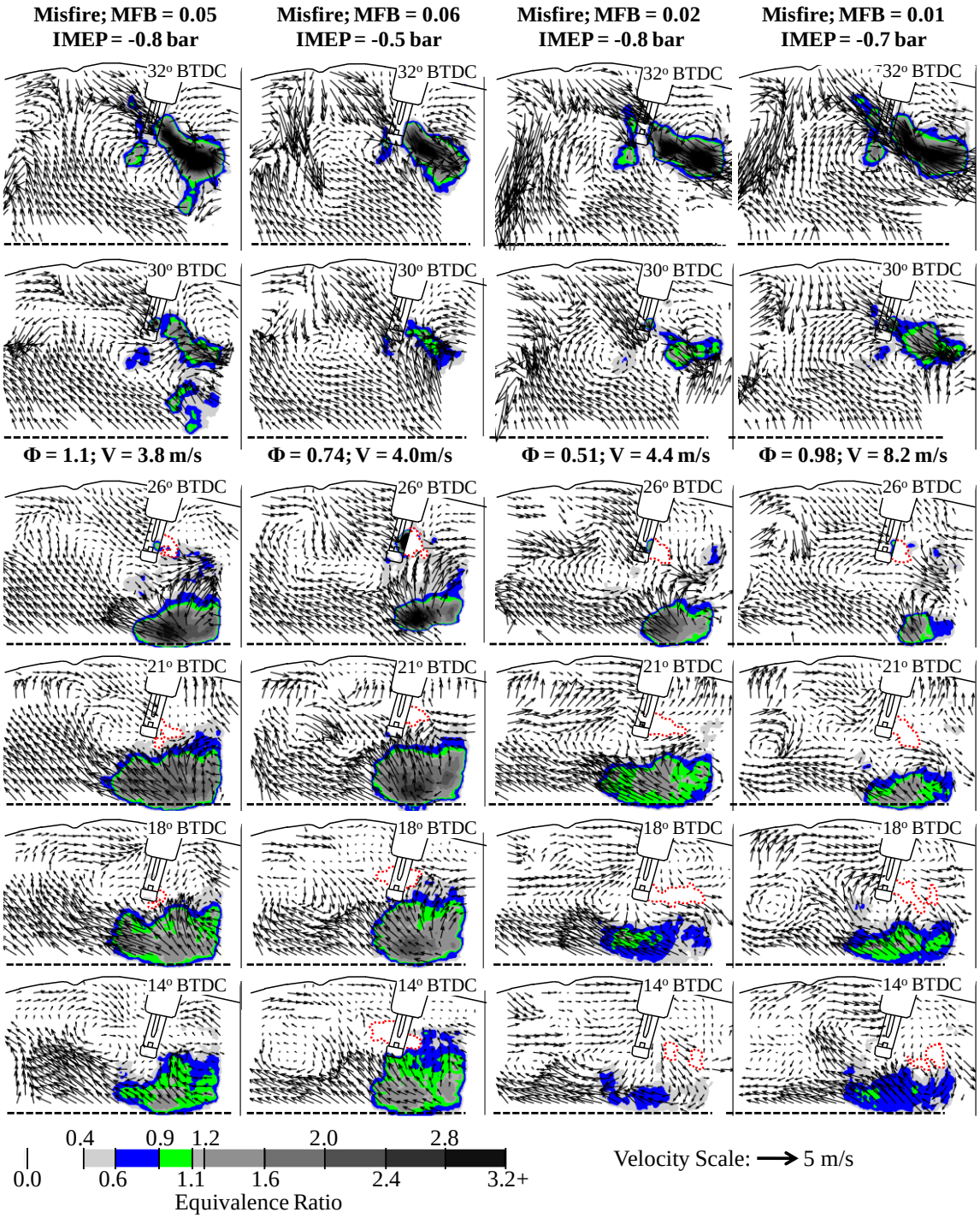

Figure 6-5: Misfire cycles with distinctly different mixtures and flow velocities near the spark plug at the time of spark all show similar trends in flame kernel development. The early flame kernel is small and shows spatial separation from the flammable mixtures within the viewing plane. These mixtures are insufficient to develop the flame kernel into the flammable mixture and the flame kernel decreases in size and eventually disappears. This trend is common among all misfires that occurred within this study.

Figure 6-5 also reveals that the misfire cycles are not limited to cycles that exhibit a small, primarily lean fuel cloud in the piston bowl during the flame kernel development as was shown for the misfire cycle in Figure 6-2. The misfire cycles shown in the first two columns in Figure 6-5 show a large, rich fuel cloud near the bottom right corner of each image at 18^{o} BTDC. This is the fuel that penetrates through the spark gap and collects within the piston bowl. This fuel-air mixture rebounds off the side of the piston bowl (lower right side of the image) and travels towards the spark plug. Despite the flammable mixtures traveling toward the spark plug, there is limited interaction between the flame kernel and the flammable mixture at this time and the flame kernel fails to propagate into the flammable mixture. It is important to stress that the cycles that exhibit a small, primarily lean fuel cloud within the piston bowl have fuel injection pressures, fuel timings, and durations that are consistent with all other cycles. Therefore, the smaller, leaner fuel clouds present within the piston bowl are likely due to a lower amount of fuel that passes through the spark gap and remains within the 2-D viewing plane.

The partial burn cycles for several different of equivalence ratios and velocities within the 4 mm x 4 mm region at the onset of spark ($\overline{\Phi}$ = 0.71 – 1.1; $\overline{V}$ = 1.9 – 10.4 m/s) are presented in Figure 6-6. The cycles are organized in columns for increasing velocity values measured in the 4 mm x 4 mm region at the onset of spark. Despite the different mixtures and velocities near the spark plug at the time of spark, the flame kernel development shown for each cycle is similar to that shown for the partial burn cycle presented in Figure 6-3. Specifically, a flame kernel is formed in all cycles by 26^{o} BTDC, but shows spatial separation from the flammable mixtures within the cylinder. The flame

kernels do not promptly move down into the piston bowl where the bulk of the fuel is located. As a consequence the flame kernel does not contact the flammable mixture until later within the compression stroke when the flammable mixture becomes significantly leaner with time and only a portion of the fuel mixture is consumed.

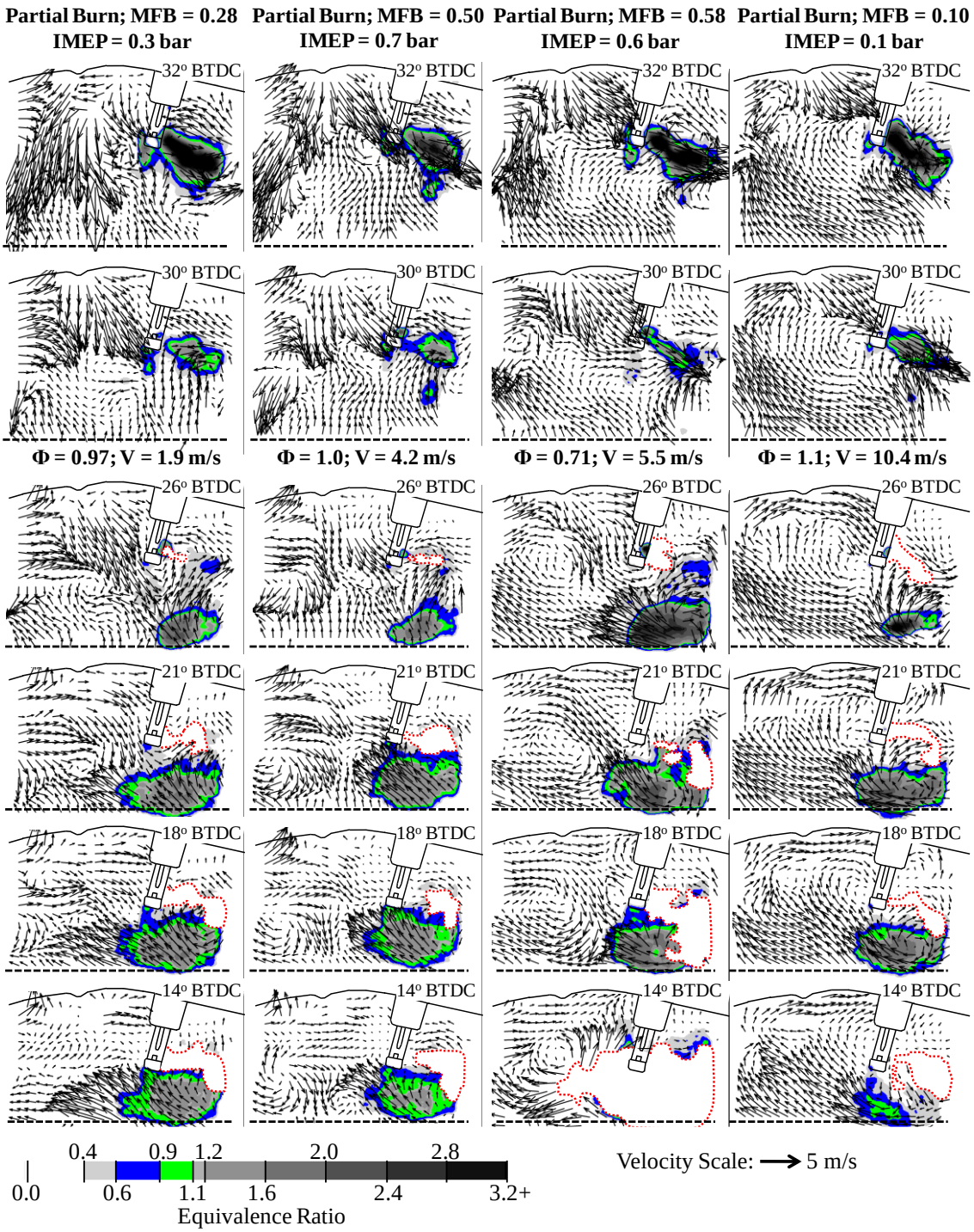

Figure 6-6: Partial burn cycles with distinctly different mixtures and velocities near the spark plug at the time of spark all show similar flame kernel development deficiencies. The flame kernel does not promptly move down into the region of the flammable mixture, but interacts with the flammable mixture at a later time when the mixture is leaner and only a portion of the mixture is consumed. This trend is consistent among all partial burn cycles that occurred in this study.

Ultimately the trends described for the misfire and partial burn cycles shown in the images are consistent with the trends shown for all misfire and partial burn cycles at this operating condition. Namely, a flame kernel is formed for all cycles but fails to develop and interact with the flammable mixture within the piston bowl. For misfire cycles, the flame kernel is surrounded by an overwhelmingly lean mixture that appears to be insufficient to develop the flame kernel and the flame kernel extinguishes shortly after the spark event. For the partial burn cycles, the flame kernel does not promptly move into the piston bowl where the flammable mixture is located and only consumes a portion of the fuel mixture. For the well-burning cycles (only shown in Figure 6-2 and Figure 6-3), the flame kernel grows rapidly and promptly reaches the flammable mixture within the piston bowl.

To quantify these trends for all misfire and partial burn cycles with their corresponding well-burning cycles, the flame areas from these cycles are extracted from the Mie scattering images and plotted for selected crank-angles. The flame kernel areas for these cycles are shown in Figure 6-7. A flame kernel is not observed in some cycles between 29^{o} and 27^{o} BTDC, although more prevalent among misfire and partial burn cycles; this could be due either to out of plane motion or late flame kernel formation. At 26^{o} BTDC a flame kernel is observed for all cycles. Misfire and partial burn cycles are not discriminated from the well-burning cycles until after the spark event (18^{o} BTDC). At this time the well-burning cycles reveal larger flame areas which continue to increase with time. At 14^{o} BTDC, the flame areas for misfire and partial burn cycles begin to decrease and in the extreme case a flame kernel is no longer observed. The results do not discriminate between the partial burns and misfire cycles until 10^{o} BTDC, where the

flame areas for the misfire cycle begin to decrease faster. For all misfires, a flame kernel is established during the spark discharge, failed to grow, and later disappeared.

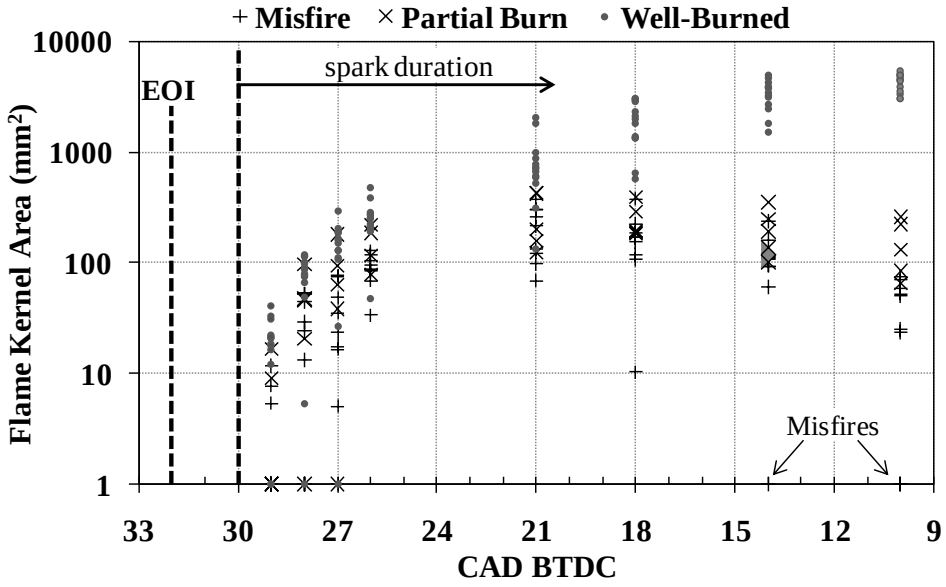

Figure 6-7: The flame area within the 2-D viewing plane is extracted and presented for all misfire and partial burn cycles along with their corresponding well-burning cycles with the similar mixtures and velocities in the 4 mm x 4 mm region at the onset of spark. It is shown that a flame kernel is present for all cycles but fail to fully develop for the misfire and partial burn cycles. Flame areas for the errant cycles decrease after the spark event and in the misfire case are shown to extinguish by 14^{o} BTDC.

It is important to note that the planar measurements presented in this chapter cannot detect the presence of out of plane motion or the fuel distribution and flame kernel development within the third dimension. This information is critical to further assess the flammable paths between the flame kernel and the flammable mixture within the piston bowl. Nonetheless, the important result is that all misfire and partial burn cycles showed the presence of an early kernel, but did not develop as well as the well-burned cycles, and eventually failed to fully burn. These results combined with the results of the electrical

spark discharge parameters suggests that these misfire and partial burn cycles are not ignition failures, but flame development failures.

It appears that with the end-of-injection at 32^{o} BTDC and spark timing of 30^{o} BTDC, the spark event occurs when the spray plume finishes passing through the spark gap and the trailing edge of the flammable mixture is present near the spark plug. If the flame kernel does not sufficiently develop within the first couple crank-angles within the spark event, the flammable mixture travels away faster than the propagating flame front. As a result, the flame kernel does not develop as fast as well-burning cycles and fails to consume the entire mixture within the cylinder.

The above description provides a reasonable explanation for the findings within chapter 5 which reveal that misfire and partial burn cycles at this operating condition primarily occur for cycles that have leaner mixtures and lower velocities ($\overline{\Phi} < 1.1$ and $\overline{V} < 8.0$ m/s) within the 4 mm x 4 mm region at the time of spark than the average well-burning cycle (Figure 5-4 (a) and shown again in Figure 6-4). During the spark duration mixtures near the spark plug become leaner with time which reduces the flame speed [1]. If the flame kernel is not formed quickly the flame kernel experiences leaner mixtures which reduce the flame speed, making it difficult for the flame kernel to reach the flammable mixture as the mixture travels away from the spark plug. As a result the flame kernel does not grow as quickly as other cycles and in the extreme situation the slower flame kernel does not fully consume the available mixture.

It is also necessary to describe the conditions that lead to well-burning cycles. Cycles with $\overline{\Phi} > 1.1$ and $\overline{V} > 8.0$ m/s in the 4 mm x 4 mm region at the onset of spark are predominately well-burning cycles (Figure 5-4 (a) and Figure 6-4). In chapter 3, it was

shown that richer mixtures and higher velocities promote higher available spark energy (despite a large spread in cycle-resolved data in chapter 3 and in Appendix E) which can increase the initial flame kernel size [4]. Also the cycles with higher velocities display significant plasma stretching which exposes the plasma channel to a larger volume of ignitable mixture. These factors help develop an early flame kernel that within the first two CAD of the spark event. As a result the early flame kernel grows more rapidly and remains in contact with a flammable mixture; the flame kernel size then increases and promptly grows into the region where the bulk of the flammable mixture is located and fully consumes the mixture.

6.2.2 Evolution of Shear Strain Rate and Vorticity for Flame Kernel Development

Although a distinct trend was identified between the errant cycles and well-burning cycles from the images showing fuel concentration, flow field, and the flame kernel, it is also advantageous to analyze images of shear strain rate and vorticity on the flame kernel development. The shear strain rate field and vorticity field were overlaid onto the vector field for the errant cycles and their corresponding well-burning cycles. The flame kernel was then overlaid onto these images in the same manner that was done for the PLIF-PIV images. Previous findings have revealed that large positive or negative shear strain rate or vorticity values have the potential to extinguish a flame front [62, 63]. Therefore, it was investigated whether flame kernels for errant cycles were predominately surrounded by abnormally large positive or negative values of shear strain rate and vorticity.

The peak shear strain rate and vorticity values occur from the injection event and quickly decay afterwards. This can be demonstrated in Figure 6-8 which shows the

spatial averaged values of shear strain rate magnitude and vorticity magnitude in the 4 mm x 4 mm region for motored cycles in which fuel was injected but the spark was turned off. This figure presents the evolution of shear strain rate and vorticity values within the 4 mm x 4 mm region throughout the injection event and rest of the compression stroke for 348 cycles. The bars indicate one standard deviation of the 348 measurements. At 30° BTDC, the values are the highest for what would be seen near the spark plug throughout the spark event (30° BTDC – 20° BTDC). Therefore, it can be expected that the flame kernels that are formed earlier will experience larger values of shear strain rate magnitude or vorticity magnitude than flame kernel that are formed later.

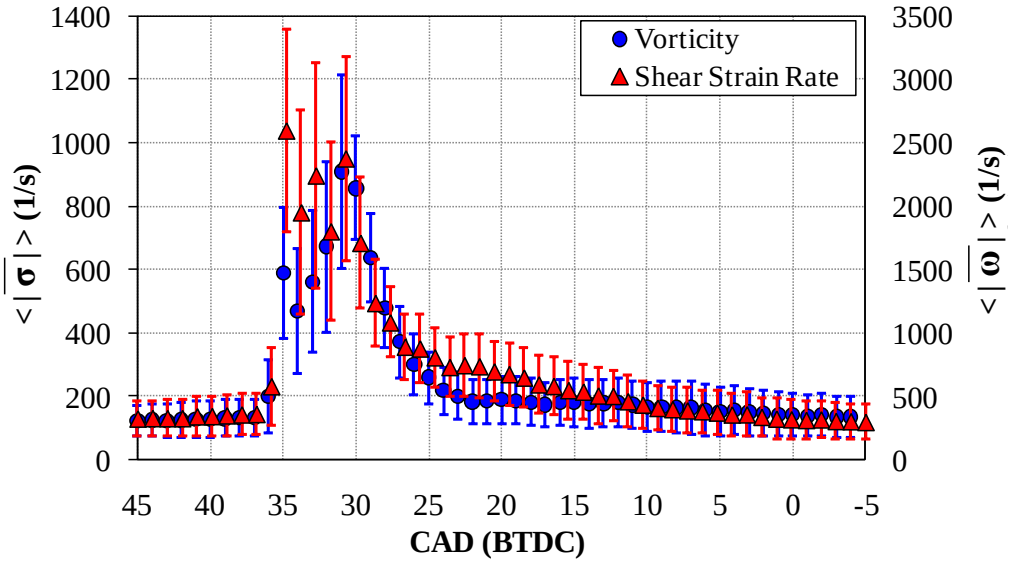

Figure 6-8: Ensemble-spatial averages values of shear strain rate magnitude and vorticity magnitude within the 4 mm x 4 mm region throughout the injection event and rest of the compression stroke for motored operation. Shear strain rate and vorticity are greatest during the injection event and quickly decrease during the spark event. Values during spark timing (30° – 20° BTDC) are greatest at the onset of spark. Bars indicate one standard deviation of the 348 measurements.

Flame kernels for errant cycles experience the same range of nearby shear strain rate and vorticity values (-900 1/s ≤ σ ≤ 900 1/s and -1200 1/s ≤ ω ≤ 1200 1/s,

respectively) as flame kernels for well-burning cycles. Furthermore, errant cycles do not show a distinct trend for which only large magnitudes of shear strain rate or vorticity surround the flame kernel. In addition, flame kernels for well-burning cycles and errant cycles do not show preference to positive or negative shear strain rate or vorticity values that surround the flame kernel. Although these planar measurements cannot detect the flow field surrounding the entire 3-dimenstional flame, a distinct trend between flame kernel development and the nearby shear strain rate or vorticity values is not shown to exist. Therefore, it is concluded that the PLIF-PIV images are more appropriate to explain the differences between the flame kernel development for the well-burning and errant cycles.

6.3 Errant Cycle Analysis for Operation with External N_2 Dilution

The analysis for the misfire and partial burn cycles for operation without external N_2 dilution revealed that a flame kernel was formed for all cycles, but the misfire and partial burn cycles did not develop as quickly as the well-burning cycles. In particular, with an end-of-injection at 32^o BTDC and spark timing of 30^o BTDC, the spark event is initiated when the spray plume finishes passing through the spark gap and the trailing edge of the fuel-air mixture is present near the spark plug. If the flame kernel does not grow substantially when the flammable mixture is present near the spark plug, the flammable mixture travels away faster than the propagating flame front. As a result the flame kernel is surrounded by leaner mixtures within the 2-D viewing plane which appear to be insufficient to fully develop the flame kernel. In the case of a misfire, the flame kernel shows little interaction with the flammable mixture within the viewing plane and the flame kernel eventually disappears. For partial burn cycles, the flame kernel does not

promptly move into the piston bowl where the bulk of the fuel is located. Instead the flame kernel enters the piston bowl when the flammable mixture is leaner and the flame kernel is only able to consume a portion of the mixture.

These trends described above are consistent for the misfire and partial burn cycles that exist for cycles with external dilution. The presence of external dilution (i.e. EGR or N_2) within the unburned mixture substantially reduces the laminar burning velocity [1]. The dilution reduces the heating value per unit mass of the unburned mixture and thus reduces the peak flame temperature and the flame speed. For stratified fuel operation described above, the early flame kernel has limited time to interact with the fuel-air mixture before the flammable mixture departs from the spark plug. As the flame kernel propagates slower due to external dilution, the developing flame kernel will have greater difficulty reaching with the flammable fuel cloud that is traveling away from the spark plug. As a result the occurrence of misfire or partial burn cycles increases with dilution level and the mechanism that produces these errant cycles is the same as what was presented for the non-diluted errant cycles.

This trend can be justified by evaluating the mass fraction burned (MFB) at the dilution levels studied. Figure 6-9 shows the cycle-averaged mass fraction burned curve for each dilution level and spark timing. Each curve is comprised of 348 cycles at each operating condition. The mass fraction burn curve was calculated by normalizing the heat release curve by the averaged total heat release of the 348 cycles. The Rassweiler-Withrow [52] method is used to calculate the heat release from the in-cylinder pressure data.

Operation without dilution and a spark timing of 30^{o} BTDC, the flame propagation is quickest and results in a faster burn. As dilution level increases to 10% and 18% the burn rate decreases due to the slower flame propagation. At higher dilution levels, the misfire rate was too severe with a spark timing of 30^{o} BTDC and the spark timing is advanced to 31^{o} BTDC to provide stable engine performance. The burn curve with the dilution level of 18% and spark timing of 31^{o} BTDC is similar to the burn curve shown for operation with 10% dilution and a spark timing of 30^{o} BTDC. It should be noted however, that the crank-angle relative to top-dead-center is advanced one crank-angle for the data points at the spark timing of 31^{o} BTDC. As the dilution level increases to 26%, the flame propagation is the slowest and results in a slow burning rate which does not reach a value of 100% until 55 CAD after spark.

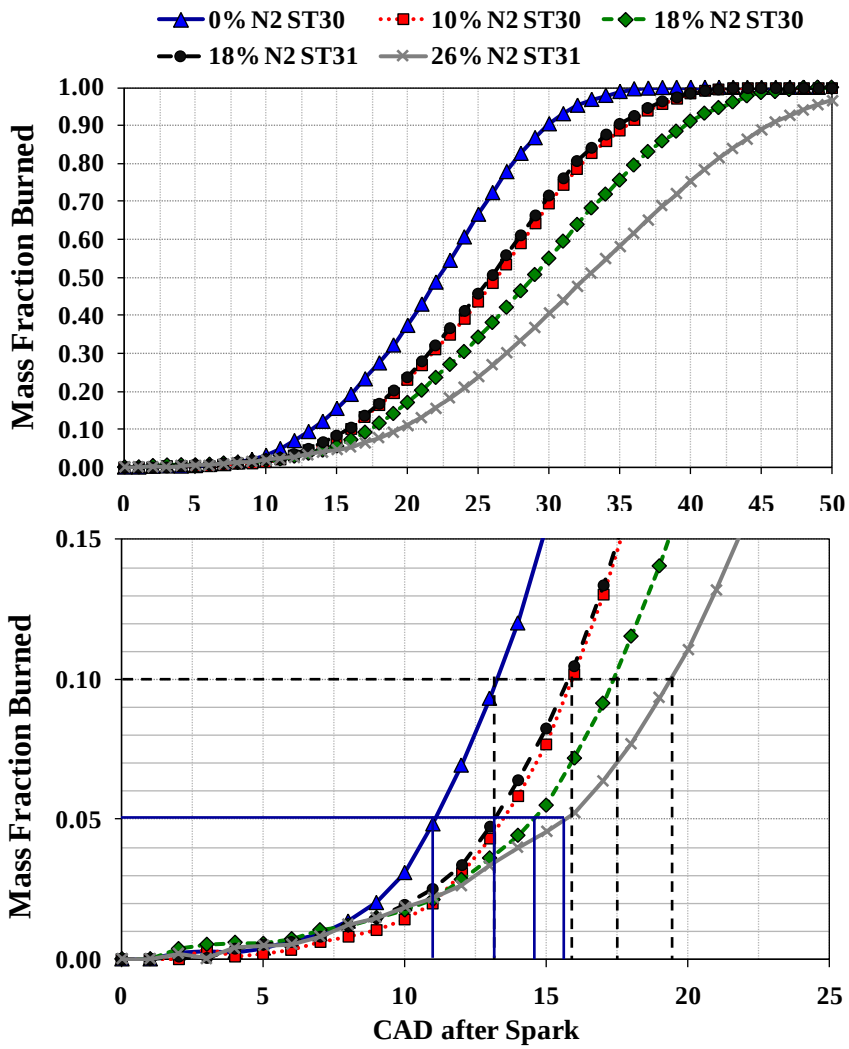

Figure 6-9: Burn rate decreases with increasing dilution level. With slower flame propagation the developing flame kernel will have more difficulty keeping up with the flammable fuel cloud that is traveling away from the spark plug and it is likely that the flame kernel will experience insufficient development. As a result the occurrence of misfire or partial burn cycles increases with dilution level and the mechanism that produces these errant cycles is the same as what was presented for the non-diluted errant cycles.

The CAD location for which 5% and 10% mass fraction burned occurs (MFB 05 and MFB 10 respectively) are highlighted in Figure 6-9 for each dilution level. These parameters are commonly used to describe the initial burn rate. However, the crucial time in which a flame kernel must be initiated when a flammable mixture is near the spark

plug (first few CAD of the spark event) occurs before the location of MFB5. Within the first few CAD of the spark duration, the burn curve does not show a significant burned portion of the mixture and thus is difficult to describe the flame kernel propagation within this time period. A flame kernel exists for errant cycles presented in this study and the mechanism which is found to cause the errant cycles is the same for the range of dilution levels studied. However, more misfire and partial burn cycles occur at the higher dilution levels due to the slower flame propagation which is insufficient to reach the flammable mixture near the spark plug or within the piston bowl.

This analysis is capable to describe the findings within chapter 5 which reveal that misfire and partial burn cycles are less restricted to cycles that exhibit leaner, lower velocity mixtures than the average well-burning cycle (Figure 5-4). For the cycles without dilution, lean mixtures are capable of delaying the early flame kernel propagation which may result in insufficient flame kernel development. Although previous experiments have shown that laminar flame speed is a maximum at $\Phi \sim 1.1$ for isooctane-air mixtures [64], the mass diffusion of the deficient oxygen species can provide progressive flame kernel development. Also since the mixture only becomes leaner during the spark event, previous studies in another SG-SIDI engine have demonstrated that rich mixtures near the spark plug are commonly needed for successful ignition [3, 14, and 65]. However, for cycles with external dilution, the dilution itself is enough to delay flame propagation which can lead to insufficient flame kernel development regardless of a stoichiometric-to-rich mixture near the spark plug at the time of spark. Therefore, it is not uncommon that engine cycles with external dilution and stoichiometric-to-rich mixtures can also experience an abnormally slow flame kernel development which results

in a misfire or partial burn cycle. As dilution level increases, flame kernel development is further delayed and insufficient flame kernel development is more common regardless of the initial mixture and velocity nearby the spark plug at the onset of spark.

6.4 Conclusions

In an attempt to identify the cause of the errant cycles, PLIF and PIV images over the entire field of view (38 mm x 30 mm) were used to analyze the temporal and spatial evolution of fuel concentration and flow field on flame kernel development for misfire, partial burn, and well-burning cycles. Misfire and partial burn cycles were compared to well-burning cycles with similar equivalence ratios and velocity magnitudes within the 4 mm x 4 mm region at the onset of spark. This allowed adequate comparison of errant cycles to well-burning cycles that had similar initial conditions for early flame kernel development.

Simultaneous PLIF and PIV images obtained for non-diluted cycles with a spark timing of 30^{o} were presented to adequately reveal the common trends shown for misfire and partial burn cycles. This operating condition was considered to be the baseline operating condition that provided rare misfire and partial burn cycles without the addition of external dilution. It was revealed that a flame kernel was present for all cycles. For well-burning cycles a flame kernel grew rapidly and promptly moved into the piston bowl and consumed the flammable mixture. For misfire cycles, the flame kernel was primarily surrounded by lean mixtures within the 2-D viewing plane which were apparently insufficient to develop the flame kernel into the location of the flammable mixture and the flame kernel disappeared shortly after the spark event. Partial burn cycles demonstrated that the flame kernel did not promptly move into the piston bowl and was

only able to consume a portion of the mixture. The images emphasize that there is a limited amount of time for which a flammable mixture is available and must be consumed by the developing flame kernel to provide a successfully burning cycle.

The introduction of external dilution ultimately decreased flame speed and the flame kernel is likely to have more difficulty keeping up with the flammable mixture as it travels away from the spark plug. In the extreme cases, this will cause insufficient flame kernel development and the flame kernel will only consume a portion of the mixture at best. As a result the number of misfire and partial burn cycles increased with dilution level, but the mechanism that caused the errant cycle remained the same.

CHAPTER 7

CONCLUSIONS AND FUTURE WORK

7.1 Conclusions

High-speed imaging of fuel concentration and flow velocity along with spark discharge measurements are used in anticipation to identify the cause of misfire and partial burn cycles that occur in a spray-guided spark-ignited direct-injection optical engine under stratified operation.

High-speed particle image velocimetry experiments were first conducted to characterize the available spark energy under well-defined mixture and flow velocity conditions that are typically seen under stratified operation. In particular the available spark energy was obtained for a wide range of homogeneous equivalence ratios (Φ = 0 - 2.9) in a SG-SIDI engine under identical flow conditions. Results reveal a moderate dependence of spark energy on equivalence ratio with average values of spark energy increasing by 21% for the equivalence ratio range from Φ = 0 – 2.3. In a separate investigation, a fuel injector was used as an air injector during motored engine operation to produce injection-like flows near the spark plug in an un-fueled (air only) charge. The air jet velocity was adjusted by varying the injection pressure (0 – 140 bar) and spark energy was characterized for a wide range of velocity values (V = 1 - 10 m/s), shear

strain rate values ($|\sigma|$ = 100 - 1500 1/s), and vorticity values ($|\omega|$ = 100 - 3000 1/s). These measurements were extracted within a 4 mm x 4 mm region downstream the spark plug throughout the spark duration. Flow field and spark energy measurements were correlated for ensemble-averaged data at each air injection pressure and for cycle-resolved data for the entire data set from all air injection pressures. These correlations were presented for averaged flow field values throughout the spark event and the total spark energy as well as crank-angle specific values at the onset of spark. Data interpreted for flow field properties should be interpreted as trends only since the flow measurements were performed such that only in a statistical sense was the plasma contained in the measurement region. Spark energy was shown to increase linearly with velocity at the spark plug which is in agreement with previous findings reported in the literature for low-pressure conditions. In addition, it was observed that increasing shear strain rate also leads to a linear increase in spark energy. A linear increase of spark energy with increasing vorticity was only confirmed with very low correlation. The spread of individual data is much larger than what was observed for influence of velocity and shear strain rate on spark energy. Cycle-resolved data show significantly lower correlations and this arguably reflects that the recorded velocities are not directly measured along the spark plasma channel. It was anticipated that analysis would further couple fuel concentration and flow field properties to spark energy to help explain rare ignition instability events such as misfire.

After the characterization of the spark energy, the engine was operated with late injection, stratified charge operation to identify the engine operating parameters for which misfire and partial burn cycles occurred. With an end-of-injection of 32^{o} BTDC, a

spark timing of 30^{o} BTDC, which was one crank-angle degree off its optimum (31^{o} BTDC), provided near optimum engine performance with the exception of rare misfire and partial burn cycles. Misfire and partial burn cycles were obtained under a range of dilution levels (0%, 10%, 18%, and 26%) at the spark timings of 30^{o} BTDC and 31^{o} BTDC.

High-speed planar laser induced fluorescence of biacetyl and particle image velocimetry techniques were combined to simultaneously measure fuel concentration and flow velocity within the engine. These measurements combined with spark discharge measurements were used in an attempt to identify the cause of misfire and partial burn cycles. Measurements were extracted and analyzed for operating conditions that contained misfire and partial burn cycles; namely a spark timing of 30^{o} BTDC with 0%, 10%, and 18% external dilution levels and a spark timing of 31^{o} with 18% and 26% external dilution levels.

Measurements of spark discharge revealed that misfire and partial burn cycles did not occur for abnormally short or low energy spark events. Furthermore, the spark energy within the first two crank-angle degrees after the onset of spark was greater than the estimated theoretical value of minimum ignition energy at a given equivalence ratio for all cycles. Thus, insufficient spark energy was not found to be the cause of the errant cycles. Measurements of equivalence ratio, velocity magnitude, shear strain rate magnitude, and vorticity magnitude were extracted from the 4 mm x 4 mm region downstream the spark plug at the time of spark to characterize the in-cylinder conditions that occur for errant cycles and well burning cycles. At each operating condition, it was revealed that misfire and partial burn cycles occur within the same general population of

spatially averaged quantities as well-burning cycles. This analysis, while important, did not discriminate between errant and well-burning cycles and was insufficient to identify the cause of the misfire and partial burn cycles.

In an attempt to further identify the cause of misfire and partial burn cycles, the PLIF and PIV images were analyzed over the entire field of view (38 mm x 30 mm) to investigate the temporal and spatial evolution of fuel concentration and flow field on flame kernel development for misfire, partial burn, and well-burning cycles. Misfire and partial burn cycles were compared to well-burning cycles with similar equivalence ratios and velocity magnitudes within the 4 mm x 4 mm region at the onset of spark. This allowed adequate comparison of errant cycles to well-burning cycles that had similar initial conditions for early flame kernel development. The flame kernel was identified as the darkened region in the Mie scattering images where seeding droplets evaporated due to the hot flame gas.

To provide a succinct yet thorough analysis of the misfire and partial burned cycles, simultaneous PLIF and PIV images were presented for non-diluted cycles with the spark timing of 30^{o} BTDC. This operating condition was considered to be the baseline operating condition that provided rare misfire and partial burn cycles without the addition of external dilution. These images adequately revealed the common trends for misfire and partial burn cycles. It was revealed that a flame kernel was present for all cycles. For well-burning cycles an early flame kernel grew rapidly and promptly moved into region of the piston bowl where a rich flammable mixture was located. Subsequent images show rapid expansion of the flame within the 2-D viewing plane and the flame kernel fully consumed the flammable mixture. For misfire cycles, the early flame kernel

was often not present within the viewing until 2-3 crank-angle degrees after the onset of spark and was primarily surrounded by lean mixtures within the 2-D viewing plane. These mixtures appeared to be insufficient to develop the flame kernel into the location of the flammable mixture and the flame kernel disappeared shortly after the spark event. Partial burn cycles demonstrated that the flame kernel did not promptly move into the piston bowl and was only able to consume a portion of the mixture.

The shear strain rate and vorticity values surrounding the flame kernels were analyzed to determine if abnormally large magnitudes of shear strain rate or vorticity were present for the errant cycles which could hinder flame kernel development. The shear strain rate and vorticity values that surround the flame kernel for errant cycles were not restricted to large magnitudes above the average values seen in the 4 mm x 4 mm region during the spark event ($|\bar{\sigma}| > 900$ 1/s and $|\bar{\omega}| >$ 1200 1/s) and were similar to the range of values shown for well-burning cycles. In addition, the flame kernel development for errant and well-burning cycles did not show preference to positive or negative shear strain rate or vorticity values. Since there is not a consistent difference among well-burning and errant cycles, the shear strain rates and vorticities that surround the flame kernel were not considered to be less important than the trends of the of the fuel distribution which was clearly shown to contribute to the insufficient flame kernel development for the errant cycles.

The cycles with external N_2 dilution revealed the exact same trends between errant cycles and well-burning cycles that were shown for the non-diluted cycles, but the occurrence of errant cycles increased. The introduction of external dilution ultimately decreased flame speed and the flame kernel had a greater difficulty keeping up with the

flammable mixture as it travels away from the spark plug. In the extreme case, this caused insufficient flame kernel development and the flame kernel was only able consume a portion of the mixture. As a result the number of misfire and partial burn cycles increased with dilution level, but the mechanism that caused the errant cycle remained the same.

The images of fuel concentration and flow field with the addition of the flame kernel information emphasize that for stratified operation there is a limited amount of time for which a flammable mixture is available and must be consumed by the developing flame kernel to provide a successfully burning cycle. If the flame kernel does not develop sufficiently when a flammable mixture is nearby, the flame kernel will likely experience lean mixtures which are insufficient to develop the flame kernel and the fuel mixture will not entirely be consumed. It is also important to note that the planar measurements presented in this work cannot detect the presence of out of plane motion or the fuel distribution and flame kernel development within the third dimension. This information is critical to further assess the flammable paths between the flame kernel and the flammable mixture within the piston bowl. Nonetheless, the important result is that all misfire and partial burn cycles showed the presence of an early kernel, but did not develop as well as the well-burned cycles, and eventually failed to fully burn.

These results demonstrate the strong coupling between the spray and spark event for the spray-guided concept. Ultimately, a flame kernel must be initiated early during the spark event and grow rapidly to remain in contact with the fuel mixture that travels away from the spark plug. Therefore, it is important to reliably ensure that there is a flammable mixture at the spark plug long enough to initiate a developing flame kernel for all engine

speeds and loads. Variation in fuel injector performance must be further minimized to consistently provide a precise fuel-air mixture to the spark plug during the spark duration for successful flame kernel development. In addition, intake manifold, valves, and combustion chamber design should be optimized to provide a consistent formation of a flammable mixture near the spark plug for stratified charge conditions.

7.2 Future Work

Research beyond the scope of this work must address the concerns of obtaining spatial and temporal measurements of fuel concentration, flow field, and flame kernel development within the third-dimension. While the measurements shown in this work are valuable to diagnose the role of fuel concentration and flow field on flame kernel development for errant cycles and well-burning cycles in a SG-SIDI optical engine, measurements within the z-plane would provide additional information that would successfully identify the cause of the misfire and partial burn cycles under stratified operation. Stereo PIV and LIF volume measurements would be able to help quantify local flow velocity and fuel concentration within the z-plane. Measurements within the tumble plane or a light-sheet setup that provides multiple light-sheets within the tumble plane at various z-plane locations would ultimately provide the information needed within the z-plane. However, multiple light-sheets within the tumble plane would require a camera with a large depth of field than what is used in the current study or a multiple camera setup which would further complicate the already cumbersome optical hardware setup. Analysis from computational fluid dynamic simulations may provide some insight about flame kernel development and fuel concentration that are typically seen within the z-plane. Large-eddy simulations (LES) would provide additional insight beyond the cycle-

averaged simulation of RANS simulations, but computational workload of the LES may be too expensive at this current time for an combustion chamber with such complicated geometries (i.e. pentroof cylinder head and piston bowl configuration).

In addition to the information within the third-dimension it would be viable to utilize a diagnostic technique that accurately describes the spatial information of the flame kernel so that it would be feasible to extract quantitative information of the flame kernel development for all cycles. Fuel concentration, shear strain rate, and vorticity values that surround the developing flame kernel for all cycles will provide further clarification between the differences between misfire, partial burn, and well-burning cycles. CH-LIF or OH-LIF measurements are suitable to clearly identify the spatial information of the flame kernel which could then be manually extracted from the images. The challenge of adding additional lasers and cameras to the already cumbersome optical setup may prevent the feasibility of such measurements.

Further measurements along the spark plasma channel are also needed to accurately measure the flow field and fuel concentration that immediately surround the spark plasma channel. This will help characterize the available spark energy for different flow fields and fuel concentrations seen under stratified operation. This will reduce the large scatter in the data presented in this work and reveal the true dependencies of available spark energy on fuel concentration and flow field information. Spark spectroscopy of the CN* radical to measure equivalence ratio at the spark plug based on the emission intensity of the CN* radical at 388 nm is a viable method to measure fuel concentration along the plasma channel. Stereo PIV with highly resolved spatial resolution would be a suitable method to measure flow velocity along the 3-dimensional

spark plasma channel. However, a post processing procedure would be needed to identify the location of the spark plasma within the 3-dimensional viewing plane and measure the velocity closest to the plasma channel for all cycles.

APPENDIX A

SENSITIVITY OF IN-CYLINDER MEASRUREMENTS DOWNSTREAM OF THE SPARK PLUG

This section addresses the sensitivity of the spatially averaged measurements that are extracted downstream the spark plug. Throughout this investigation, quantities of fuel concentration, velocity magnitude, shear strain rate magnitude ($|\sigma|$), and vorticity magnitude ($|\omega|$) are extracted nearby the spark plug to characterize the in-cylinder conditions near the ignition site. Unfortunately, it is not possible to measure directly along the spark plasma channel. Therefore, the quantities of interest are extracted from a 4 mm x 4 mm region adjacent to and downstream the spark plug. The general region adjacent to and downstream the spark plug is of particular interest since both the intake-induced tumble flow and injection induced flows convect the plasma channel in this direction. The 4 mm x 4 mm region size is selected as it was the minimum size to capture the extent of the spark plasma channel excursions beyond the spark gap.

To analyze the sensitivity of the measurements extracted within the 4 mm x 4 mm region, spatially averaged measurements are extracted from several regions adjacent to and downstream the spark plug which vary in size and location. These spatially averaged quantities are compared to the spatially averaged quantities measured within the 4 mm x

4 mm region. This analysis is performed for the air injection experiments presented in chapter 3 as well as the stratified charge fuel injection experiments presented throughout chapters 4-6.

A-1 Location of Extraction Region

The selected regions for which quantities are extracted from are shown in a Mie scattering image for an instantaneous air injection cycle during the spark event and shown in Figure A-10. A 5 mm x 5 mm region is chosen to compare measurements from a slightly larger region than the 4 mm x 4 mm region. In addition, quantities are extracted from two equally-sided 2.5 mm regions that are contained within the original 4 mm x 4 mm region, but vary in location. One region is located on the left-most side (2.5 x 2.5 Left) of the 4 mm x 4 mm region, while the other region is located on the right-most side (2.5 x 2.5 Right). These regions are selected to evaluate quantities extracted from smaller regions than the 4 mm x 4 mm region which vary in location. Lastly, regions of non-equal size (4 mm x 2 mm and 2 mm x 4 mm), but within the original 4 mm x 4 mm region are chosen to evaluate the sensitivity of the length and width of the extracted region. For the instantaneous Mie scattering image shown in Figure A-10, the spark plasma channel is contained in all regions of interest; however, extent of the plasma channel is more appropriately captured within the 4 mm x 4 mm and 4 mm x 2 mm regions. Even though the 4 mm x 2 mm region appears to capture the majority of the plasma channel in Figure A-10, it should be noted that the spark channel often stretches beyond this region and is suitably captured within the 4 mm x 4 mm region. Therefore, the 4 mm x 4 mm region size is argued as the minimum size to capture the extent of the plasma channel excursions beyond the spark gap.

A region with size smaller than 2 mm is not investigated because this region is smaller than the interrogation window size (2.8 x 2.8 mm^2 for PLIV-PIV experiments). For all experiments the interrogation window is 32 pixels x 32 pixels and with 50% overlap velocity vectors are shown every 16 pixels. For the PLIF-PIV experiments, 16 pixels correspond to a distance of 1.4 mm. Therefore, for a region of 2 mm x 2 mm, only one complete 16 x 16 pixel region is captured which does not provide enough velocity vectors for a statistical interpretation of the flow field.

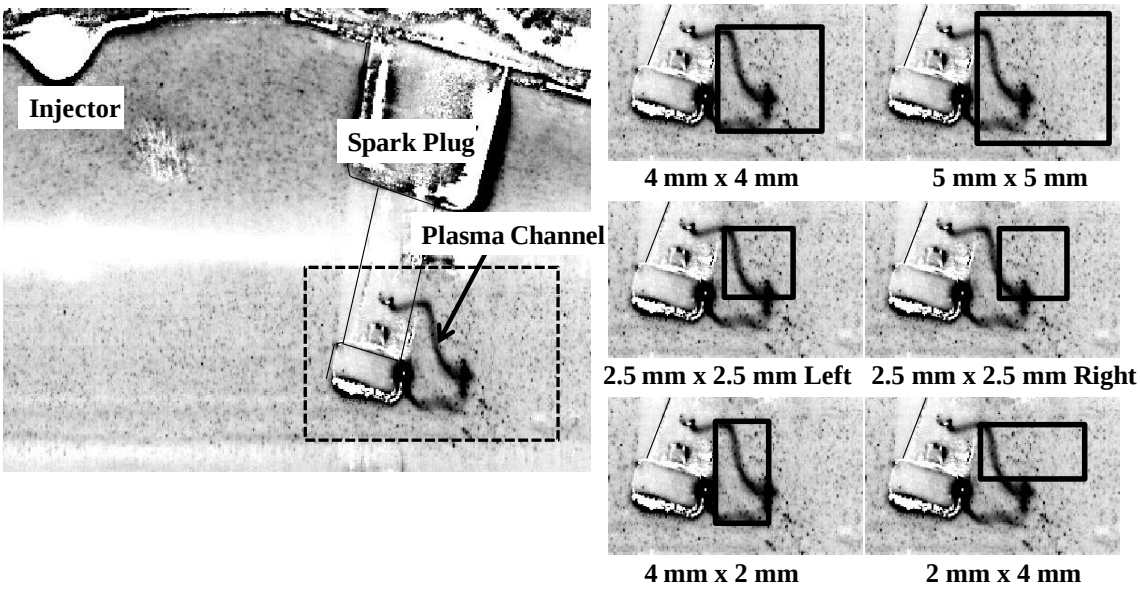

Figure A-10: Regions adjacent to and downstream the spark plug for which spatially averaged quantities of equivalence ratio, velocity magnitude, shear strain rate magnitude, and vorticity magnitude are extracted. These different regions are selected to evaluate the sensitivity of the measurements extracted within the 4 mm x 4 mm region.

A-2 Air Injection Experiments

Quantities of velocity magnitude, shear strain rate magnitude, and vorticity magnitude are extracted from each region shown in Figure A-10 for air injection cycles at the highest injection pressure (140 bar). Figure A-11 shows the ensemble-spatial averaged quantities at each crank-angle for 150 air injection cycles. Bars indicated one

standard deviation of the 150 measurements to demonstrate cyclic variability. For clarity and readability, these bars are only shown for the measurements extracted from the 4 mm x 4 mm region.

Before the air injection, quantities extracted from each region are similar in value for a given variable. During injection, the quantities for each region can show distinct differences, but are within the standard deviation of the measurements within the 4 mm x 4 mm region. Values of velocity magnitude can show up to 20% difference in values, while values of shear strain rate show smaller differences in magnitude below 10%. Values of vorticity show larger differences in magnitude on the order of 30%. During the spark event, the differences between the quantities extracted from each region are smaller than during the injection event and remain within the standard deviation of the measurements extracted from the 4 mm x 4 mm region. This trend remains as the piston moves toward top-dead-center.

During the crank-angle regime shown, there is not a consistent difference between the quantities extracted from the 4 mm x 4 mm region and the quantities extracted from the other regions. In other words, values extracted from a particular region are not consistently higher or lower than the quantities extracted from the 4 mm x 4 mm region. For velocity however, the values shown for the 2.5 mm x 2.5 mm (right) and 2 mm x 4 mm regions are slightly higher than the values extracted from the 4 mm x 4 mm region once air injection event is initiated. This occurs because these regions are more biased toward regions further downstream of the spark plug and not in the immediate location of the wake region behind the spark plug. The velocities seen further downstream the spark plug are greater than the velocities seen within the region directly behind the spark plug.

The 2 mm x 4 mm region is located near the spark plug, but is in the region near the spark gap which experiences higher velocities than the region behind the ground strap. Velocity values within the 4 mm x 4 mm and 5 mm x 5 mm region contain the regions further downstream the spark plug, but also include the location closest to the spark plug where the lower velocity exists. Nonetheless, the velocity values extracted from each region are within the range of cycle-to-cycle variability of the measurements extracted from the 4 mm x 4 mm region. Therefore, the 4 mm x 4 mm region appears to be a suitable choice as captures the full extent of the plasma channel excursions and the measurements downstream the spark plug are more sensitive to the cycle-to-cycle variations than the actual measurements size and location.

It should be noted that velocities during air injection are not always resolved due to the high velocity magnitudes and highly turbulent nature of the flow field. This explains the fact that the velocity magnitude shown in Figure A-11 is the largest at the end of the air injection event when velocity vectors are resolved.

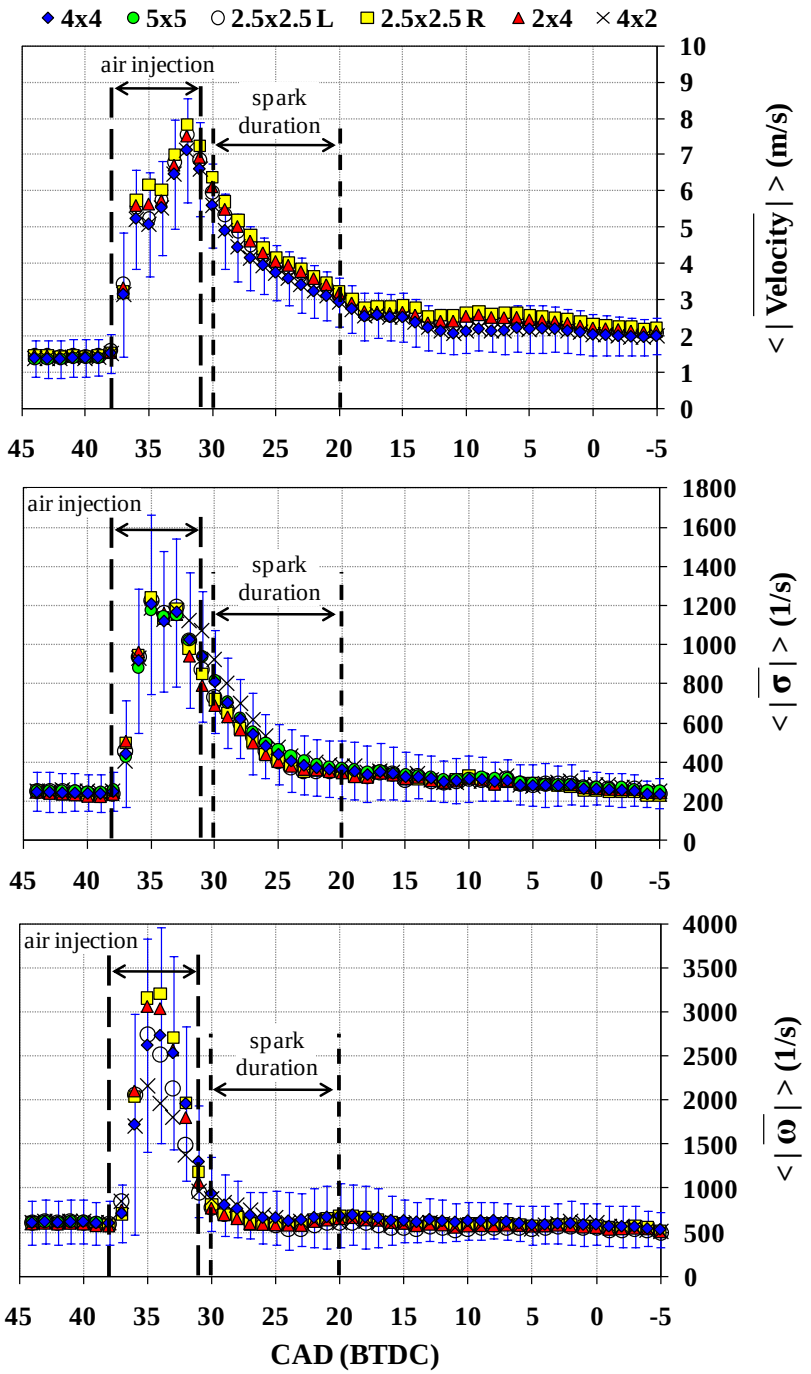

Figure A-11: Crank-angle resolved quantities of velocity magnitude (top), shear strain rate magnitude (middle), and vorticity magnitude (bottom) for regions downstream the spark plug for air injection cycles at the highest injection pressure (140 bar). Values shown are ensemble-spatial averaged values and bars indicate one standard deviation of the 150 measurements within the 4 mm x 4 mm region. Quantities extracted from each region are agreeable within the cycle-to-cycle variation of the measurements extracted from the 4 mm x 4 mm region.

In most situations, quantities are extracted at the crank-angle degree of the onset of spark to characterize the initial conditions closest to the spark plug. To highlight the quantities at this time, Figure A-12 reveals the quantities of velocity magnitude, shear strain rate magnitude, and vorticity magnitude that are extracted from each region at the onset of spark (30^{o} BTDC). The values shown are ensemble-spatial averaged values of 150 cycles and the bars indicate one standard deviation of the measurements for each region to demonstrate the cyclic variability. Quantities extracted from all regions are agreeable within the cycle-to-cycle variability. Thus, for the air injection experiments, the spatially averaged measurements within the 4 mm x 4 mm region are more sensitive to cycle-to-cycle variation than to the slight differences in extraction region size and location. This information confirms the validity of the selected 4 mm x 4 mm region.

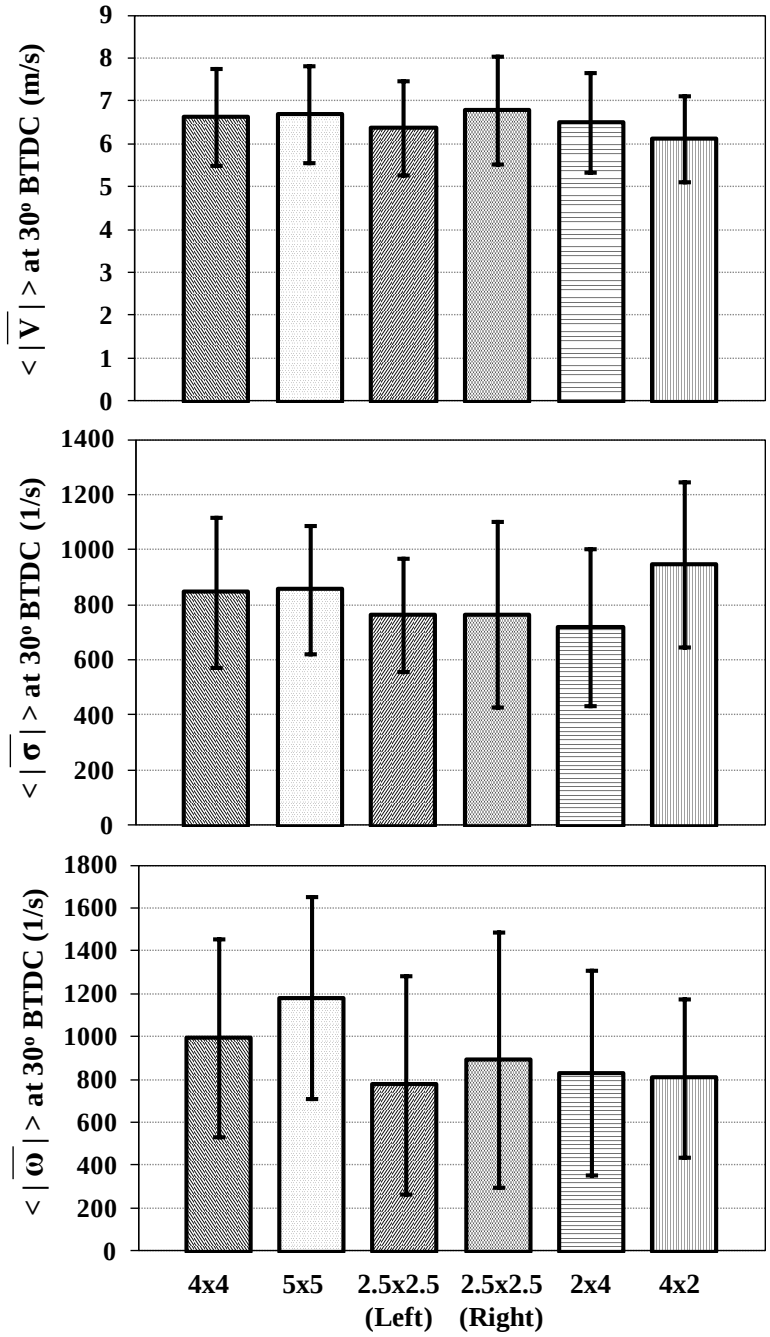

Figure A-12: Ensemble-spatial averaged values of velocity magnitude (top), shear strain rate magnitude (middle), and vorticity magnitude (bottom) for each extraction region at the onset of spark (30^o BTDC) for air injection cycles at the highest injection pressure (140 bar). Quantities are shown to be within the cycle-to-cycle variability of the measurements and further confirm the validity of the selected 4 mm x 4 mm region. Bars indicate one standard deviation of the 150 measurements.

A-3 Stratified Charge Fuel Injection Experiments

Quantities of equivalence ratio, velocity magnitude, shear strain rate magnitude, and vorticity magnitude are extracted from each region downstream the spark plug for 348 motored fuel- injection cycles (no spark). Ensemble-spatial averaged values of equivalence ratio and velocity magnitude at each crank-angle are shown in Figure A-13, while ensemble-spatial averaged values of shear strain rate magnitude and vorticity magnitude at each crank-angle are shown in Figure A-14. Bars indicate one standard deviation of the 348 measurements for the quantities extracted from the 4 mm x 4 mm region to demonstrate cyclic variability. For clarity and readability, these bars are only shown for the measurements associated with the 4 mm x 4 mm region. Although the spark was not activated, the onset of spark and expected spark duration are shown within Figure A-13 and Figure A-14 to emphasize the values during this particular timing.

During fuel injection, quantities of equivalence ratio extracted from each region are drastically different from one another and beyond the limits of the cycle-to-cycle variation. At this time there is significant liquid fuel present downstream the spark plug with large cycle-to-cycle variability. Fluorescence signal strength of liquid biacetyl has not yet been characterized for engine conditions. Therefore, the normalization procedure used for late injection images in the presence of liquid biacetyl might not completely render results quantitative as the case for fully vaporized conditions. After the injection event, equivalence ratio dramatically decreases and fortunately values extracted from the different regions are in agreement within the cyclic variability associated with the 4 mm x 4 mm region.

Velocity values extracted from the different regions are similar (1-2 m/s) before the injection event. During fuel injection ensemble-spatial velocity values are distinctly

different for the different regions, but are within the cyclic variability of the measurements within the 4 mm x 4 mm region. After the injection event, velocity values slowly decay and remain within the cyclic-variability of the measurements within the 4 mm x 4 mm region. After the typical spark duration, velocity values for all regions are in agreement within the cyclic variability and are similar to values typically seen before the injection event (~ 2 m/s).

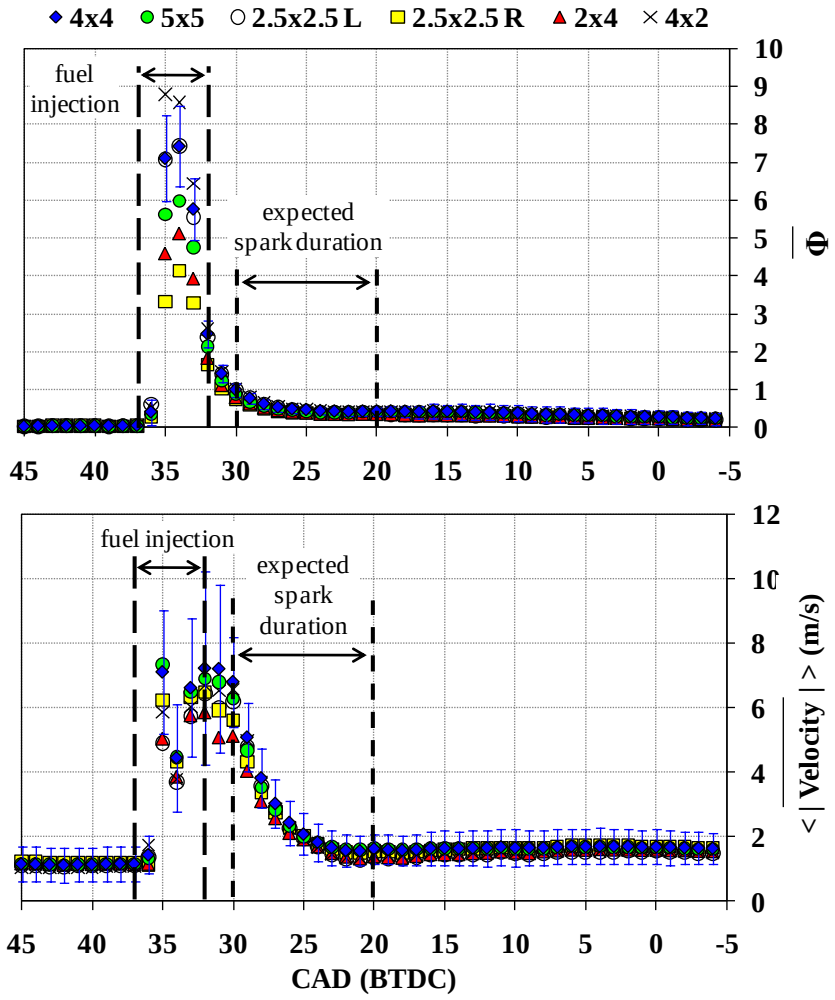

Figure A-13: Crank-angle resolved quantities of equivalence ratio (top) and velocity magnitude (bottom) for each region downstream the spark plug for motored fuel injection cycles. Values shown are ensemble-spatial averages and bars indicate one standard deviation of the 348 measurements within the 4 mm x 4 mm region. After the injection event, the quantities extracted from the different regions are agreeable within cyclic variability.

Values of shear strain rate and vorticity extracted from the different regions show a common trend amongst each other. Before fuel injection, values extracted from each region downstream the spark plug are similar for each variable ($|\bar{\sigma}|$ = 100 - 200 s^{-1}, $|\bar{\omega}|$ = 200 – 500 s^{-1}). During fuel injection values show a drastic increase and can be distinctly different for each extraction region, but are within the cyclic variability of the measurements for the 4 mm x 4 mm region. After the injection event, values of shear strain rate and vorticity decrease and values extracted from each region are in agreement within cyclic variability of the measurements for the 4 mm x 4 mm region.

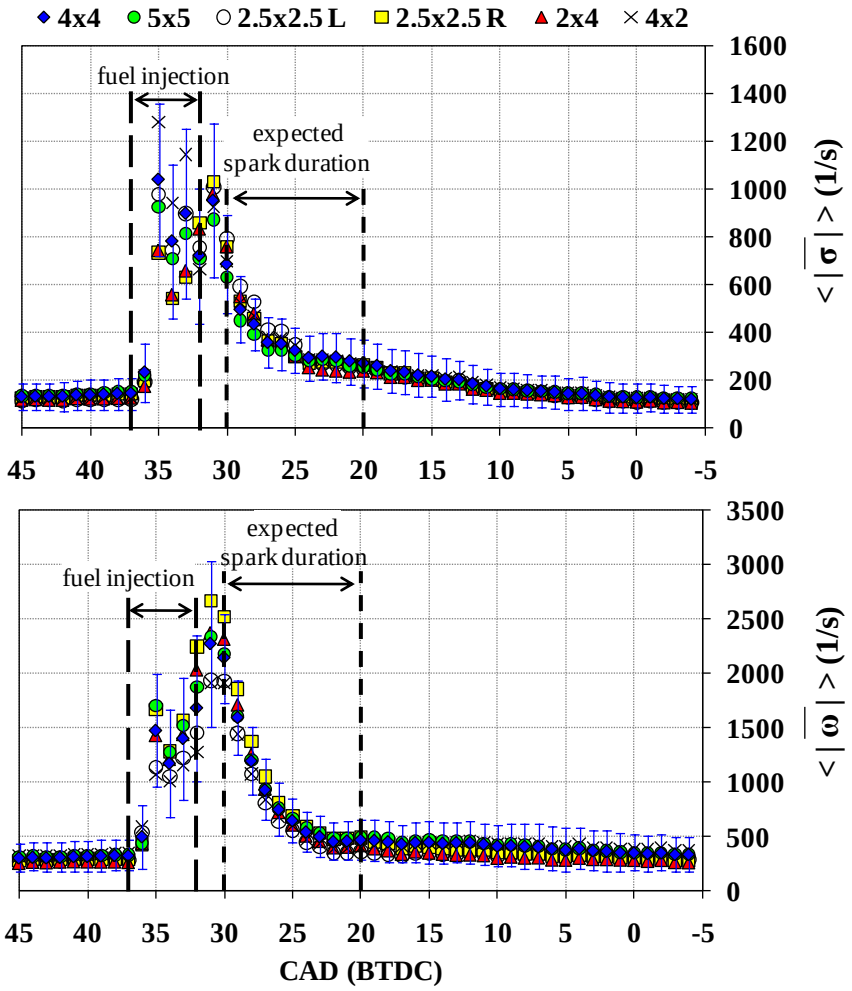

Figure A-14: Crank-angle resolved quantities of shear strain rate magnitude (top) and vorticity magnitude (bottom) for each region downstream the spark plug for motored fuel injection cycles. Values shown are ensemble-spatial averages and bars indicate one standard deviation of the 348 measurements within the 4 mm x 4 mm region. Values extracted from each region are in agreement within the cyclic variability of the 4 mm x 4 mm measurements.

Figure A-15 highlights the ensemble-spatial averaged quantities of equivalence ratio, velocity magnitude, shear strain rate magnitude, and vorticity magnitude at 30^{o} BTDC (expected onset of spark) extracted from each region downstream the spark plug. Bars indicate one standard deviation of the 348 measurements to demonstrate the cyclic variability. Although ensemble-spatial averaged quantities are be different at 30^{o} BTDC all quantities are agreeable within the cyclic variation. Thus, the spatially averaged measurements within the 4 mm x 4 mm region are more sensitive to cycle-to-cycle

variations than the difference in extraction region size and location. This information confirms the validity of the selected 4 mm x 4 mm region for which quantities are extracted.

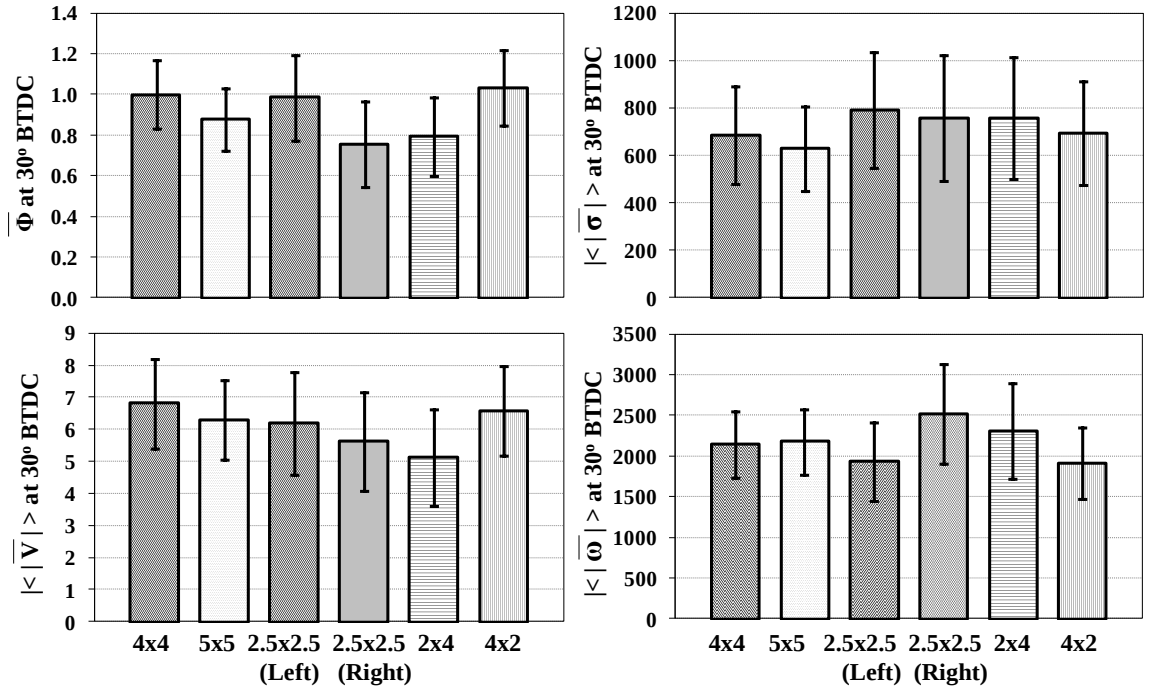

Figure A-15: Ensemble-spatial averaged values of equivalence ratio (top-left), velocity magnitude (bottom-left), shear strain rate magnitude (top-right), and vorticity magnitude (bottom-right) for each extraction region at 30^o BTDC for motored fuel injection cycles. Quantities are shown to be within the cycle-to-cycle variability of the measurements and further confirm the validity of the selected 4 mm x 4 mm region. Bars indicate one standard deviation of the 150 measurements.

APPENDIX B

AFFIRMATION OF THREE-DIMENSIONAL FLOW FIELD WITHIN THE ENGINE

Engine flows in general are 3-dimensional and out of plane motion, while present, is not quantified within the planar flow field images presented in this work. Therefore, analysis is performed to confirm that the flow field shown in the planar images is in-fact 3-dimensional. The fact that the flow field is 3-dimensional does not take away from the important information obtained from the planar measurements.

The continuity equation:

$$-\frac{1}{\rho}\frac{\partial \rho}{\partial t} = \frac{\partial u}{\partial x} + \frac{\partial v}{\partial y} + \frac{\partial w}{\partial z} \qquad \text{(B-1)}$$

is used with the assumption that density is spatially uniform and effects such as mass loss past the piston rings can be neglected. Solving for the $\partial w/\partial z$ term within (B-1) gives:

$$\frac{\partial w}{\partial z} = -\left(\frac{1}{\rho}\frac{\partial \rho}{\partial t} + \frac{\partial u}{\partial x} + \frac{\partial v}{\partial y} \right) \qquad \text{(B-2)}$$

and provides an estimate of the normal strain in the third-dimension. For a true 2-dimensional flow, the $\partial w/\partial z$ term equals zero. This should not be confused with the fact

that a value of $\partial w/\partial z = 0$ implies that the flow is 2-dimensional. The terms on the right hand side of (B-2) are computed to provide an estimate of $\partial w/\partial z$ and quantitatively demonstrate the flow is 3-dimensional. It is important to note that this analysis only provides an estimate of the normal strain rate in the third-dimension and does not provide quantitative analysis of the out of plane velocity component.

The rate of change of the density is calculated by evaluating the change of density at each crank-angle:

$$\frac{1}{\rho}\frac{\partial \rho}{\partial t} = \frac{1}{\Delta t}\frac{\rho_t - \rho_{t-1}}{\rho_t} \tag{B-3}$$

The density at each crank-angle is calculated from the trapped cylinder mass and volume at each crank-angle. The trapped mass within the cylinder is computed at intake valve closing (IVC) via the ideal gas law. The pressure and temperature at IVC is assumed to be the same as the intake pressure and temperature.

The x- and y- velocity derivative terms in (B-1) and (B-2) represent the normal strain rate components:

$$\frac{\partial u}{\partial x} = e_{xx} \quad \text{and} \quad \frac{\partial v}{\partial y} = e_{yy} \tag{B-4}$$

The normal strain rates (e_{xx} and e_{yy}) are computed within the 2-D viewing plane. These measurements are extracted from the 4 mm x 4 mm region (Figure B-1) throughout the time of imaging (45^o BTDC – 5^o ATDC). This analysis is conducted for instantaneous flow fields for motored cycles (no injection), air injection cycles, and motored fuel injection cycles (fuel injection, but no spark). Table B-3 provides the engine operating parameters for the experiments with the different injection strategies.

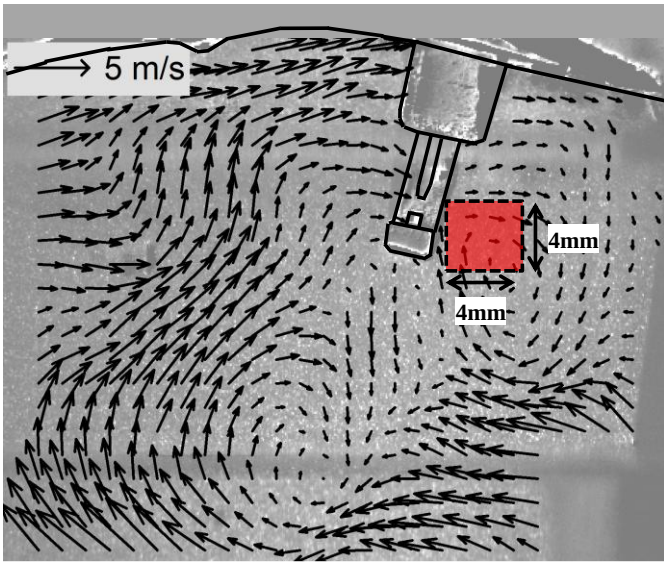

Figure B-1: The normal strain rate components (e_{11} and e_{22}) were extracted from the 4 mm x 4 mm region downstream the spark plug for motored cycles, air injection cycles, and motored fuel injection cycles.

Parameters	Motored (no injection)	Air Injection	Motored Fuel Injection
Engine Speed	800 RPM		
Manifold Absolute Pressure (MAP)	95 kPa		
Spark Timing	30 BTDC		
Injection Timing (Physical EOI)	-	31° BTDC	32° BTDC
Injection duration	-	1.5 ms	1.14 ms
Injection Pressure	-	110 bar	
Intake temperature	45° C		
Oil and Coolant temperature	90° C		
PIV time delay	62.5 μs	20 μs	

Table B-3: Operating parameters for the air injection, fuel injection, and motored experiments for which normal strain rates are evaluated.

Figure B-2 shows the crank-angle resolved quantities of $\partial u/\partial x + \partial v/\partial y$ and $\rho^{-1}\partial\rho/\partial t$ for motored cycles, air injection cycles, and motored fuel injection cycles. Values of $\partial u/\partial x + \partial v/\partial y$ are ensemble-averaged values from 300 cycles at each injection operation. Bars indicate one standard deviation of the 300 measurements at each injection

operation. Only one value of $\rho^{-1}\partial\rho/\partial t$ is computed at each crank-angle since values of trapped mass and volume are calculated for the averaged cycle. The $\partial w/\partial z$ term is also shown in Figure B-2 and is calculated from the ensemble-averaged measurements of $\partial u/\partial x + \partial v/\partial y$ and $\rho^{-1}\partial\rho/\partial t$.

For motored cycles, for which the flow field is moderate (|V| < 5 m/s), the $\rho^{-1}\partial\rho/\partial t$ term is within the range of $\partial u/\partial x + \partial v/\partial y$ values. However, the resulting $\partial w/\partial z$ term is not equal to zero for each crank-angle which indicates that the flow on average is 3-dimensional.

For air injection cycles, values of $\partial u/\partial x + \partial v/\partial y$ increase dramatically from the air injection event and show large cycle-to-cycle variation. The resulting magnitude of the out of plane normal strain rate, $\partial w/\partial z$, is shown to be comparable to the sum of the in-plane normal strain rates, $\partial u/\partial x + \partial v/\partial y$. From this analysis it is obvious that the flow is 3-dimensional. Values of each term before air injection and well after air injection (5^{o} BTDC) are comparable to what is seen for motored operation and still indicate that the flow is 3-dimensional.

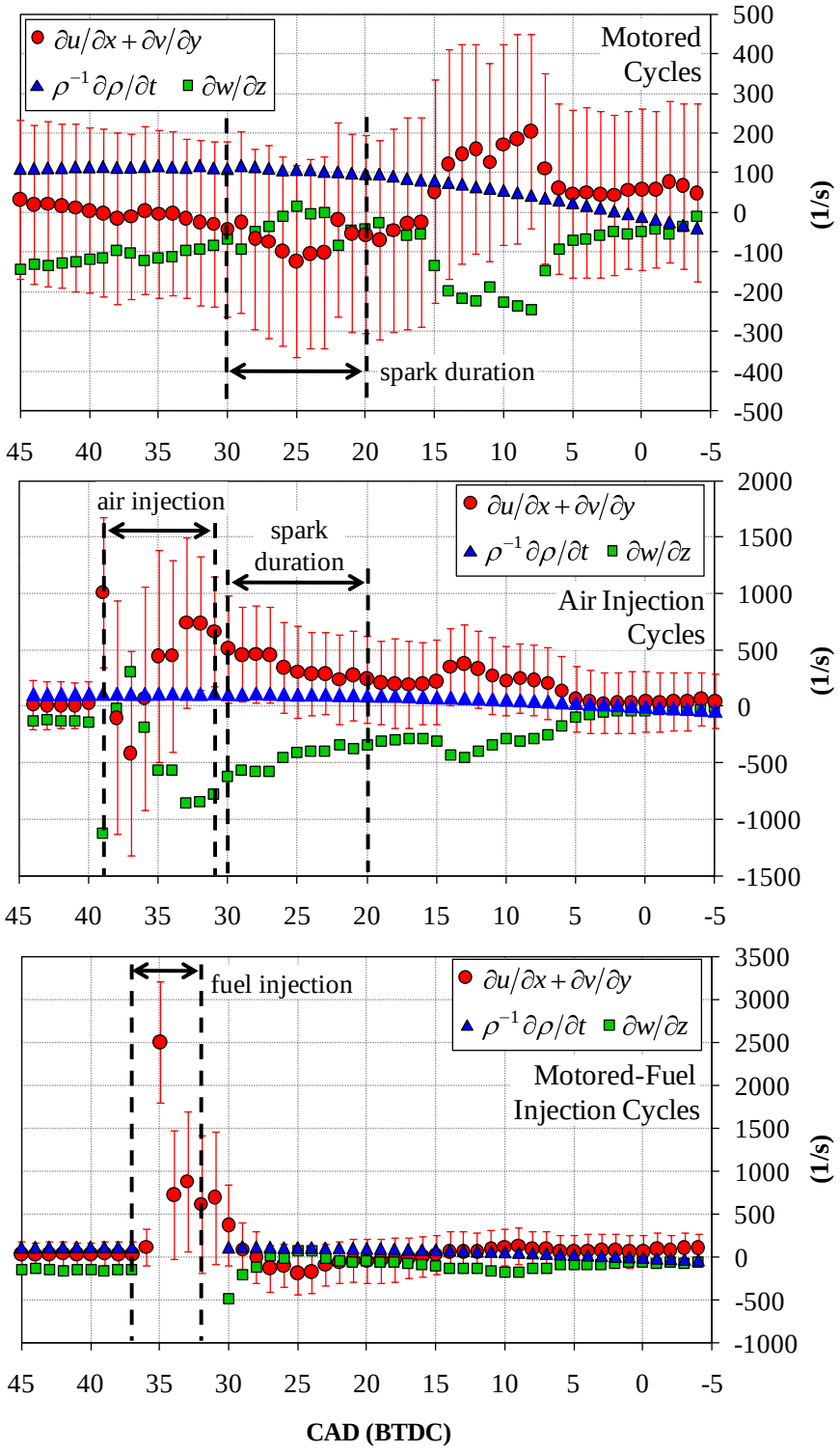

Figure B-2: Values of $\partial w/\partial z$ are calculated from ensemble-averaged values of $\partial u/\partial x + \partial v/\partial y$ and $\rho^{-1}\partial\rho/\partial t$. These values demonstrate that the flow within the engine is 3-dimensional throughout the time of imaging.

For motored fuel injection cycles, values of the in-plane normal strain rates, $\partial u/\partial x + \partial v/\partial y$, increase dramatically during fuel injection and show large cycle-to-cycle variation. Values of $\rho^{-1}\partial\rho/\partial t$ are not computed during fuel injection because liquid fuel is present within the 4 mm x 4 mm region at this time and the density within this region cannot be quantified. Therefore quantities of $\partial w/\partial z$ are not computed during the injection event. After the injection event values of $\rho^{-1}\partial\rho/\partial t$ are computed for air-only charges despite the fact the fuel-air mixture is present within the 4 mm x 4 mm region. After the fuel injection event, the values of $\partial w/\partial z$ are comparable to $\partial u/\partial x + \partial v/\partial y$ and though values are smaller than during the injection event, these values indicate that the flow is 3-dimensional.

The $\rho^{-1}\partial\rho/\partial t$ term is calculated for a range of equivalence ratios and compared to the values obtained for an air-only charge to validate the values of $\rho^{-1}\partial\rho/\partial t$ that are presented in Figure B-2. It is first necessary to determine the range of equivalence ratio values seen within the 4 mm x 4 mm region after the injection event. Figure B-3 reveals the ensemble-averaged values of equivalence ratio for the 300 motored fuel injection cycles. After 30^{o} BTDC liquid fuel is not present within the 4 mm x 4 mm region and equivalence ratios are within the range of $0.0 \leq \overline{\Phi} \leq 1.0$. Therefore, the $\rho^{-1}\partial\rho/\partial t$ term is calculated for mixtures $0.0 \leq \Phi \leq 1.0$. In this analysis the density is calculated for homogeneous mixtures despite the fact that the fuel-air mixture is heterogeneous directly after the injection event. However, well after the injection event (i.e. 15^{o} BTDC), the fuel and air have had adequate time to mix and the mixture within the 4 mm x 4 mm region can be presumed quasi-homogenous. As fuel concentration increases from $\Phi = 0.0$ to $\Phi = 1.0$, the density increases by 4%. Values of $\rho^{-1}\partial\rho/\partial t$ for mixtures with $\Phi = 1.0$ are within

2% of values calculated for an air-only charge. Therefore, the air-only values to compute the $\rho^{-1}\partial\rho/\partial t$ term are suitable for analysis with fuel injection.

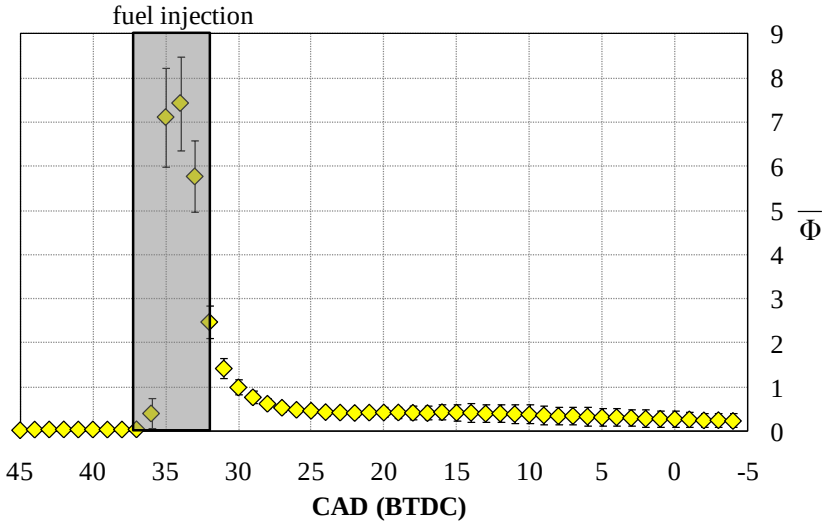

Figure B-3: Spatial averages of equivalence ratio in the 4 mm x 4 mm region for cycles with motored fuel injection. Equivalence ratio within the 4 mm x 4 mm region is within the range of $0.0 \leq \Phi \leq 1.0$ after the injection event. Bars indicate one standard deviation of the 300 measurements.

It should be noted that most optical engines suffer from mass loss. The engine used in this work has been shown to have mass loss on the order of 10% throughout the compression stroke [66]. This effect would ultimately lower the value of the $\rho^{-1}\partial\rho/\partial t$ term presented within this study. Nonetheless, the flow would still be shown to be 3-dimensional.

The fact that the flow within the engine is 3-dimensional can be attributed to several factors within the engine. Swirl motion is a common factor that will cause out of plane motion. For the current study, the field of view is within the tumble plane and there is a swirl flow ratio of 0.8 which is induced by the intake manifold configuration. This can contribute to the out of plane motion within selected region. In addition, the 4 mm x 4 mm region is within wake region of the spark plug. The tumble induced flow produces

a clockwise motion of the flow field within the cylinder as illustrated in Figure B-1. The spark plug can disrupt this motion and produce a wake region of the flow field downstream of the spark plug.

The fact that the flow within the engine is 3-dimensional does not take away from the important observations obtained from the planar velocity measurements revealed within this study.

APPENDIX C

CORRELATIONS FOR CRANK-ANGLE RESOLVED SPARK ENERGY AND FLOW PROPERTIES

In Chapter 3, flow properties are extracted from a 4 mm x 4 mm region adjacent to and downstream the spark plug to investigate relationships between available spark energy and flow properties. An air injector is used to produce injection-like flows near the spark plug for an air-only charge (no fuel). The injection pressure is used to control the flow velocity near the spark plug. Correlations are presented for integrated quantities throughout the spark duration as well as time-specific quantities at the onset of spark (30^{o} BTDC). Weaker correlations are shown to exist for time-specific quantities at the onset of spark than for quantities integrated throughout the spark duration. These weaker correlations are a result of the inability to measure the flow properties directly along the spark plasma channel. At the onset of spark, the plasma channel has not had sufficient time to stretch into the 4 mm x 4 mm region. Instead the plasma channel is primarily located between the spark electrodes and quantities within the 4 mm x 4 mm region do not depict the values seen along the plasma channel.

Figure C-4 presents the R^2 values of linear correlations for time-specific spark discharge and flow data for the first four crank-angle degrees of spark timing to demonstrate the correlations between time-specific spark and flow data as the plasma

channel is convected into the 4 mm x 4 mm region. Data is presented for ensemble-averaged quantities over the 300 cycles at each injection pressure and for cycle-resolved quantities for all injection pressures.

For ensemble-averaged quantities, the R^2 values for velocity increase from $R^2 = 0.44$ to $R^2 = 0.88$ throughout the first four crank-angles of the spark duration. Cycle resolved data shows a similar increasing trend but significantly lower R^2 values ($R^2 = 0.08 – 0.28$). The correlation between spark energy and velocity magnitude does however becomes weaker at 27^o BTDC for the cycle-resolved data. A possible explanation for this decrease is the likelihood that the plasma channel is not within the 4 mm x 4 mm region at this time for all cycles. Either out of plane motion or a restriking plasma channel (see section 3.5 for description) will remove the plasma channel from the 4 mm x 4 mm region which can lower the correlation between spark energy and velocity magnitude.

A good correlation already exists at the onset of spark (30^o BTDC) for the relationship between ensemble-averaged values of spark energy and shear strain rate magnitude ($R^2 = 0.87$). The R^2 value increases to $R^2 = 0.99$ one crank-angle degree later (29^o BTDC) and values remains above $R^2 = 0.96$ throughout the crank-angle regime shown. For cycle resolved data, R^2 values are significantly lower ($R^2 = 0.09 – 0.19$) and do not continue to increase with crank-angle. The R^2 value increases from $R^2 = 0.09$ to $R^2 = 0.19$ within the first two crank-angle degrees of the spark, but then continues to decrease to $R^2 = 0.10$ at 27^o BTDC. The possibility that the plasma channel is not within the extraction region is a likely possibility of the decreasing R^2 value.

For correlations of spark energy and vorticity magnitude, the R^2 value for ensemble-averaged measurements is shown to decrease throughout the first four crank-

angles of the spark duration. For cycle resolved measurements, the R^2 value increases slightly at 29^o BTDC, but then continues to decrease. Overall, the R^2 values for the correlations between spark energy and vorticity magnitude are lower than R^2 values associated with velocity magnitude and shear strain rate magnitude. These correlations along with the correlations presented in Chapter 3 would suggest that spark energy is not well correlated with vorticity magnitude. However, further measurements that are capable of resolving the flow field along the 3-dimensional plasma channel are needed to confirm this claim.

Overall, weaker correlations exist for cycle resolved measurements than ensemble-averaged measurements. The spark discharge behavior and flow conditions in an operating engine are highly stochastic and large cycle-to-cycle variation exists in these measurements. As a result, the spread in the data is large and weak correlations exist for the data. For ensemble-averaged measurements, the cycle-to-cycle variation is mitigated which yields stronger correlations.

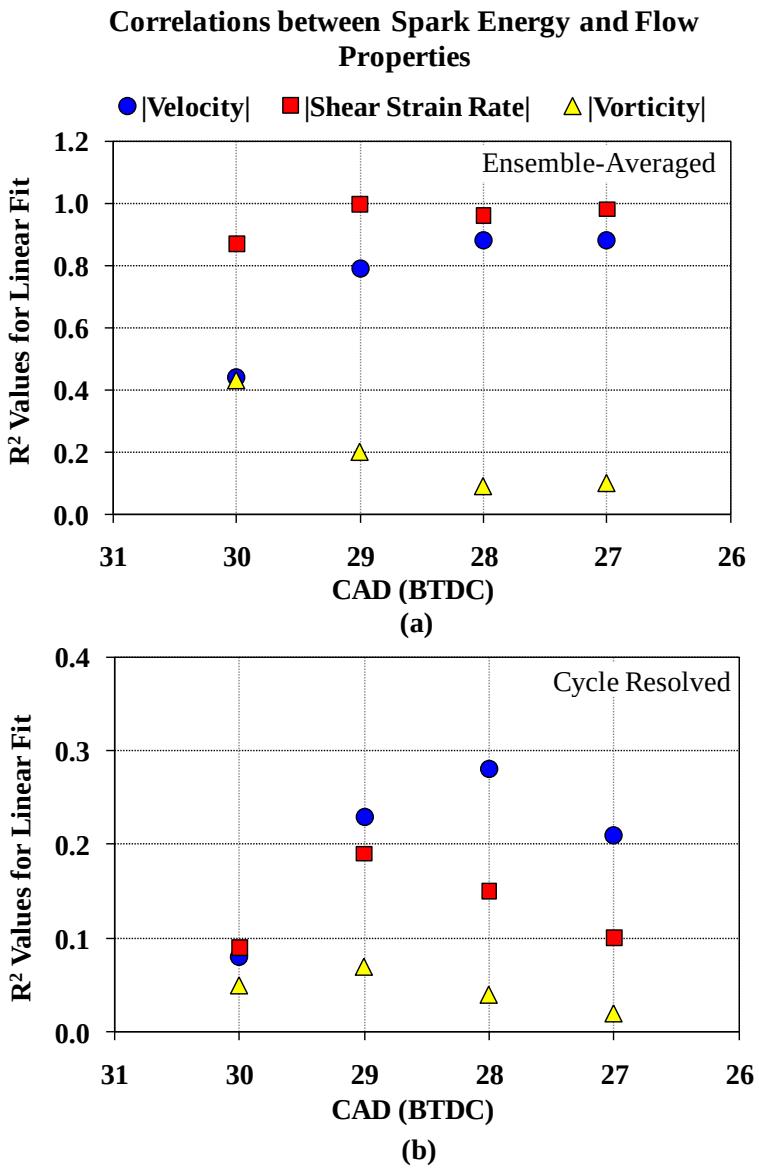

Figure C-4: R^2 values for correlations of crank-angle resolved measurements of spark energy and flow properties. Values are shown for quantities extracted from the first four crank-angles of the spark duration for air injection cycles presented in Chapter 3.

APPENDIX D

PARAMETER VALUES FOR CALCULATION OF MINIMUM IGNITION ENERGY

A theoretical expression for minimum ignition energy presented by Glassman [59] is used in Chapter 5 to provide an estimate of spark energy needed to reliably ignite a given mixture. This expression is given as:

$$\text{Minimum Ignition Energy} = \ 4/3\pi r_C^{\ 3} \ \ \rho c_P \ \ T_b - T_0 \qquad \text{(D-1)}$$

where r_C is the critical flame kernel radius, ρ is the unburned gas density, c_P is the specific heat at constant pressure, and T_b is the adiabatic flame temperature. The critical flame kernel radius is defined as:

$$r_C = 3k/\ \ \rho_b c_P S_L \qquad \text{(D-2)}$$

where k refers to the heat conductivity of the surrounding gas, ρ_b is the burned gas density, and S_L is the laminar flame speed for the given mixture. Table D-4 provides the parameter values used in these calculations for a range of lean-to-stoichiometric fuel-air mixtures. The properties of the fuel are calculated for a mixture of 90% isooctane, 10% biacetyl mixture by volume.

Values of air and fuel properties are obtained from Sonntag et al. [67] and Green et al. [68]. The unburned gas density, ρ, is calculated using the ideal gas law with the appropriate gas constant for the given fuel-air mixture. Temperature and pressure for the unburned mixture is 725 K and 1000 kPa respectively. The burned gas temperature (T_b) and laminar burning velocity (S_L) are obtained for isooctane-air mixtures from Martz et al. [69] and Metghalchi and Keck [64]. The heat conductivity of air is used at the unburnt gas temperature and pressure to calculate the flame kernel radius. The value of the heat conductivity of air at these conditions is k = 0.055 W/mK [68].

Equivalence Ratio	ρ [kg/m^3]	ρ_b [kg/m^3]	C_P [kJ/kgK]	T_b [K]	S_L (m/s)
0.5	5.41	2.01	1.15	1750	0.28
0.6	5.44	1.85	1.16	1890	0.45
0.7	5.46	1.70	1.18	2030	0.63
0.8	5.49	1.60	1.19	2170	0.80
0.9	5.52	1.55	1.20	2290	0.95
1.0	5.54	1.49	1.22	2400	1.03

Table D-4: Values of thermophysical properties.

APPENDIX E

CORRELATIONS OF SPARK ENERGY AND MEASUREMENTS OF FLOW FIELD AND FUEL CONCENTRATION FOR STRATIFIED FUEL OPERATION

The spark energy for the first spark crank-angle degree is correlated with spatially averaged quantities of equivalence ratio, velocity magnitude, shear strain rate magnitude, and vorticity magnitude measured in the 4 mm x 4 mm region at the onset of spark. This data is analyzed for operating conditions which incurred misfire and partial burn cycles; namely a spark timing of 30^{o} BTDC with dilution levels of 0%, 10% and 18% and a spark timing of 31^{o} BTDC with dilution levels of 18% and 26%. This analysis was conducted to compare the results for late injection, stratified operation to the findings for the well-defined conditions presented in Chapter 3. In addition, misfire and partial burn cycles are highlighted among the predominately well-burning cycles in an attempt to identify the cause of the errant cycles.

The breakdown event is not resolved in the spark measurements and is therefore the spark energy presented in this section begins at the onset of the arc phase once the voltage stabilizes after the initial voltage peak.

Figure E-5 shows the spark energy for the first spark CAD and spatially averaged equivalence ratio measurements at the different spark timings and dilution levels. Overall, the data exhibits large cycle-to-cycle variation in the measurements and thus

correlations are weak. For the spark timing of 30^{o} BTDC with 0% dilution (Figure E-5 (a)), the equivalence ratio measurements are scattered around stoichiometric and are within the flammability limits, while spark energy values are scattered between values of 1.5 mJ – 5.5 mJ. As dilution level increases with the spark timing of 30^{o}, mixtures become slightly richer and spark energies are within the range of 2 mJ and 5.5 mJ. The positive linear relationship between equivalence ratio and spark energy as shown in Chapter 3 is not evident for the measurements shown at the spark timing of 30^{o} BTDC. However, at the spark timing of 31^{o} BTDC, the positive relationship is more evident despite large scatter in the measurements. Equivalence ratio measurements at the spark timing of 31^{o} span a larger range ($1.0 \leq \overline{\Phi} \leq 4.5$) than at the spark timing of 30^{o} BTDC ($0.5 \leq \overline{\Phi} \leq 2.0$). At the spark timing of 31^{o} BTDC and 18% dilution level, equivalence ratio values are shown to be in the range of $1.0 \leq \overline{\Phi} \leq 3.0$ and spark energies fall within the range of 2 mJ – 10 mJ. As dilution level increases to 26% both equivalence ratio and spark energy show a slight increase. The positive relationship shown at the spark timing of 31^{o} is likely due to the larger range of rich mixtures near the spark plug at the time of spark. This range more appropriately spans the range of values studied in Chapter 3.

To provide additional insight to identify the cause of the errant cycles, misfire and partial burn cycles are highlighted among the predominately well-burning cycles in Figure E-5. Overall, the misfire and partial burn cycles occur within the same general population of well-burning cycles. For the spark timing of 30^{o} and 0% dilution level (Figure E-5 (a)), misfire and partial burn cycles occur for spark energies lower than 3 mJ with lean-to-stoichiometric equivalence ratios. As dilution level increases (Figure E-5 (b) and (c)), the available spark energy for the errant cycles increases slightly, but is

predominately below 4 mJ. At a spark timing of 31^{o} and dilution level of 18% (Figure E-5 (d)), the majority of the misfire and partial burn cycle occur for the lower spark energies for a given equivalence ratio. As dilution level increases to 26% (Figure E-5 (e)), errant cycles occur spark energies less than 8 mJ and a wide range of rich equivalence ratios. This information, while relevant, is insufficient to identify the cause of the misfire or partial burn cycles.

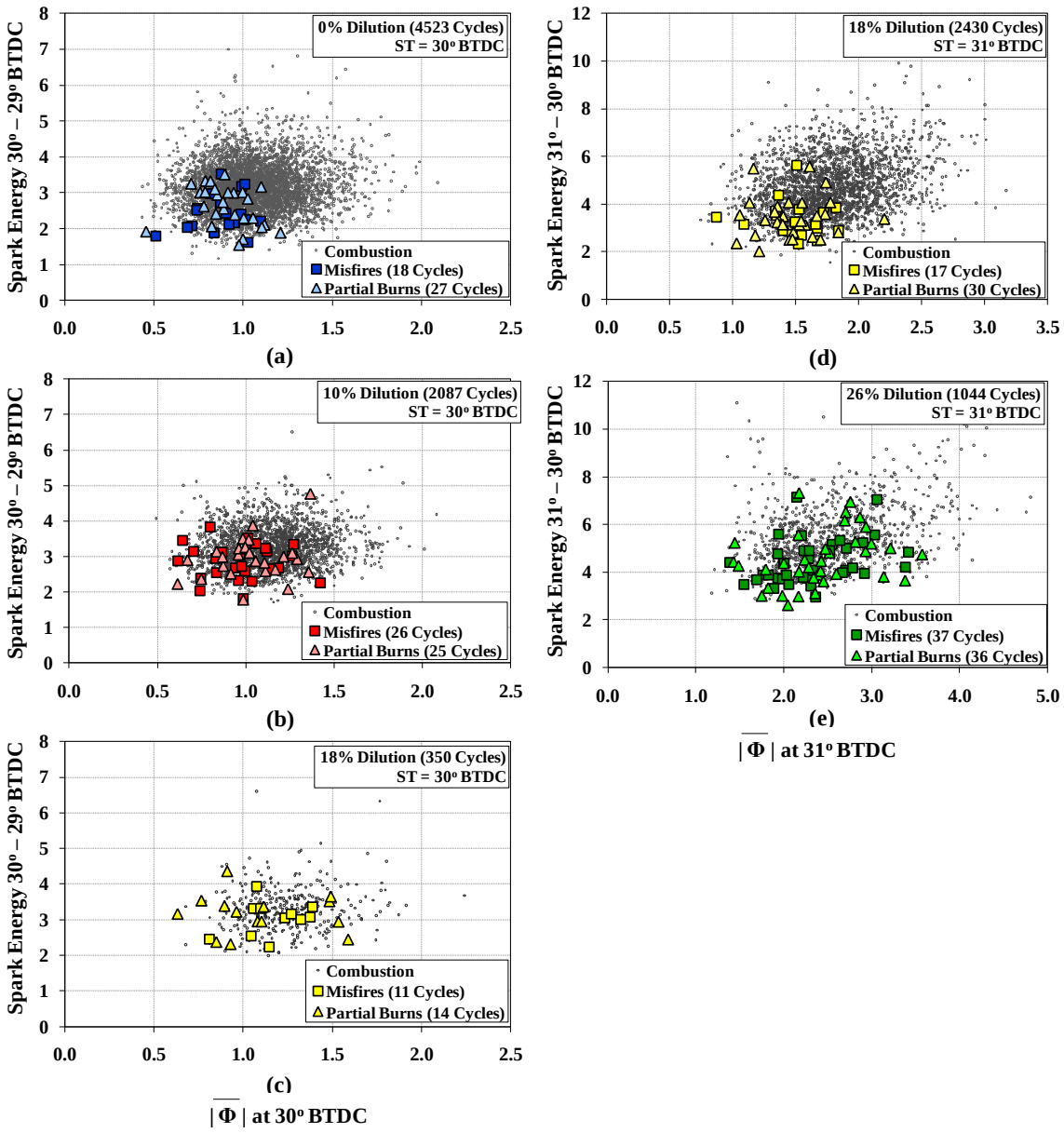

Figure E-5: Large cycle-to-cycle variation exists for the measurements of spark energy during the first spark CAD and the spatially averaged equivalence ratio within the 4 mm x 4mm region at the onset of spark. This data is only weakly correlated at best. A stronger positive relationship between spark energy and equivalence ratio is shown to exist at the spark timing of 31° BTDC than at 30° BTDC and is likely due to the larger range of equivalence ratios encountered at the spark timing of 31° BTDC. Furthermore, misfire and partial burn cycles are within the general population of well-burning cycles.

Figure E-6 shows the spark energy during the first spark CAD and velocity magnitude at the onset of spark for the different spark timings and dilution levels. Again, large cycle-to-cycle variation exists between the spark energies and velocity values and

thus only weak correlations are shown at best. A weak positive relationship between spark energy and velocity is shown at the spark timing of 30^o and dilution level of 0% (Figure E-6 (a)) and at the spark timing of 31^o BTDC with dilution level of 26% (Figure E-6 (e)). For all other operating conditions, the spread in the data is large and a positive relationship between the variables is not evident. This is not of great surprise since weak trends were also shown for the cycle-resolved velocity data presented in Chapter 3. The weak correlations are a likely result of the inability to directly measure the velocity along the plasma channel; at the onset of spark the plasma channel is located between the spark electrodes as opposed to within the 4 mm x 4 mm region. Measurements beyond the time of spark were unfortunately not available due to the fact that a flame kernel often existed in the 4 mm x 4 mm region which interferes with quantitative PLIF and PIV measurements.

At a spark timing of 30^o BTDC and dilution level of 0% (Figure E-6 (a)), misfire and partial burn cycles occur for lower velocity lower spark energies ($2 \text{ m/s} \leq \overline{V} \leq 8 \text{ m/s}$; $1\text{mJ} \leq E_{spark} \leq 3 \text{ mJ}$) and are less restricted to these conditions as dilution level increases to 10% and 18% (Figure E-6 (b) and (c)). At a spark timing of 31^o BTDC and dilution level of 18% (Figure E-6 (d)), the misfire and partial burn cycles are again more common for the lower velocities and lower spark energies within the distribution of well-burning cycles. As dilution level increases to 26% (Figure E-6 (e)), misfire and partial burn cycles are no longer restricted to the lower velocity, lower spark energy cycles. Overall, the errant cycles occur within the same general population of well burning cycles and are insufficient to identify the cause of the errant cycles.

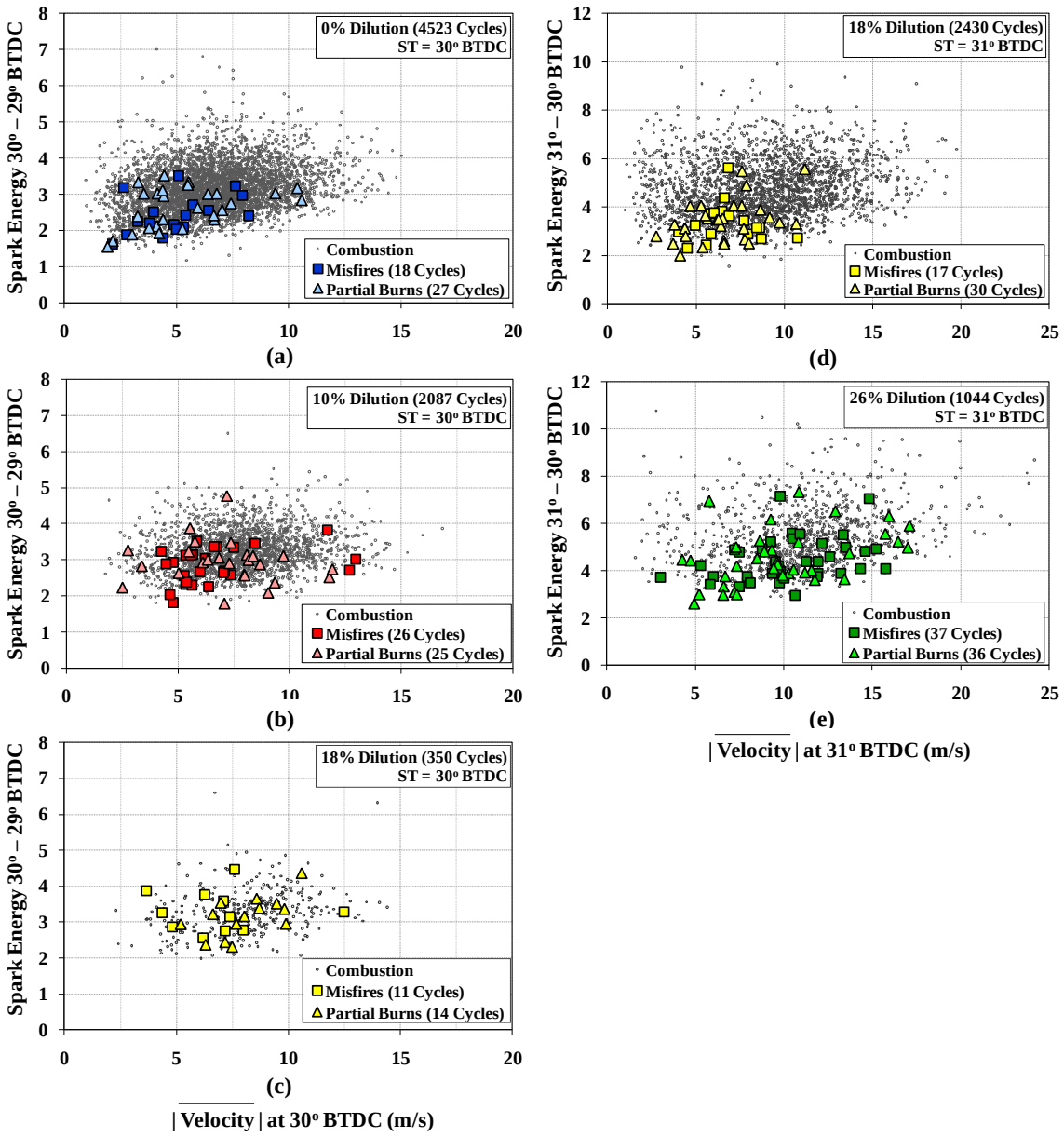

Figure E-6: Large cycle-to-cycle variation exists between spark energy during the first spark CAD and spatial averages of velocity magnitude and correlations at best are weak. Misfire and partial burn cycles are shown to be within the distribution of well burning cycles.

The initial spark energies are correlated with spatial averaged quantities of shear strain rate magnitude and are shown in Figure E-7. Again, large cycle-to-cycle variation exists in the measurements and thus significant correlations are not evident. Shear strain rate and spark energy are shown to increase as spark timing is advanced from 30° BTDC

to 31^{o} BTDC, but a positive relationship between spark energy and shear strain rate shown in Chapter 3 is not clearly evident in at either spark timing. Misfire and partial burn cycles are shown to be within the general population of well-burning cycles at each spark timing and dilution level. This data however does not provide additional insight to identify the cause of the errant cycles.

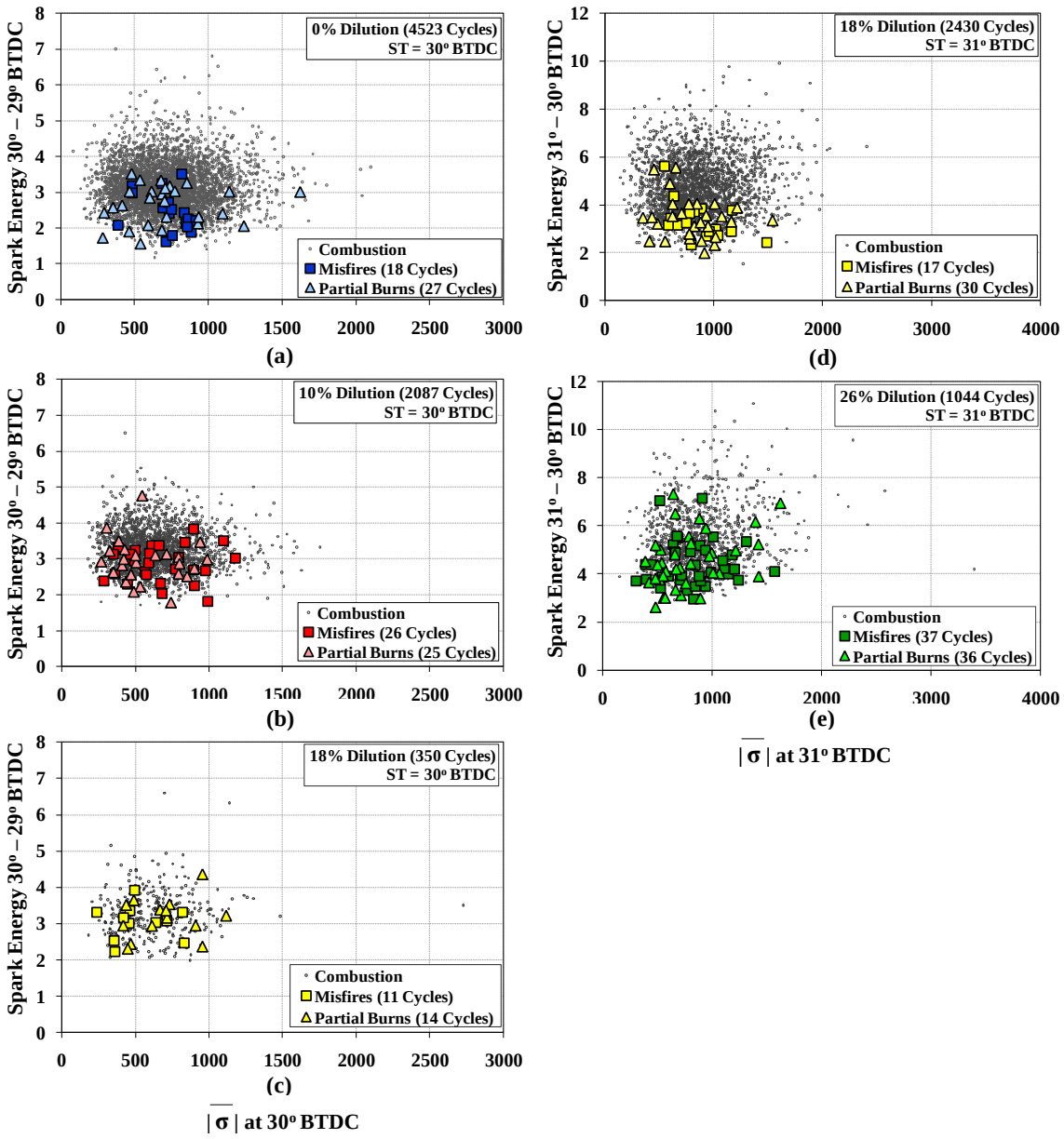

Figure E-7: Large cycle-to-cycle variation exists between measurements of the spark energy during the first spark CAD and spatially averaged values of shear strain rate magnitude and thus a correlation between these two variables is not evident. Misfire and partial burn cycles are within the general population of well-burning cycles.

Spark energy during the first spark CAD is also correlated with spatially averaged measurements of vorticity magnitude and is shown in Figure E-8. Again, the spread in the data is large and significant correlation does not exist for these measurements. Vorticity values are shown to increase as spark timing is advanced from 30° BTDC to 31° BTDC.

This is due to the stronger flow fields present near the spark plug due the shorter time delay between the end-of-injection (32^{o} BTDC) and the CAD of question. Misfire and partial burn cycles are shown to be within the distribution of well-burning cycles and thus do not provide additional information that identifies the cause of the errant cycles.

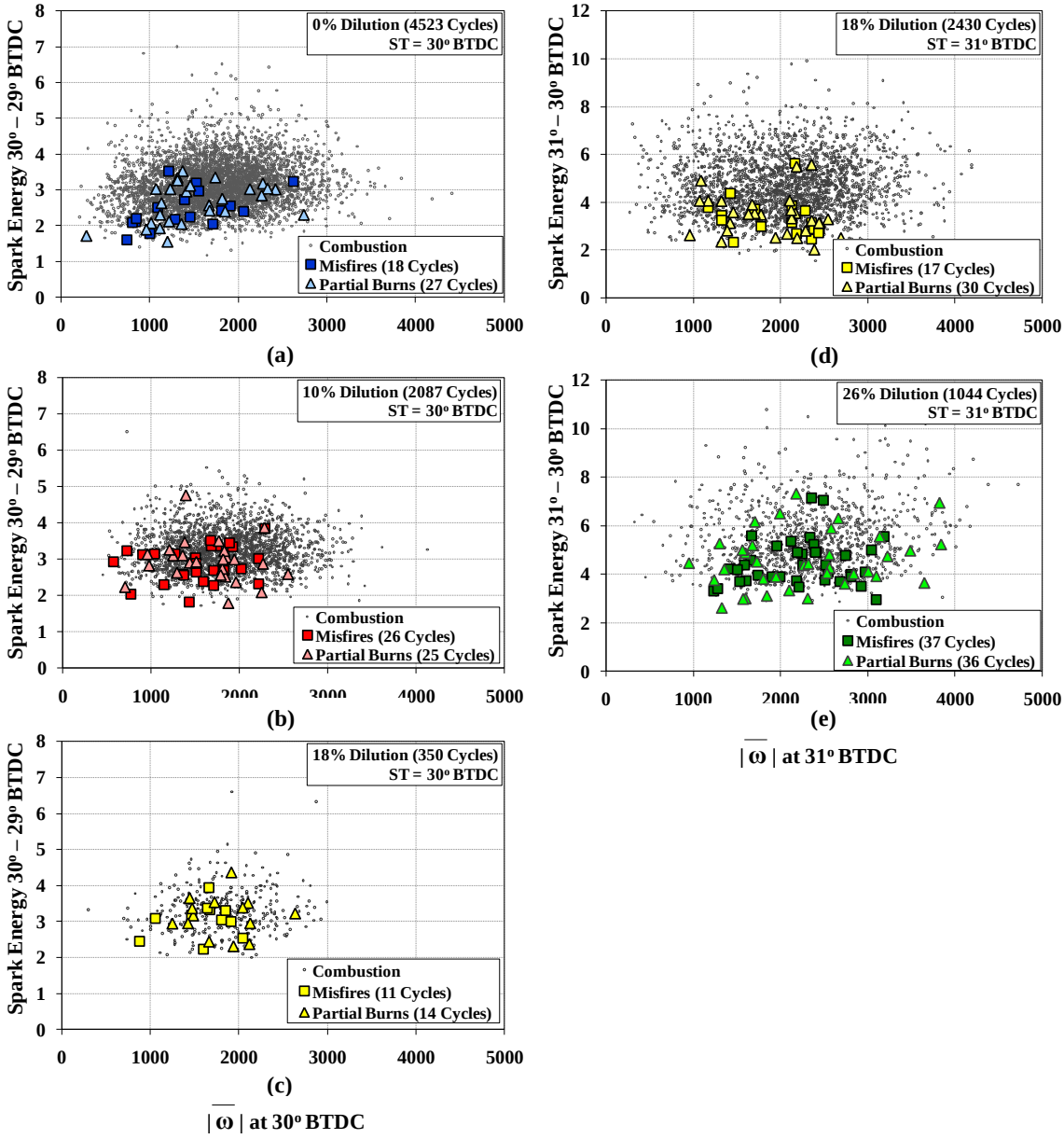

Figure E-8: Measurements of spark energy during the first spark CAD and spatially averaged values of vorticity magnitude show a large spread in the data and a significant correlation is not found for these measurements. Misfire and partial burn cycles are within the general population of well-burning cycles.

A comparison should be made about the comparison of flow field quantities between the air injection experiments presented in Chapter 3 and the stratified fuel injection experiments at a spark timing of 30^{o} BTDC and 0% dilution. The range of values for velocity, shear strain rate, and vorticity in the air injection experiments are similar to values revealed under stratified operation. However, despite similar or even higher injection pressures for air injection, the velocity range under stratified operation with fuel injection (2 – 15 m/s) is larger than what was seen under air injection (3 – 9 m/s). This is expected, given that the jet penetration is a function of the density ratio between injected fluid and the in-cylinder air. This ratio is lower for the air injection thus the penetration towards the spark plug is reduced and lower velocities are expected behind the spark plug. The inclusion of non-injection cycles in Chapter 3 provides spark energy characterization in the lower velocity regime (1-2 m/s).

Large cycle-to-cycle variation in the measurements between spark energy and spatially averaged quantities of equivalence ratio, velocity magnitude, shear strain rate magnitude, and vorticity magnitude prevent a significant correlation that exists for each operating condition. Weak correlations at best are found for some operating conditions. The weak or lack of correlations are presumably due to the inability to measure the in-cylinder conditions along the plasma channel. At the time of spark, the plasma channel is located between the spark electrodes as opposed to within the 4 mm x 4 mm region. After the onset of spark, the flow field has time to convect the plasma channel into the 4 mm x 4 mm region. However, measurements beyond the onset of spark are not available because a flame kernel often exists in the 4 mm x 4 mm region at this time which interferes with quantitative PLIF-PIV measurements.

In addition, the analysis of misfire and partial burn cycles presented in this section does not provide additional information that identifies the cause of the errant cycles.

BIBLIOGRAPHY

1. Heywood, J. B. *Internal Combustion Engine Fundamentals.* New York, Mc-Graw Hill Inc., 1988.

2. Zhao, F., M.-C. Lai, and D. L. Harrington. "Automotive Spark-Ignited Direct-Injection Gasoline Engines." *Progress in Energy and Combustion Science* **25**, 437-532 (1999).

3. Drake, M. C., T. D. Fansler, and A. M. Lippert. "Stratified-Charge Combustion: Modeling and Imaging of a Spray-Guided Direct-Injection Spark-Ignition Engine." *Proceedings of the Combustion Institute* **30**, 2683-2691 (2005).

4. Maly, R., in *Fuel Economy in Road Vehicles Powered by Spark Ignition Engines*, ed. by J.C. Hillard, G.S Springer. New York, Plenum Press, 1985.

5. Kim, J., and R. W. Anderson. "Spark Anemometry of Bulk Gas Velocity at the Plug Gap of a Firing Engine." *SAE* 952459 (1995)

6. Maly, R., and M. Vogel. "Initiation and Propagation of Flame Fronts in Lean CH_4-Air Mixtures by the Three Modes of the Ignition Spark." *17th Symposium (International) on Combustion*, Issue **1**, 821-831(1979).

7. Ballal, D. R., and A. H. Lefebvre. "The Influence of Spark Discharge Characteristics on Minimum Ignition Energies in Flowing Gases." *Combustion and Flame* **24**, 99-108 (1975).

8. Ballal, D. R.., and A. H. Lefebvre. "The Influence of Flow Parameters on Minimum Ignition Energy and Quenching Distance." *15th Symposium (International) on Combustion*, Issue **1**, 1473-1481 (1975).

9. Merer, M. R. and J. S. Wallace. "Spark Spectroscopy for Spark Ignition Engine Diagnostics." *SAE* 950164 (1995).

10. Lee, M. J., M. Hall, O. A. Ezekoye, R. Matthews. "Voltage, and Energy Deposition Characteristics of Spark Ignition Systems." *SAE* 2005-01-0231 (2005).

11. Maly, R., H. Meinel, and E. Wagner. “Novel Method for Determining General Flow Parameters from Conventional Spark Discharges.” *IMechE* Conference Transactions, **C67/83**, 27-32 (1983).

12. Ziegler, G. F. W., E. P. Wagner, and R. R Maly. “Ignition of Lean Methane-Air Mixtures by High Pressure Glow and Arc Discharges.” *20th Symposium (International) on Combustion*, Issue **1**, 1817-1824 (1985).

13. Ko, Y., V. S. Arpaci, and R. W. Anderson. “Spark Ignition of Propane-Air Mixtures Near the Minimum Ignition Energy: Part I. An Experimental Study.” *Combustion and Flame* **83**, 75-87 (1991).

14. Fansler, T. D., B. Stojkovic, M. C. Drake, and M. E. Rosalik. “Local Fuel Concentration Measurements in Internal Combustion Engines Using Spark-Emission Spectroscopy.” *Applied Physics B: Lasers and Optics* **75**, 577-590 (2002).

15. Fansler, T. D., M. C. Drake, and B. Böhm. “High-Speed Mie-Scattering Diagnostics for Spray-Guided Gasoline Engine Development.” *8th International Symposium on Internal Combustion Diagnostics*, Baden-Baden (2008).

16. Dulger, M., and E. Sher. “Experimental Study on Spark Ignition of Flowing Combustible Mixtures.” *SAE* 951004 (1995).

17. Riven, B., M. Dulger, and E. Sher. “Extending Lean Misfire Limit of Methane-Air Mixtures by Means of an Enhanced Spark Discharge.” *SAE* 199-01-0573 (1999).

18. Geiger, J., S. Pischinger, R. Böwing, H.-J. Koß, and J. Thiemann. “Ignition Systems for Highly Diluted Mixtures in SI-Engines.” *SAE* 1999-01-0799 (1999).

19. Ozdor, N., M. Dulger, E. Sher. “An Experimental Study of Cyclic Variability in Spark Ignition Engines.” *SAE* 960611 (1996).

20. Nakai, M., Y. Nakagawa, M. Sone. “Stabilized Combustion in a Spark Ignited Engine Through a Long Spark Duration.” *SAE* 850075 (1985).

21. Fansler, T. D., M. C. Drake, I. Düwel, F. P. Zimmermann. “Fuel-Spray and Spark-Plug Interactions in a Spray-Guided Direct-Injection Gasoline Engine.” 7th *International Symposium on Internal Combustion Diagnostics*, Baden-Baden (2006).

22. Maly, R. “Ignition Model for Spark Discharges and the Early Phase of Flame Front Growth.” *18th Symposium (International) on Combustion*, Issue **1**, 1747-1754 (1981).

23. Maly, R., and H. Meinel. “Determination of Flow Velocity, Turbulence Intensity and Length and Time Scales from Gas Discharge Parameters.” *Proceedings of the 5th International Symposium on Plasma Chemistry*, ISPC-5, 552-557 (1981).

24. Arcoumanis, C., and C-S. Bae. “Correlation Between Spark Ignition Characteristics and Flame Development in a Constant-Volume Combustion Chamber.” *SAE* 920413 (1992).

25. Danis, A. M., I. Namer, and N. P. Cernansky. “Droplet Size and Equivalence Ratio Effects on Spark Ignition of Monodisperse n-Heptane and Methanol Sprays.” *Combustion and Flame* **74**, 285-294 (1988).

26. Mastorakos, E. “Ignition of Turbulent Non-Premixed Flames.” *Progress in Energy and Combustion Science* **35**, 57-97 (2009).

27. Calcote, H. F., C. A., Gregory, C. M. Barnett, and R. B. Gilmer. “Spark Ignition: Effect of Molecular Structure.” *Industrial and Engineering Chemistry* **44**, 2656-2662 (1952).

28. Lewis, B., and G. von Elbe. *Combustion, Flames and Explosions of Gases*, 3rd Edition. New York, Academic Press, Inc., 1988.

29. Huang, C. C., S. S. Shy, C. C. Liu, and Y. Y. Yan. “A Transition on Minimum Ignition Energy for Lean Turbulent Methane Combustion in Flamelet and Distributed Regimes.” *Proceedings of the Combustion Institute* **31**, 1401-1409 (2007).

30. Hamai, D., H. Kawajiri, T. Ishizuka, and M. Nakai. “Combustion Fluctuation Mechanism Involving Cycle-to-Cycle Spark Ignition Variation Due to Gas Flow Motion in S.I. Engines.” *21st Symposium (International) on Combustion*, Issue **1**, 505-512 (1986).

31. Smith J. D., and V. Sick. “Factors Influencing Spark Behavior in a Spray-Guided Direct-Injection Engine.” *SAE* 2006-01-3376 (2006).

32. Warnatz, J., U. Mass, and R.W. Dibble. *Combustion*, 2nd Edition. Berlin, Springer, 1999.

33. Drake, M. C., D. T. French, and T. D. Fansler.” Advanced Diagnostics for Minimizing Hydrocarbon Emissions from a Direct-Injection Gasoline Engine.” *26th Symposium (International) on Combustion*, Issue **1**, 2581-2587 (1996).

34. Smith, J. D., and V. Sick. “Crank-Angle Resolved Imaging of Biacetyl Laser-Induced Fluorescence in an Optical Internal Combustion Engine.” *Applied Physics B: Lasers and Optics* **81**, 579-584 (2005).

35. Smith, J. D., and V. Sick. “A Multi-Variable High-Speed Imaging Study of Ignition Instabilities in a Spray-Guided Direct-Injected Spark-Ignition Engine.” *SAE* 2006-01-1264 (2006).

36. Fajardo C., and V. Sick. “Flow Field Assessment in a Fired Spray-Guided Spark-Ignition Direct-Injection Engine Based on Particle Image Velocimetry with Sub Crank Angle Resolution.” *Proceedings of the Combustion Institute* **31**, 3023-3031 (2007).

37. Fissenewert, U., V. Sick, and H. Pucher. “Characterization of Combustion and NO Formation in a Spray-Guided, Gasoline, Direct-Injection Engine Using Chemiluminescence Imaging, NO-PLIF, and Fast NO Exhaust Gas Analysis.” *SAE* 2005-01-2089 (2005).

38. Smith, J. D. “Development and Application of High Speed Optical Diagnostic Techniques for Conducting Scalar Measurements in Internal Combustion Engines.” *Ph.D. Dissertation*, University of Michigan (2006).

39. Fajardo, C. M., V. Sick, and D. L. Reuss. “Engine In-Cylinder-Turbulence Assessment Using Sub-Millimeter Resolution PIV.” In *PIV 2007,* Rome, Italy (2007).

40. Melling, A. “Tracer Particles and Seeding for Particle Image Velocimetry.” *Measurements Science and Technology* **8**, 1406-1416 (1997).

41. Fajardo, C. “Development of a High-Speed UV Particle Image Velocimetry Technique and Application for Measurements in Internal Combustion Engines.” *Ph.D. Dissertation*, University of Michigan (2007).

42. Keane, R. D., and R. J. Adrian. “Optimization of Particle Image Velocimeters. Part I: Double Pulsed Systems.” *Measurement Science and Technology* **1**, 1202-1215 (1990).

43. Megerle, M., V. Sick, and D. L. Reuss. “Measurement of Digital Particle Image Velocimetry Precision Using Electro-Optically Created Particle-Image.” *Measurement Science and Technology* **13**, 997-1005 (2002).

44. Westerweel, J. “Fundamentals of Digital Particle Image Velocimetry.” *Measurement Science and Technology* **8**, 1379-1392 (1997).

45. Reuss, D. L., M. Megerle, and V. Sick. “Particle-Image Velocimetry Measurement Errors When Imaging Through a Transparent Engine Cylinder.” *Measurement Science and Technology* **13**, 1029-1035 (2002).

46. Funk, C. O. “An In-Depth Comparison of Experimental and Computational Turbulent Parameters For In-Cylinder Engine Flows.” *Ph.D. Dissertation*, University of Michigan (2005).

47. Westerweel, J. “Efficient Detection of Spurious Vectors in Particle Image Velocimetry Data.” *Experiments in Fluids* **16**, 236-247 (1994).

48. Westerweel, J., D. Dabiri, and M. Gharib. “The Effect of a Discrete Window Offset on the Accuracy of Cross-Correlation Analysis of Digital PIV Recordings.” *Experiments in Fluids* **23**, 20-28 (1997).

49. Einecke, S., C. Schulz, and V. Sick. “Measurement of Temperature, Fuel Concentration and Equivalence Ratio Fields Using Tracer LIF in IC Engine Combustion.” *Applied Physics B: Lasers and Optics:* **71**, 717-723 (2000).

50. Smith, J. D., and V. Sick. “Quantitative, Dynamic Fuel Distribution Measurements in Combustion-Related Devices Using Laser-Induced Fluorescence Imaging of Biacetyl in Iso-octane.” *Proceedings of Combustion Institute* **31**, 747-755 (2007).

51. Beyrau, F., A. Brauer, T. Seeger, and A. Leipertz. “Gas-Phase Temperature Measurement In The Vaporizing Spray of a Gasoline Direct-Injection Injector by Use of Pure Rotational Coherent Anti-Stokes Raman Scattering.” *Optics and Letters* **29** (3), 247-249 (2004).

52. Rassweiler, G. M., and L. Withrow. “Motion Pictures of Engine Flames Correlated With Pressure Cards.” *SAE Transactions* **38** (1938).

53. Cundy, M., T. Schucht, O. Thiele, and V. Sick. “High-Speed Laser-Induced Fluorescence and Spark Plug Absorption Sensor Diagnostics For Mixing and Combustion Studies in Engines.” *Applied Optics,* **48**, B94-B104 (2009).

54. Adrian, R. J. “Dynamic Ranges of Velocity and Spatial Resolution of Particle Image Velocimetry.” *Measurement Science and Technology* **8**, 1393-1398 (1997).

55. Peterson, B., and V. Sick. “Simultaneous Flow Field and Fuel Concentration Imaging at 4.8 kHz in an Operating Engine.” *Applied Physics B: Lasers and Optics* **97** (4), 887-895 (2009).

56. Quader, A. “Why Intake Charge Dilution Decreases Nitric Oxide Emission from Spark Ignition Engines.” *SAE* 710009 (1971).

57. Blanc, M. V., P. G. Guest, G. von Elbe, and B. Lewis. “Ignition of Explosive Gas Mixtures by Electric Sparks: III. Minimum Ignition Energies and Quenching Distances of Mixtures of Hydrocarbons and Ether with Oxygen and Inert Gases.” *Third Symposium on Combustion and Flame and Explosion Phenomena*, Issue **1**, 363-367 (1949).

58. Strehlow, R. A. *Fundamentals of Combustion.* New York, Robert E. Kreiger Publishing Company, 1979.

59. Glassman, I., and R. A. Yetter. *Combustion*, 4th Edition. New York, Elsevier, 2008.

60. Swett, C. C., and R. H. Donlon. “Spark Ignition of Flowing Gases III – Effect of Turbulence Promoter on Energy Required to Ignite a Propane-Air Mixture.” *NACA Research Memorandum*, RM E52 – J28 (1953).

61. Bradely, D., and F. K-K. Lung. “Spark Ignition and the Early Stages of Turbulent Flame Propagation.” *Combustion and Flame* **69**, 71-93 (1987).

62. Steinberg, A. M., J. F. Driscoll, and S. L. Ceccio. “Temporal Evolution of Flame Stretch Due to Turbulence and the Hydrodynamic Instability.” *Proceedings of the Combustion Institute* **32**, 1713-1721 (2009).

63. Böhm, B, D. Geyer, A. Dreizler, K. K Venkatesan, N. M Laurendeau, and M. W. Renfro. “ Simultaneous PIV/PTV/OH PLIF Imaging: Conditional Flow Field Statistics in Partially Premixed Turbulent Opposed Jet Flames.” *Proceedings of the Combustion Institute* **31**, Issue 1, 709-717 (2007).

64. Metghalchi, M. and J. C. Keck. “Burning Velocities of Mixtures of Air with Methanol, Isooctane, and Indolene at High Pressure and Temperature.” *Combustion and Flame* **48**, 191-210 (1982).

65. Alkidas, A. C., A. M Lippert, D. L. Reuss, J. Liedtke, and K.-J. Wu. “Fuel Economy and Engine-Out Emissions from a Single-Cylinder Two-Valve Direct-Injection S.I. Engine Operating in the Stratified-Combustion Regime.” *SAE* 2002-01-2658 (2002).

66. Koban, W., J. D. Koch, V. Sick, N. Wermuth, R. K. Hanson, and C. Shulz. “Predicting LIF Signal Strength for Toluene and 3-Pentanone Under Engine-Related Temperature and Pressure Conditions.” *Proceedings of the Combustion Institute* **30**, 1545-1553 (2005).

67. Sonntag, R. E., C. Borgnakke, and G. J. Van Wylen. *Fundamentals of Thermodynamics*, Sixth Edition. New Jersey, John Wiley & Sons, 2003.

68. Green, D. W., and R. H. Perry. *Perry’s Chemical Engineers’ Handbook*, 8th Edition. New York, McGraw-Hill Inc., 2008.

69. Martz, J. B., R. J. Middleton, G. A. Lavoie, A. Babajimopoulous, and D. N. Assanis. “A Computational Study and Correlation of Premixed Isooctane-Air Laminar Flame Properties under Spark Ignited and Spark Assisted Compression Ignition Engine Conditions.” *Combustion and Flame* – Accepted (2010).